Politecnico di Milano
Department of Physics
Laurea Magistrale in Engineering Physics

Crystal field driven metamagnetic transitions in $HoIr_2Si_2$ analyzed by means of X-ray spectroscopy and full atomic multiplet calculations

Master's thesis of:
Riccardo Marco Augusto Bona
Matr: 876727

Supervisor:
Prof. Giacomo Ghiringhelli

Tutor:
Dr. Kurt Kummer

2017 – 2018

POLITECNICO DI MILANO

Abstract

Engineering Physics
Department of Physics

Crystal field driven metamagnetic transitions in $HoIr_2Si_2$ analyzed by means of X-ray spectroscopy and full atomic multiplet calculations

by Riccardo Marco Augusto BONA

Lanthanide materials exhibit exotic properties due to the concurrence of atomically localized and collective electronic interactions. A complete theory adequate to properly account for all the experimentally determined features has not been conceived yet. Still, in the framework set by full multiplet atomic theory, starting from a local Ansatz, most of the characteristics regarding rare earth compounds are properly described. The coexistence of anisotropies, set by crystalline environment, and electronic coupling effects between rare earth atoms leads to unconventional magnetic phase diagrams. X-ray absorption and Resonant Inelastic X-ray Scattering data have been collected for $HoIr_2Si_2$ sample, with high quality synchrotron light, at beamline ID32 of the European Synchrotron Radiation Facility (ESRF). A combined analysis of X-ray spectra and magnetic properties reported in literature yielded a complete set of parameters which binds the shape of the ground state 4f wave function of Ho^{3+} ion in $HoIr_2Si_2$. Metamagnetic transitions occurring in $HoIr_2Si_2$ can be well described combining crystal electric field model with exchange coupling interactions. The methodologies exploited in this thesis work can be fruitfully applied to the analysis of similar compounds, characterized by intriguing magnetic phase diagrams.

POLITECNICO DI MILANO

Sommario

Engineering Physics
Department of Physics

Crystal field driven metamagnetic transitions in $HoIr_2Si_2$ analyzed by means of X-ray spectroscopy and full atomic multiplet calculations

by Riccardo Marco Augusto BONA

I composti di terre rare sono caratterizzati da diagrammi di fase che sfuggono ai modelli convenzionali della fisica dello stato solido. A causa della simultanea presenza di effetti legati al carattere fortemente localizzato degli orbitali di valenza 4f e della loro ibridizzazione con la banda di conduzione, non è ancora stata formulata una teoria esaustiva per questa classe di materiali. Non di meno, molte delle proprietà dei lantanoidi sono inquadrabili nell'ambito della teoria dei multipletti atomici, nella quale lo schema energetico dei livelli elettronici per lo ione di terra rara è primariamente determinato da interazioni elettrone-elettrone. Secondo questa teoria, la presenza degli atomi circostanti può essere utilmente modellata sostituendo la matrice cristallina con un campo elettrico efficace, nell'applicazione del modello a campo elettrico cristallino. La competizione tra interazioni di campo cristallino e termini elettronici di scambio, tra atomi di terre rare, in diversi siti cristallini, si esprime in diagrammi di fase magnetici non ordinari. Dati di spettroscopia ad assorbimento e a diffusione inelastica risonante di raggi X per il campione $HoIr_2Si_2$ sono stati raccolti presso l'installazione Europea di sincrotrone ESRF. Combinando l'analisi di spettri e delle proprietà magnetiche è stato possibile determinare la funzione d'onda dello stato fondamentale per lo ione Ho^{3+} in $HoIr_2Si_2$. Inoltre, le transizioni di fase metamagnetiche in $HoIr_2Si_2$ sono state adeguatamente riprodotte con simulazioni basate sulla teoria a multipletto atomico, includendo un campo cristallino efficace e un accoppiamento antiferromagnetico per una coppia di ioni Ho^{3+}. Le metodologie applicate in questo lavoro di tesi potrebbero essere proficuamente estese all'analisi di campioni simili caratterizzati da diagrammi di fase magnetici inusuali.

Acknowledgements

Many thanks to ID32 group of ESRF for hosting me, in particular to my tutor Dr. Kurt Kummer for his patience in answering my questions, even when they did not make any sense.

Thanks also to the scientists of ID20 for the pleasant lunch breaks spent together.

Thanks to my supervisor Prof. Giacomo Ghiringhelli, for giving me the opportunity of writing my thesis in a high stimulating work environment as ESRF.

La gratitudine non sarà mai sufficiente per i miei genitori, che mi hanno supportato in tutto il mio percorso: a mio padre a cui penso ogni giorno e a mia madre che ha sempre creduto fin troppo in me.

Una menzione al mio compagno di appartamento e di avventura Marco con il quale ho condiviso questa importante esperienza di vita.

Infine, i miei ringraziamenti devono andare ai miei amici, quelli di lunga data e quelli che lo diventeranno, e alla mia ragazza per aver scelto di vivere con me questa porzione così importante di vita.

Contents

List of Figures

List of Tables

A chi non c'è più, a chi c'è sempre stato e a chi vorrà esserci.

Introduction

The following thesis deals with the project carried on from september 2018 to march 2019 with the group of scientists at beamline ID32 of the European Syncrothron Radiation Facility (ESRF).

In this work, experimental Resonant Inelastic X-ray Scattering (RIXS) and X-ray Absorption Spectra (XAS) are compared to calculations performed in the framework of the full multiplet atomic theory.

Indeed, 4f valence ions are eligible candidates for the application of a local approach, due to their lack of participation in chemical bonds [1, 2]. At the same time, though, a plethora of collective striking effects arise when 4f-partially filled atoms arrange in a crystalline structure, ranging from magnetically ordered to unconventional superconductive states. Hence, rare earth compounds are labeled as strongly correlated materials, meaning that 4f electrons can not be fully described as independent particles in a mean-field potential. This double character of 4f systems has led to a growing scientific interest lately [3].

On one side, an exhaustive theory able to account for all the exotic properties associated to 4f systems has not been reached so far. On the other side, the improvement of X-ray facilities has pushed the resolution limit beyond wildest dreams for any experimentalist, providing the scientific literature with loads of data. The thesis work hereafter aims at shedding some more light on the complex magnetic features in this class of materials.

In particular, in chapter 1 a theoretical background for the exploited spectroscopic techniques will be given. Going further, chapter 2 deals with description of the state-of-the-art ID32 beamline at ESRF. Then, in chapter 3 the reader will be provided with the proper framework required to describe most of the properties of rare earth ions in a crystalline environment. In the same chapter, a brief outline is proposed about the simulation tool used to analyze experimental data coming from RIXS and XAS measurements; a grasp will be presented of how calculations, based on a local Ansatz, can account for most of the properties of rare earth systems. Simulations are usefully exploited in chapters 4 and 5, where atomic parameters convenient in modeling the rare earth ion Hamiltonian will be inferred by comparison with experimental data.

Notably, chapter 4 is conceived with the aim to prove to the reader how the theory developed in chapter 3 can be conveniently exploited to model the energetic scheme of a 4f valence ion. To probe multiplet excitations occurring in 4f shell, RIXS is the elective tool due to the achievable resolution, matching typical energy of *ff* excitations [4, 5]. Moreover, analyzing RIXS experiments through simulations, one can unambiguously distinguish spin-orbit split features from high-excited electrostatic terms, thus inferring energy splittings between ground state and other configurations higher in energy. Finally, in chapter 5 the local model will be extended in order to account for collective effects

occurring in $HoIr_2Si_2$, which exhibits intriguing magnetic properties.
Before starting, it is here useful to clarify some definitions extensively used in the following chapters. To identify the spectral absorption edges analyzed in this work, the IUPAC spectroscopic notation will be exploited [6]. Depending on the principle quantum number n of the involved core level, a letter is associated to the electronic transition towards the valence shell, i.e. K, L, M, N, O edges are linked respectively to transitions from n = 1, 2, 3, 4, 5 core shell. Then, a subscript number is put, which labels different lines in the same shell, depending on their energy, i.e. subshells defined by different l and spin-orbit split states defined by different j. Higher subscript numbers are associated to less bound core states, i.e. less energetic edges in XAS spectra. Regarding this work, $M_{4,5}$ edges are investigated; M is linked to transitions from the shell $n = 3$ to the valence states, whereas the subscript numbers 4, 5 refer to the subshell d, with 4 linked to transitions from the core state $3d_{3/2}$ and 5 to $3d_{5/2}$.
Finally, to label the symmetries of rare earth ions in crystalline environment, the crystallographic point group symmetry notation named after Schönflies is used [7]. In particular, this thesis deals with the crystallographic space point group D_{4h}. D stands for dihedral or two-sided group; the number 4 accounts for the four-fold rotation axis, plus the four two-fold rotation axes perpendicular to it; h means that the reflection with respect an horizontal plane is listed among the symmetry operations for this group, along with reflections with respect to four vertical planes, each containing the four-fold and one of the two-fold axis.

Chapter 1

Experimental techniques

Light is a valuable tool in probing the properties of solids. In particular, radiation in the vacuum ultraviolet and X-ray range efficiently interacts with electrons in solids [8]. Lately, thanks to the technological advances, synchrotron radiation sources have reached brilliance comparable with that of lasers [8, 9]. These improvements have led to a growing interest in experimental techniques involving light spectroscopy, especially in X-ray region, performed with synchrotron facilities [9].

In the following sections, a brief description of the X-ray techniques used to collect the data for this work will be provided. In particular, the focus will be on Resonant Inelastic X-Ray Scattering (RIXS) and X-Ray Absorption Spectroscopy (XAS). A short background on X-Ray Magnetic Circular Dichroism (XMCD) will be presented, for it has been useful in the analysis of the magnetic arrangement of Ho momentum in $\mathrm{HoIr_2Si_2}$ compound.

1.1 X-Ray Absorption Spectroscopy (XAS)

XAS is a spectroscopy technique which allows to probe transitions from ground to core excited states [9, 10]. In the framework which will be discussed for RIXS, the absorption step can be seen as equivalent to an XAS experiment. Indeed, XAS spectra are usually acquired before any RIXS measurement, for they are useful in selecting the incident energy on a strong resonance so that RIXS cross section is enhanced.

In figure 1.1 the general scheme of a spectroscopic experiment is displayed.

The importance of performing X-ray spectroscopy experiments exploiting synchrotron radiation must be stressed; the possibility to tune the entrance energy to a high degree and over a continuum large spectrum without losing brilliance, along with the possibility to exploit polarization characteristics of the synchrotron light has given a boost to experiments performed with this technique, since the advent of first dedicated facilities [9].

The XAS cross section is proportional to

$$\sigma \propto |\langle n|T|g\rangle|^2 \times \delta(E_n - E_g + \hbar\omega_{in}), \tag{1.1}$$

whith $T = \boldsymbol{\epsilon}\mathbf{p}$ in dipole approximation, where $\boldsymbol{\epsilon}$ and $\mathbf{p}$ stand precisely for polarization and momentum of the incoming photon. In eq. 1.1, g and n are the

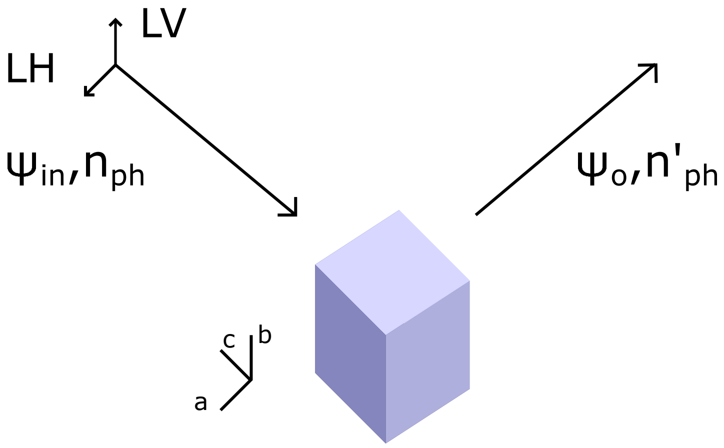

FIGURE 1.1: Spectroscopy experiment scheme. Incoming photons excite matter from its ground state ψ_{in} to an excited one ψ_o. Then, a detector collects a signal which is a hint of the excitations occurring in the sample. In XAS, the signal is proportional to the number of absorbed photons at each energy. In RIXS, the signal is the number of photons with a certain energy loss with respect to the incident energy. In the cartoon Linear Vertical (LV) and Linear Horizontal (LH) polarizations relative to the axes of a unitary crystal cell belonging to D_{4h} point group symmetry are shown.

initial and final state respectively. The δ is for energy conservation purpose, which along with linear and orbital momentum conservation laws is the key to the understanding of any spectroscopic result.

In practice, the incoming photon energy is scanned over an energy interval. When it matches a particular resonant edge, matter strongly interacts with light absorbing a large amount of photons. In other words, when photon frequency resonates with the energy difference between an excited state and the ground state an electron can be promoted, as a result of the absorption of the photon. Therefore, XAS spectra can be seen as the density of unoccupied states times the probability to reach them.

In order to relate XAS spectra with a commonly used empirical parameter in optics, the Lambert-Beer law for the attenuation of light in matter is here recalled

$$I_x = I_0 e^{-\mu(\omega_{in})x}, \tag{1.2}$$

where I_x and I_0 stand for intensity at the coordinate x and the incident one respectively. $\mu(\omega_{in})$ is the so-called absorption coefficient, which is a function of the incident photon energy; indeed, a normalized XAS spectrum is proportional to the ratio between the intensity exiting a sample and the incident one, scanned over an energy range, i.e. $I_{XAS} \propto e^{-\mu(\omega_{in})t}$, with t being the thickness of the sample. Thus, combining eqs. 1.1 and 1.2, one can link an empirical parameter like the absorption coefficient to a quantity which in principle comes from calculations.

All in all, the evaluation of spectra is a matter of calculating eigenstates of the initial Hamiltonian and reachable final states according to selection rules. In

order to have a non zero integral, the overall function in the braket $\langle n|\boldsymbol{\epsilon}\mathbf{p}|g\rangle$ must be even; selection rules come as consequence. In electric dipole approximation, the transition operator is an odd function, therefore initial and final wavefunctions must have different parity in order to have a non-zero matrix element. To put it in another way, one may think to express wavefunctions and operator as spherical harmonics, thus reducing to the overall conservation of momentum quantum numbers. Since photon is carrying an orbital momentum equal to one and zero spin, in dipole-like transitions, the following rules can be stated: $\Delta l = \pm 1$, $\Delta s = 0$ and $\Delta J = 0, \pm 1$ with the constrain that $J_i + J_f \geq 1$; for the magnetic quantum numbers, accordingly $\Delta m_l = 0, \pm 1$ and $\Delta m_s = 0$.
In principle, other multiplet orders can lead to transitions that are dipole forbidden, but their intensities will be orders of magnitude smaller with respect to dipolar ones.
The evaluation of final eigenstates is a non trivial problem when performing simulations of experimental spectra. In the insight about Quanty 3.3, the script language used the simulation of spectra, the issue of calculating final excited states, which is fundamental when dealing with spectroscopic simulations, RIXS as well, will be discussed.
As the reader can notice from eq. 1.1, the polarization of incident photon matters in the evaluation of transition intensity, thus opening the possibility of performing a dichroism analysis in spectra. The possibility of performing dichroism experiments seems to be promising for the evaluation of crystal field effects. Indeed, probing different crystalline directions is the key to see in spectra electronic or magnetic anisotropy effects [10–13].
Nevertheless, there are some major drawbacks with respect to RIXS, when dealing with crystal field split f states, that should be highlighted and that will be clear after discussion of resonant scattering in next section. As seen, XAS cross-section is dipole dominated so that *ff* transitions, which are not allowed due to selection dipolar rules, are only indirectly probed. Instead, RIXS does not have to face this limit, for *ff* transitions can be seen as the sum of two allowed dipole transitions and in principle resonant scattering can be sensitive to higher order symmetry mixing of states, such as the four-fold one occurring in a tetragonal crystal system [4]. To put it in other words, there is no chance to probe the in-plane spatial orientation, i.e. the planar orbital occupation of states, in compounds which displays a tetragonal symmetry relying only on XAS spectroscopy, limited to probe only up to two-fold ground state symmetries. Moreover, the resolution of an XAS spectrum at the $M_{4,5}$ edge typically can not be lower than 1 eV, being dominated by intrinsic core hole lifetime broadening. Therefore, any information related to *ff* excitations, whose energy scale can be in the order of ∼10 meV, can only be indirectly obtained.
In RIXS experiments instead, resolution of the order of 10 s meV and with peak values of 30 meV at the copper L_3 edge at ERIXS-ID32 is achievable [5], which allows to directly resolve 4f energy levels. Indeed, due to the fact that the final reached state is in a low excited energy configuration with respect to the initial one, a long life time is expected; as a result, the combined resolution has a technological limit and depends mainly on the quality of the beam, the monochromator and the spectrometer. As a matter of fact, one may partially

cope with the second limit, exploiting, when possible, the rather large polarization dependence, which can in the end push the analysis beyond the resolution limit constrain [10, 13]. Still, when resolution is appropriate, RIXS spectra are expected to offer less ambiguous results, for one, in principle, can rely on directly resolved splittings of multiplets rather than analyze how crystal field indirectly affects the transition probability [4].

After having introduced the general scheme in a spectroscopic experiment, it seems now relevant to account the temperature for as an important parameter in measurements. Temperature can be seen as a reservoir of energy for electrons which can populate states above the ground with a probability given by Boltzmann statistics

$$dZ = 1/e^{-\frac{E_i - E_{gs}}{k_B}}, \tag{1.3}$$

where E_i and E_{gs} stand for the excited and ground state energy respectively. It is clear that the shape of spectra is strongly dependent on temperature, for different states can be populated, changing then the initial states and the reachable ones. Moreover, temperature can be a rough measure of the splitting between ground and excited states and temperature analysis of spectra can be an interesting experiment to carry out [14, 15]. The spectra acquired to obtain the CEF scheme of the compounds for this work have been obtained at low temperature, i.e. around 20 K, in order to have most of the sample in the ground state.

In the next section a further insight about dichroism will be given, in particular about magnetic circular dichroism.

1.1.1 Dichroism

Dichroism is a property of certain compounds to give a different response depending on the relative orientation between polarization of light and symmetry axes of the sample [4, 10, 13, 16]. Therefore, the signal X-ray Circular Dichroism will be defined as the difference between the spectrum acquired with a right circular polarization and the one acquired with left circular one. Instead, one may refer to X-ray Linear Dichroism when light is linearly polarized: in the latter case the dichroism signal is the difference between two spectra acquired with different experimental geometries, including in the term geometry the relative orientation of the polarization and the wave vector with respect to the symmetry axes [10].

In order to have any spatial anisotropy, there must be a term in the Hamiltonian which breaks spherical symmetry of the free atom. For instance, a symmetry loss occurs when exchange field driven interactions are present or when an external magnetic or electric field is applied as well. Crystal field can be modeled as a fictitious electric field in the sample, which forces the atom to orient the spatial electronic wavefunctions along easy axes [1, 2, 17–20]. To put it in other words, the crystal field splits the 2J + 1 degenerate atomic energy levels of the free atom, according to their spatial orientation along the symmetry axes, i.e. depending on the value of the quantic number M.

It is now appropriate to introduce the 3J-symbols formalism and express transition probability in terms of the product of spherical harmonics, i.e. in terms of quantic numbers J and M, related to the overall momentum and its projection along a quantization axis [1, 17]. According to Wigner-Eckhart theorem [1], the transition probability in eq. 1.1 can be separated into a radial and an angular part

$$\langle n(JM)|\boldsymbol{\epsilon}\mathbf{r}|g(J'M')\rangle = (-1)^{J-M}\begin{pmatrix} J & 1 & J' \\ -M & q & M' \end{pmatrix}\langle n|\boldsymbol{\epsilon}\mathbf{r}|g\rangle, \tag{1.4}$$

where the momentum vector $\mathbf{p}$ has been replaced by the position vector $\mathbf{r}$ through the use of the commutator $[\frac{\mathbf{p}}{2m},\mathbf{r}] = \frac{-i\hbar\mathbf{p}}{m}$ and q stands for the projection of the momentum carried by the incoming plane wave, i.e. $q = 0, \pm 1$. In order to have a non-zero 3J symbol, the following conditions must be fulfilled: the absolute value of each element of the second row must be smaller or equal to the corresponding element in column and the subtraction by column of the two element must be equal to an integer; $-M + q + M' = 0$, which can be seen as another way to express the selection rule $\Delta M = 0, \pm 1$; $J' + 1 + J$ is an integer; $|J - 1| \leq J' \leq |J + 1|$, also known as the triangular relation and related to the selection rule $\Delta J = 0 \pm 1$. Accordingly, depending on the value of q, i.e. the polarization of light, transitions are likely to happen or not.

In order to better explain the source of magnetic circular dichroism in spectra one may refer to the so-called two-step model for XMCD [16]. The model is conceived for $L_{2,3}$ edges of transition metals; nevertheless, it can be useful to give a general explanation of why differences in absorption spectra must be expected, when dealing with magnetic materials. The model will be also helpful to finally give an argument for the development of the so-called sum rules [21].

In the first step, considering transitions starting from $p_{1/2}$, excited by a right circular polarization, i.e. $\Delta m = +1$, counting all the possible reachable final levels, there is a 75% probability of a spin up final state, while for the L_3 edge a 62.5% probability of a spin down final state. Therefore, the constrains due to dipole selection rules and to the value of the 3J symbols involved in transitions result in a spin polarized final state, depending on the considered edge. So far, no magnetic effect has been accounted for the dichroism in spectra. In step two of the model, magnetism is taken into consideration, by considering a final spin split band state, as it is in ferromagnetic materials for instance or when any external field breaks the spherical symmetry, e.g. due to Zeeman or crystal field effects. As a result of the two steps, the excitation probability of polarized electrons depends on the density of final states which are reachable according to selection rules, being the intensity of the absorption cross-section dependent on the availability of polarized final states, according to Pauli exclusion principle. All in all, the sum of the two effects will result in a difference in the absorption coefficients controlled by the polarization of incoming light. Taking into account an orbital polarization as well, eq. 1.1 can be rewritten as

$$\sigma_{\pm} \propto |\langle n|T|g\rangle|^2 \times (\rho_{|n\rangle}(E) \pm \langle \sigma_z \rangle \cdot \Delta\rho_{spin,|n\rangle}(E) \pm \langle l_z \rangle \cdot \Delta\rho_{orbital,|n\rangle}(E)), \tag{1.5}$$

where the transition operator T and its expression in dipole approximation have been already discussed; ρ stands for the final density of states. Thus, the absorption coefficient is the sum of a constant part related to the presence of resonant edges and a variable part linked to the polarization of incoming photon. The dependence on the spin polarization has a different sign from edge L_2 to edge L_3, whereas the orbital one has the same, considering the $\Delta m = +1$ transitions; intuitively, to get the signal coming from the orbital polarization, one would have to properly sum the contributions coming from the two edges, whereas the difference should be taken to extract the spin dependent signal. Sum rules come as a consequence.
Sum rules are a quantitative tool to extrapolate expectation values of spin and orbital momentum projection on a quantization axis. Their aim is to separate spin and orbital contribution to XMCD. Considering two spin-orbit split edges, the sum rules are

$$\begin{gathered}
\frac{-\int_{j_+ + j_-}(\mu^+(E) - \mu^-(E))dE}{\int_{j_+ + j_-}(\mu^+(E) + \mu^-(E) + \mu^0(E))dE} = a\frac{\langle L_z\rangle}{n_h}, \\
\frac{-\int_{j_-}(\mu^+(E) - \mu-(E))dE - b\int_{j_-}(\mu^+(E) - \mu^-(E))dE}{\int_{j_+ + j_-}(\mu^+(E) + \mu^-(E) + \mu^0(E))dE} = \frac{c\langle S_z\rangle + d\langle T_z\rangle}{n_h},
\end{gathered} \tag{1.6}$$

where $\langle L_z\rangle$, $\langle S_z\rangle$ and $\langle T_z\rangle$ are the expectation values for spin, orbital angular moment and magnetic dipole term projection along the quantization axis. The latter takes into account the asphericity of the spin distribution, due to the environment around the atom, which lowers its symmetry from the spherical one. n_h stands for the number of initial holes in the valence shell. a, b, c and d are constants linked to the branching ratios of the transitions and ultimately come from the evaluation of the relative 3J symbols.
The denominator of both equations in 1.6 is the isotropic XAS spectrum over the two edges, i.e. the sum of spectra obtained with all the possible polarizations. Usually, in an XMCD experiment, it is estimated as $\mu^+ + \mu^- + \mu^0 \approx \mu^+ + \mu^- + (\mu^+ + \mu^-)/2 = 3(\mu^+ + \mu^-)/2$. The nominator in the two equations is instead the XMCD, i.e. the signal coming from the difference between the spectra μ^+ and μ^-, where the first is acquired with round circular polarization and magnetic field applied along +z and the latter with left polarization or with negative field. In sum rules 1.6, the XMCD signal is evaluated over both edges in the first one, whereas edge by edge in the latter, according to the fact that the orbital contribution displays the same sign over the two edges, while the spin contribution does not. Obviously, one has to remove from the signal what does not come from magnetic properties of the sample, e.g. a step like background must be erased by the spectra at each edge. Indeed, each time photon energy resonates with a core level, the photoelectron can be excited to the vacuum, so that any further amount of energy can bring to higher unbound states and will result in a nearly constant contribution to the absorption coefficient. Clearly, this contribution to the spectra is not related to the magnetism of the sample and if not properly removed can severely affect the evaluation of the integrals [16].

It is clear from the two-step model that the presence of an element lifting spherical symmetry is necessary, to have dichroism when dealing with circular polarized light. As well as circular, linear dichroism is expected when crystal field is present, due to the fact that electronic clouds of the ion are likely to orient along certain symmetry axes of the crystal. As a matter of fact, varying the experimental geometry, absorption events are likely to happen or not, e.g. the polarization of the incoming beam can be parallel or perpendicular to the electronic clouds; in the first case, absorption will take place whereas will not in the latter [10]. To this date, there is not an equivalent to sum rules for linear dichroism, still XLD experiments can be useful in revealing the presence of crystalline effects.
In the next section RIXS technique will be treated; the theory outlined for the XAS will be useful, to understand how the two techniques can be seen as complementary tools in a spectroscopic experiment.

1.2 Resonant Inelastic X-Ray Scattering (RIXS)

RIXS is a second-order optical process, since it involves a coherent absorption and emission of X-rays at resonance with electronic excitations [4, 8, 22, 23]. The incoming photon promotes a core electron and brings the electronic system to an excited state; therefore, after a characteristic time, the system will fill the core hole by emitting an X-ray photon. Being RIXS a photon-in photon-out spectroscopy technique, it opens the possibility in principle to measure variations of the energy, momentum and polarization of emitted photons with respect to incident ones, both in metals and insulators. These variations probe, in the end, excitations occurring in solids and can be measured under different external conditions: e.g. with applied electric or magnetic field and in applied high pressure as well [8, 24]. In the range of X-ray wavelengths, which is of relevance for the analysis of transition metal and rare earth compounds for instance, photons are much more energetic than any other probes, such as neutrons or electrons. As a result, the scattering phase space is much larger compared to the one of other techniques, e.g. photon scattering with visible and infrared light [22].
The RIXS cross-section is in the form

$$F(\omega_{in}, \omega_o) = \sum_f \left| \sum_n \frac{\langle f\,|T|\,n\rangle\,\langle n\,|T|\,g\rangle}{E_g + \hbar\omega_{in} - E_n - i\Gamma_n} \right|^2 \times \delta(E_g + \hbar\omega_{in} - E_f - \hbar\omega_o), \quad (1.7)$$

where $\hbar\omega_{in}$ and $\hbar\omega_o$ are the photon energies of the incoming and outgoing photon, respectively. g, n and f stand for the initial, intermediate and final states, along with their energies E_g, E_n and E_f. The same letters, labeling in XAS initial and final states, have been used to define initial and intermediate states in RIXS cross-section, for the first transition in resonant process is equivalent to an absorption event. The operator T represents the radiative transition and Γ_n the spectral broadening due to the core hole lifetime in the intermediate state. Finally, the δ function states the total energy conservation law, which along with the conservation of total linear and orbital momentum is crucial in deducing the properties of a sample from spectroscopic analysis.

As one can see from expression 1.7, RIXS spectrum is the sum of all the possible second order transitions. All the available transitions from the initial state g to an intermediate state n, due to a core electron excitation induced by an X-ray photon absorption of energy $\hbar\omega_{in}$, give a contribution to the intensity of the spectrum. For each of them, all the transitions towards a final state f due to an X-ray photon emission of energy $\hbar\omega_o$ must be taken into account. The real part of the denominator in eq. 1.7 vanishes, when the incoming photon energy is close to the core electron excitation threshold, thus leading to a strong intensity even if RIXS is a second-order process. This strong enhancement of the scattering section around the electronic edges, compared to the one of other techniques probing crystal field and magnetic excitations, such as Inelastic Neutron Scattering, allows to operate with small sample volumes, e.g. thin films, surfaces and objects at the nanoscale [25]. Therefore, the strong resonance character of RIXS opens up the opportunity to investigate low dimensional systems as well [26]. Nevertheless, RIXS, being a second-order scattering process, is a photon hungry technique; as a result, in order to collect meaningful information from RIXS spectra a state-of-the-art instrumentation is needed both in terms of the light source and of the detectors, as discussed in chapter 2.

Listing other advantages, it should be recalled that RIXS is an element and orbital specific technique, being indeed sensitive to crystal field environment around the selected ion. Due to the possibility of tuning the incoming photon energy, one can select the specific elemental edge to probe and the specific excitations, including the multiplets splittings due to the crystalline environment [27]. Furthermore, RIXS is a bulk sensitive technique as well, for in X-ray range the penetration depth is typically of the order of a few µm for hard X-rays and of 0.1 µm for the soft ones [22, 28]. The sensitivity to the surface can be enhanced by varying the incidence angle to a grazing one. Finally, in principle, a polarization analysis of the outgoing photons can be carried out, providing the user with information about the exchanged angular momentum between light and matter during the interaction [29]. As a result, one can yield from RIXS a symmetry characterization of the excitations occurring in solids [30, 31].

In the description of a RIXS process, in principle, one should take into account the superposition of two different scattering mechanisms: direct and indirect RIXS, the first being dominant when allowed, while the latter contributing only at higher orders [22].

Considering direct scattering, the deep core hole left by the electron excited into an empty state in the valence band is filled by one electron from the occupied states under the emission of an X-ray photon. As a result of the two-step process a valence excitation is created, whose energy and momentum is given by the difference between the ones carried in by the incoming photon and those taken out by the exiting X-ray. The direct RIXS mechanism to occur requires both transitions to be allowed and considering electric dipole transition rules, M edge of rare earth compounds can safely be claimed to fulfill this requirement. In case of a low probability for the direct transition to occur, e.g.

the two processes are forbidden by electric dipole rules, indirect transitions can become relevant. In indirect transition case, the electron core is promoted in a strong excited level in the intermediate state, i.e. several electron volts above the Fermi level. The strong potential exerted by the core hole is felt by valence electrons which are scattered in a way that electron-hole excitations are created in the valence band. Finally, the strongly excited electron decays to fill the core hole, leaving behind the electron-hole valence excitation. Thus, indirect transitions are due to the strong core hole potential and their analysis can provide information about the solids in the heavily excited intermediate state. Finally, the fact that both scattering mechanisms can contribute to the intensity of RIXS spectra should be stressed. However, when allowed, direct mechanism has a much higher cross-section with respect to the higher order process of indirect event and one can focus the analysis on the first type of scattering.
A sketch of the described mechanisms is displayed in figures 1.2 and 1.3.

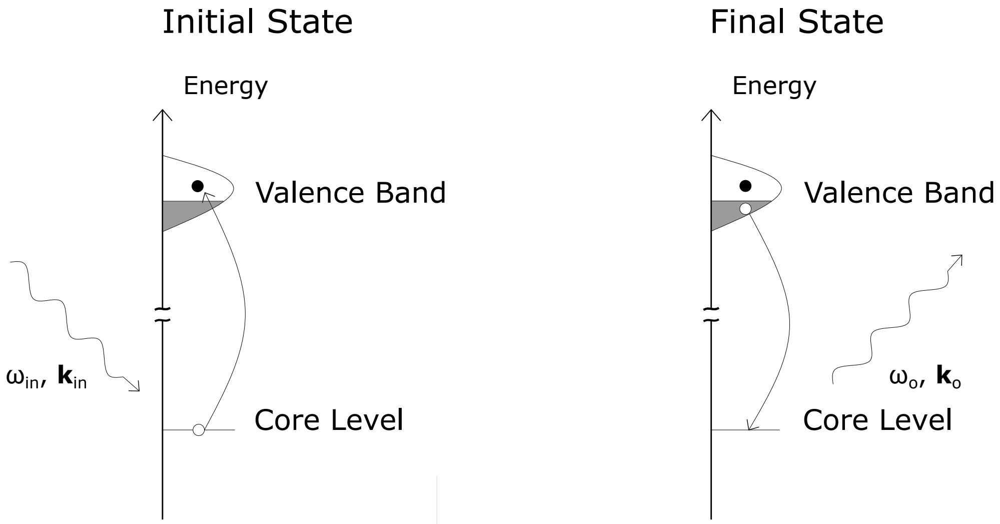

FIGURE 1.2: Direct RIXS scattering. A core electron is excited into the empty valence band, then, within few *fs*, the core hole is filled by an electron from an occupied state in the valence band. In the end, a valence excitation has been created with momentum $\hbar\mathbf{k}_o - \hbar\mathbf{k}_{in}$ and energy $\hbar\omega_{in} - \hbar\omega_o$. Image redrawn from [22].

After having introduced, at least in a qualitative way, the scattering mechanisms during a RIXS process, is appropriate to move further on to the two possible classes of inelastic energy loss features. Then, are defined as Raman features those in which the energy transferred $\hbar\omega$ to the solid is independent of the incoming photon energy $\hbar\omega_{in}$. In other words, the energy of the outgoing photon $\hbar\omega_o$ increases of the same amount as the energy of the incident one $\hbar\omega_{in}$. Whereas, one can define as X-ray emission or X-ray fluorescence features those which show no dependence of the energy of the outgoing photon on the incident energy, thus requiring only the core hole to be created by the incoming

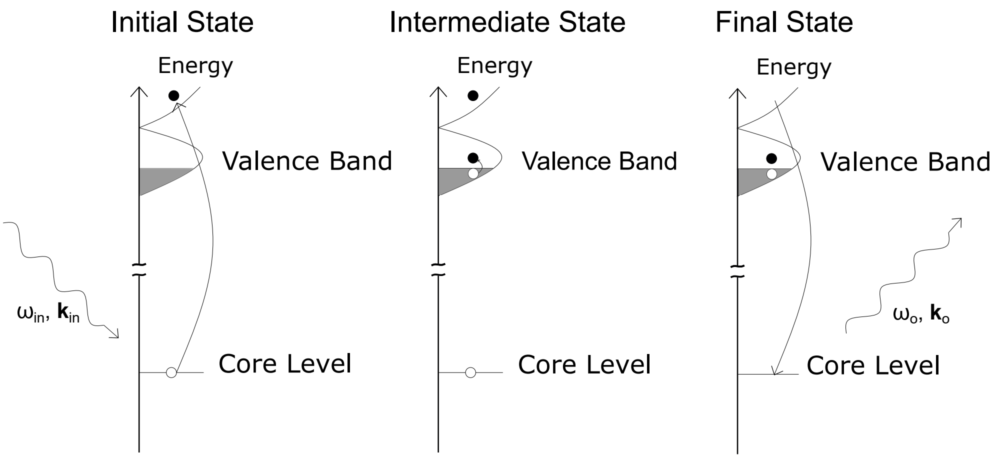

FIGURE 1.3: Indirect RIXS scattering. A core electron is excited into an empty valence state far above Fermi level. Electrons in the occupied states of the valence band are scattered by the electrostatic potential originating from the core hole into the empty states. The photoelectron, then, decays emitting an X-ray photon. In the end, as in the case of direct RIXS process, a valence excitation has been created with momentum $\hbar\mathbf{k}_o - \hbar\mathbf{k}_{in}$ and energy $\hbar\omega_{in} - \hbar\omega_o$. Image redrawn from [22].

radiation. Therefore, in the energy conservation equation $\hbar\omega_{in} = \hbar\omega + \hbar\omega_o$, the Raman features will stand for the ones in which the energy loss $\hbar\omega$ is constant with respect to incoming energy $\hbar\omega_{in}$, while the fluorescence class is characterized by having the outgoing photon energy $\hbar\omega_o$ constant. Since, for the occurrence of the second class features, it is only necessary to have a core hole, all the possible intermediate states in which the photoelectron is excited to the vacuum can contribute to this RIXS feature class and information about the intermediate state is lost. Thus, Raman features are more relevant in a RIXS experiment, for they can provide a full description of elementary excitations in solids and their analysis is in principle simpler.

1.2.1 Theoretical fundamentals

In order to derive a justification for eq. 1.7, the theoretical aspects of RIXS will be deepened.
Considering the initial state g with energy E_g and the final state f with energy E_f, the intensity of RIXS transition 1.7 can be rewritten as

$$\begin{aligned} I(\omega_{in}, \omega_o, \mathbf{k}_{in}, \mathbf{k}_o, \epsilon_{in}, \epsilon_o) = \sum_f \left| \mathcal{F}_{fg}(\omega_{in}, \omega_o, \mathbf{k}_{in}, \mathbf{k}_o, \epsilon_{in}, \epsilon_o) \right|^2 \times \\ \delta(E_f + \hbar\omega_o - E_g - \hbar\omega_{in}), \end{aligned} \tag{1.8}$$

with ω_{in}, $\mathbf{k}_{in}$ and ϵ_{in} being the energy, momentum and polarization of the incident photon and ω_o, $\mathbf{k}_o$ and ϵ_o the ones of the outgoing X-ray. As the reader can see, the intensity is the product of an amplitude factor $\mathcal{F}_{fg}$ and a δ term,

again for energy conservation purpose. The amplitude factor depends on the probed excitations, being function of ω_{in} and ω_o, and on the experimental geometry, due to the dependence on polarization and wavevector, .
With the aim of obtaining the transition rate probability in a RIXS process, which will lead to eq. 1.7, one should start writing the Hamiltonian for N atomic electrons interacting with the electromagnetic field of synchrotron radiation. In the non-relativistic limit and small potentials approximation, i.e. the electrons potential ϕ and the photons vector one $\mathbf{A}$ are small compared to the rest energy of electrons, $e\phi/2mc^2$, $e\left|\mathbf{A}\right|/2mc \ll 1$, one can write

$$\begin{aligned}\mathcal{H} = \sum_{i=1}^{N} \Bigg(& \frac{[\mathbf{p}_i + \mathbf{A}(\mathbf{r}_i)]^2}{2m} + \frac{e\hbar}{2m}\sigma_i \cdot \mathbf{B}(\mathbf{r}_i) + \\ & \frac{e\hbar}{2(2mc)^2}\sigma_i \cdot \{\mathbf{E}(\mathbf{r}_i) \times [\mathbf{p}_i + e\mathbf{A}(\mathbf{r}_i)] - [\mathbf{p}_i + e\mathbf{A}(\mathbf{r}_i)] \times \mathbf{E}(\mathbf{r}_i)\}\Bigg) + \\ & \frac{e\hbar^2\rho(\mathbf{r}_i)}{8(mc)^2\epsilon_0} + \mathcal{H}_{Coulomb} + \sum_{\mathbf{k},\epsilon} \hbar\omega_{\mathbf{k}}(a^{\dagger}_{\mathbf{k}\epsilon}a_{\mathbf{k}\epsilon} + \frac{1}{2}),\end{aligned} \tag{1.9}$$

where $\mathbf{p}_i$, $\mathbf{r}_i$ and σ_i represent the momentum, position and the Pauli matrix of electron i. $\mathbf{A}$ is the vector potential; the electric field can be expressed as $\mathbf{E}(\mathbf{r}_i) = -\nabla\phi - \partial\mathbf{A}/\partial t$ and the magnetic one as $\mathbf{B}(\mathbf{r}_i) = \nabla \times \mathbf{A}$. In a second quantization formalism, the last term through the use of creation $a^{\dagger}_{\mathbf{k}\epsilon}$ and annhilation $a_{\mathbf{k}\epsilon}$ operators, stands for the photons term. The photons term is the sum of the energy associated to all the modes $\mathbf{k}$ multiplied by the number of photons in each mode and polarization states, plus the zero point energy $\hbar\omega_{\mathbf{k}}/2$. The first term of eq. 1.9 is the kinetic energy of electrons in presence of an electromagnetic field. The second term is the Zeeman term, responsible of multiplet splittings when a static magnetic field is applied. The third term describes the spin-orbit interaction coupling. the fourth contribution is the fine structure Darwin term and relevant only when dealing with s orbitals, for they do not decay when approaching the nuclear coordinates: for the purpose of this work, dealing with d and f orbitals, it will be neglected. Finally, a Coulomb term has been introduced to account for the interaction of electron with any electric potential, including the one due to the presence of other electrons and the nuclei.
Hence, the idea is to split up the Hamiltonian $\mathcal{H}$ in two major pieces: $\mathcal{H}_0 = \mathcal{H}_{el} + \mathcal{H}_{ph}$. Thus, the system is represented as the sum of an electronic term and an electromagnetic one, as if they do not interact with each other, and $\mathcal{H}'$, which stands for the contribution coming from the interaction of the two systems. As a result, one can write the Hamiltonian in eq. 1.9 as $\mathcal{H} = \mathcal{H}_0 + \mathcal{H}'$ and treat the interaction term as a perturbation to $\mathcal{H}_0$. Only the contributions which show a linear dependence on $\mathbf{A}$ in eq. 1.9 are relevant in a two-photon resonant process, so that the interaction Hamiltonian is

$$\mathcal{H}' = \sum_{i=1}^{N} \left[\frac{e}{m}\mathbf{A}(\mathbf{r}_i) \cdot \mathbf{p}_i + \frac{e\hbar}{2m}\sigma_i \cdot \nabla \times \mathbf{A}(\mathbf{r}_i)\right], \tag{1.10}$$

where the Coulomb gauge was fixed, i.e. $\nabla \mathbf{A}(\mathbf{r}_i) = 0$, i.e. $[\mathbf{A}, \mathbf{p}] = 0$. The first addend is a non-magnetic term, while the second one is related to a Zeeman like interaction: the magnetic term will be neglected from now on, since it is estimated to be smaller by a factor 10^{-2} with respect to the non-magnetic one. Applying the perturbative approach and expanding Fermi's golden rule to the second order, for the transition from an initial state $|\mathrm{g}\rangle = |g;\, \hbar\omega_{in}, \mathbf{k}, \boldsymbol{\epsilon}\rangle$ to a final state $|\mathrm{f}\rangle = |f;\, \hbar\omega_o, \mathbf{k}', \boldsymbol{\epsilon}'\rangle$ the rate probability is

$$w = \frac{2\pi}{\hbar} \sum_{\mathrm{f}} \left| \langle \mathrm{f}|\mathcal{H}'|\mathrm{g}\rangle + \sum_{\mathrm{n}} \frac{\langle \mathrm{f}|\mathcal{H}'|\mathrm{n}\rangle \langle \mathrm{n}|\mathcal{H}'|\mathrm{g}\rangle}{E_{\mathrm{g}} - E_{\mathrm{n}}} \right|^2 \times \delta(E_{\mathrm{f}} - E_{\mathrm{g}}) \tag{1.11}$$

The photon is scattered from the state at energy $\hbar\omega_{in}$, momentum $\hbar\mathbf{k}_{in}$ and polarization $\boldsymbol{\epsilon}_{in}$ to the final one at $\hbar\omega_o$, $\hbar\mathbf{k}_o$ and $\boldsymbol{\epsilon}_o$, bringing the electronic system from the state $|g\rangle$ to $|f\rangle$. The first order term of eq. 1.11 is related to non-resonant scattering, whereas the second order term, through its denominator energy dependence, is enhanced when the incident photon energy is close to a resonant edge. Expanding the vector potential in plane waves, i.e. $\mathbf{A}(\mathbf{r}) = \sum_{\mathbf{k}\boldsymbol{\epsilon}} \sqrt{\frac{\hbar}{2V\epsilon_0\omega_{\mathbf{k}}}} (\mathbf{A}_{\mathbf{k}\boldsymbol{\epsilon}} e^{i\mathbf{k}\mathbf{r}} + \mathbf{A}^{\dagger}_{\mathbf{k}\boldsymbol{\epsilon}} e^{-i\mathbf{k}\mathbf{r}})$, V being the volume of the system and $\mathbf{A}_{\mathbf{k}\boldsymbol{\epsilon}}$ each mode amplitude, one can write the resonant part of eq. 1.11 and the amplitude of eq. 1.8 as

$$\mathcal{F}_{fg} = \frac{e^2\hbar}{2m^2V\epsilon_0\sqrt{\omega_{in}\omega_o}} \sum_n \sum_{i,j=1}^{N} \frac{\langle f|\boldsymbol{\epsilon}_o^* \cdot \mathbf{p}_i e^{-i\mathbf{k}_o\mathbf{r}_i}|n\rangle \langle n|\boldsymbol{\epsilon}_{in} \cdot \mathbf{p}_j e^{i\mathbf{k}_{in}\mathbf{r}_j}|g\rangle}{E_g + \hbar\omega_{in} - E_n + i\Gamma_n}. \tag{1.12}$$

Thus, the transition operator in eq. 1.7 is $T = C\sum_{i=1}^{N} e^{i\mathbf{k}_{in}\mathbf{r}_i} \boldsymbol{\epsilon}_{in} \cdot \mathbf{p}_i$ and, finally, one gets

$$\mathcal{F}_{fg}(\omega_{in}, \omega_o, \mathbf{k}_{in}, \mathbf{k}_o, \boldsymbol{\epsilon}_{in}, \boldsymbol{\epsilon}_o) = \sum_n \frac{\langle f|T^{\dagger}|n\rangle \langle n|T|g\rangle}{E_g + \hbar\omega_{in} - E_n + i\Gamma_n}, \tag{1.13}$$

which links eqs. 1.8 and 1.7.

Exploiting Green's function formalism, $\mathcal{F}_{fg}$ can be written in a more compact way as $\mathcal{F}_{fg} = \langle f|T^{\dagger}GT|g\rangle$, where $G = \sum_n \frac{|n\rangle\langle n|}{E_g + \hbar\omega_{in} - E_n + i\Gamma}$ is called the intermediate state propagator. The propagator G is intrinsically connected to the intermediate state Hamiltonian; therefore, one can express it as the sum of an unperturbed term and one related to the core hole Hamiltonian, i.e. the interaction arising from the exciton in the intermediate state, $G = G_0 + G_0 H_c G$ and straightforward write the scattering amplitudes for both direct and indirect RIXS mechanisms, depicted in figures 1.2 and 1.3:

$$\mathcal{F}_{fg}^{direct} = \langle f|T^{\dagger}G_0T|g\rangle \tag{1.14}$$

and

$$\mathcal{F}_{fg}^{indirect} = \langle f|T^{\dagger}G_0H_cGT|g\rangle. \tag{1.15}$$

A final remark about the definition is appropriate. Equations 1.8 and 1.13, which in the end combine to build up expression 1.7, are usually referred to as Kramers-Heisenberg formulas. They date back to 1925 [32], just before the conventional advent of quantum physics and the theory about photon transitions afterwards developed, including the perturbation theory and the derivation of Fermi's golden rule. Their purpose was to describe stimulated emission and inelastic scattering, anticipating the discovery of Raman effect. As shown, they can describe RIXS scattering mechanism as well.
That concludes the chapter about the exploited spectroscopic experimental techniques in this work.
In the next chapter, the reader will get a grasp of how a state-of-the-art beamline dealing with soft X-rays spectroscopy is designed.

Chapter 2

Beamline ID32 at ESRF

Conceived and built as a part of phase I ESRF Upgrade, the ID32 is a state-of-the-art beamline for XMCD and RIXS soft X-ray experiments, covering the energy range 400 eV $\div$ 1600 eV. This energy interval allows to scan over different elements absorption edge, e.g. light elements K-edges, 3d transition metals $L_{2,3}$ and 4f rare earths $M_{4,5}$ ones, directly probing magnetic features due to the not-full valence shell. The beamline is split up into two branches; one dedicated to XMCD and external users experiments and one to high resolution RIXS.
In this chapter, after a brief description of a synchrotron facility, with a focus on ESRF, a technical description of the design of the beamline will be given, stressing how technological issues have been tackled to achieve the aim of providing the user with high stability, fast acquisition time and never achieved before resolution.
Concerning the description of ID32 beamline the following description is mainly based on [5, 33], the latter focusing on the XMCD branch.

2.1 Light source: ESRF, a brilliant synchrotron radiation facility

Before going into the details of the beamline itself, a brief insight on synchrotron radiation and its sources will be given, focusing on ESRF.
High energetic moving electrons that are subjected to an acceleration can emit radiation in the X-ray range [9, 16]. Thus, the working principle of a synchrotron machine is based on the idea that electrons moving on a circular trajectory get continuously accelerated. The ESRF facility follows a general design for synchrotron machines, being made of a preliminary linear accelerator (Linac), a booster synchrotron and the storage ring [34]. The aim of the Linac is to accelerate the electrons coming from an electron gun to 200 MeV by means of linear arranged and electric fields based optics and to provide them as bunches to the booster. Increasing the energy of electrons, magnetic fields become much more effective with respect to electric ones in modifying electronic trajectories; indeed, the Lorentz force scales with the velocity of the charge particle whereas the electric one is constant. Therefore, the booster is a 300 m long ring, made of magnetic optics, whose aim is to bring electrons to the 6 GeV target energy, before injection in the storage ring. Going further, the

storage ring is a a tube 844 m in circumference where electrons are kept in trajectory close to the speed of light. Ultra high vacuum is required in the cavity in order to avoid impact between electrons and impurities which may cause creation of high energetic positive ions and electrons energy losses; thus, the tube is maintained at around 1×10^{-9} mbar. Finally, the radiation resulting from the bending of electronic trajectories is provided to beamlines in order to perform experiments.
A sketch of the ESRF facility is provided in figure 2.1.

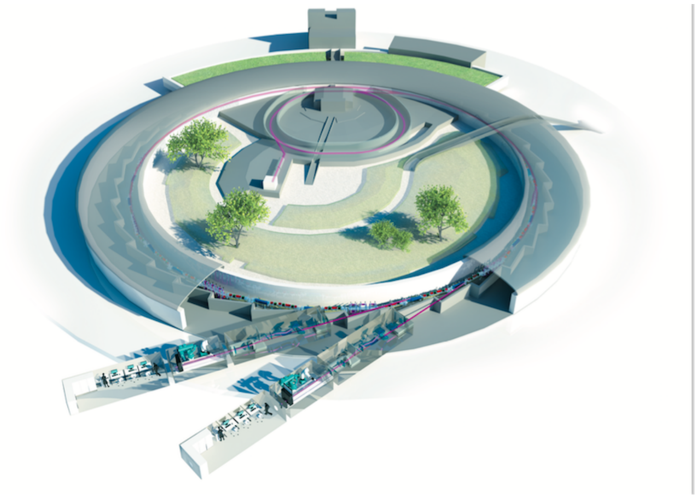

FIGURE 2.1: Layout of ESRF. In the figure the trajectory followed by the bunches of electrons is highlighted. They are generated by the electron gun, linearly accelerated by the Linac, brought to the target energy and injected in the storage ring by the booster synchrotron. Finally, photons by undulators and bending magnets are provided to the beamlines. Image from www.esrf.eu.

Along the storage ring, the magnetic optics are arranged in 32 alternating straight and curved sections.
Bending magnets are placed in the curve sections; keeping electrons in their circular trajectory, they are responsible for the production of synchrotron radiation. However, since electrons passing in a bending magnet are subject to a continuous acceleration the radiation coming from these devices is characterized by a poor brilliance compared to the one achieved by more sophisticated devices, such as undulators, both in terms of the energy band and of focusing power [9, 16]. Whereas, in the straight sections refocusing magnets and insertion devices, i.e. undulators, are placed. The task of the first is to cope with the space-charge effects, which can ultimately lead to loss of spatial and temporal coherence of the beam. Then, alternating quadrupoles and sextupoles magnets keep electrons as close as possible to the ideal orbital path. The latter instead are arrays of small magnets which force the electrons to undergo rapid oscillations in space. Due to this motion, electrons can emit photons which sum in phase over a small energy range and are focused on a small solid angle. Moreover, depending on the arrangement of magnets in the arrays, in particular on the relative spatial phase difference among them, the light can be linearly or

circularly polarized with a degree of polarization close to 100% [16]. Thus, undulators are currently employed in third generation synchrotron facilities. The graph in figure 2.2 displays the brilliance of several X-ray sources in history along with the current value and the prediction for ESRF after EBS (Extremely Bright Source) upgrade [35].

Following the same path as photons coming from the storage ring, in the next section a detailed description of ID32 beamline at ESRF will be provided; starting with the optics hutch where photons coming from ID32 dedicated undulators are delivered, the optics common to the two branches will be described.

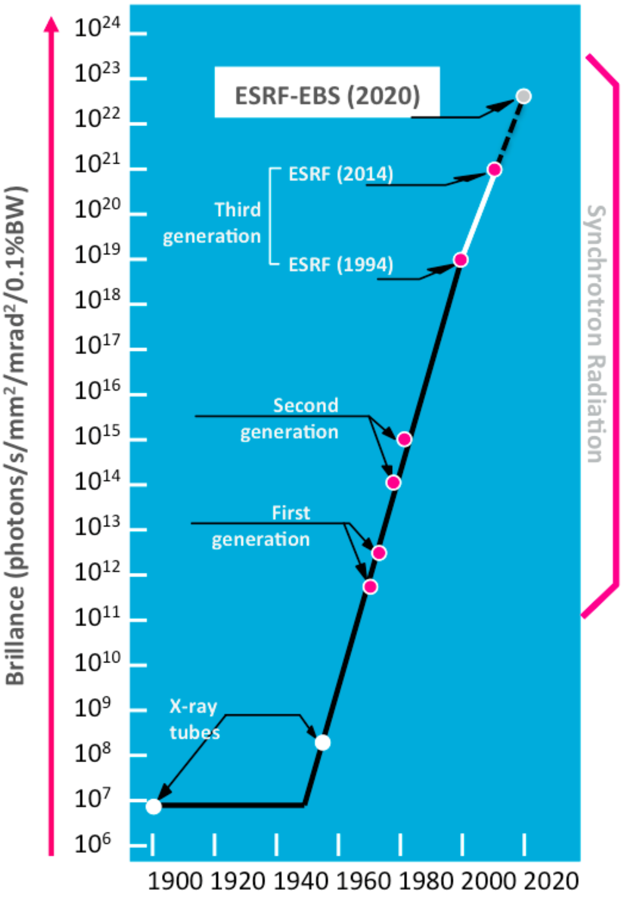

FIGURE 2.2: Brilliance of X-ray sources in history. Following the time line: the first X-ray tubes; the first generation synchrotron, where bending magnets were employed for the first time with the purpose of radiation production; the second generation ones, characterized by the use of wigglers, forerunners of the modern undulators exploited by the third generation sources. Finally, an estimation for ESRF after EBS (Extremely Bright Source) upgrade. Image from www.esrf.eu.

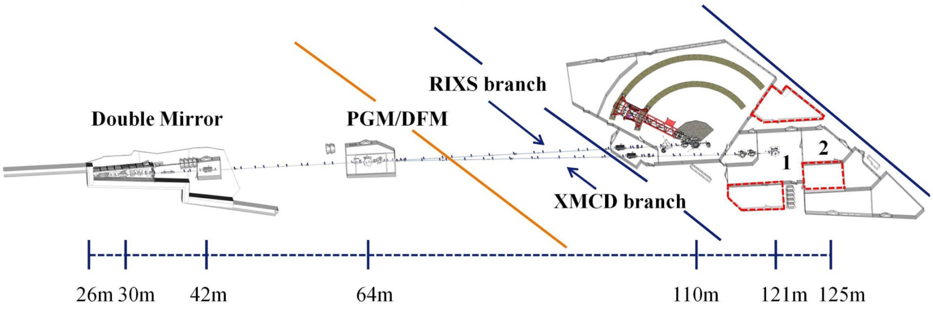

FIGURE 2.3: ID32 beamline floor plan. Distances of each component is given taking the centre of ID32 straight section as a reference. The two branches are pointed out. Highlighted in red the long arm RIXS spectrometer and the control cabins: one for the RIXS branch, two for the XMCD one, for the main endstation and the external users' experiments one respectively. Image taken from [5].

2.2 Optics hutch

To achieve the double aim of having a tunable polarization and a high flux light, ID32 dedicated straight section hosts three undulators APPLE-II [36].
These undulators allow a close to 100% polarization, both linear in two perpendicular planes and circular right and left, over the energy range 400 eV ÷ 1600 eV. Radiation exiting from undulators is characterized by an elliptical section, with the size in the horizontal plane being one order of magnitude larger than the one in the perpendicular vertical plane and with a higher divergence as well. The undulators are spatially arranged in order to provide a radiation whose first harmonic covers the soft X-ray range. Being the photons highly absorbed at this energy, pressure of 2×10^{-9} mbar is required; therefore, the entire beamline is connected with the Ultra High Vacuum of the storage ring and ID32 is a windowless beamline.
In figure 2.3 a sketch of ID32 floor plan is provided.

A double mirror device is placed at the entrance of the optics hutch, in order to obtain a beam parallel to the one coming from the storage ring but shifted of 16 mm in the horizontal plane and to install a Bremsstrahlung stop to filter out higher energy photons. Moreover, the mirrors reduce the heat load on the monochromator, absorbing unwanted higher energy radiation as well. Their position can be adjusted by the user acting on the hexapod support which performs six degrees of freedom movements.
Out of the double mirror, the beam is focused in the vertical direction and collimated in the horizontal one by a toroidal mirror, before reaching a plane grating monochromator (PGM) in the vertical direction. Since radiation falls in the soft X-ray range, it is not possible to exploit crystal optics as monochromators, currently used in hard X-ray beamlines; therefore, artificial periodic structures designed for higher soft X-ray wavelenghts are employed.
When performing a spectroscopic experiment, one of the major challenge is scanning over a wide range of energies with the same degree of monochromaticity. To fulfill this requirement, ID32 employs two variable line spacing

(VLS) plane gratings for each branch: one characterized by a higher resolution power, the latter designed to work in a medium resolution setup, conceived to increase the throughput. A pre-mirror, in front of the gratings, performs the task of keeping the beam spot at the centre of them; the energy of the beam is selected by rotating the gratings about their axis, i.e. selecting the order of diffraction. Undulator gap is scanned as well to ensure an approximately constant flux across the scan.
A scheme of the optical components of the two branches is proposed in 2.4 up to the refocusing optics, along with the listed distances with respect to the dedicated straight section.
In the next section, we will go into the details of the description of the XMCD branch.

2.3 XMCD branch

2.3.1 XMCD optics

For the XMCD branch two gratings are available: a resolving power of 5000 is achieved with the 300 l/mm one, whereas with the 900 l/mm groove density one is possible to obtain a resolving power higher than 10000 over the entire energy range. The selection is a trade-off between resolution and intensity, keeping also in mind that with the higher density grating setup measurements the insensitivity to angular changes is improved, due to the higher degree of dispersion achieved.
A cylindrical deflecting mirror (DFM) is placed after the monochromator to focus the beam at the exit slit of the gratings and to guide it in the XMCD branch; this mirror is mechanically removed as RIXS measurements are taken.
Finally, before the sample chambers, refocusing optics are in charge of adjusting the beam size. It is possible to focus the beam in both the end stations, the main one and the one committed to special experiments of external users, or to defocus it when a high flux is unwanted on the sample to prevent damage. Focusing in the horizontal and vertical direction is achieved by two elliptically bent cylindrical mirrors, horizontal refocusing mirror (HRM) and vertical refocusing mirror (VRM): beam size can be tuned from $\sim$100 µm × 10 µm to $\sim$2000 µm × 800 µm (H×V). A refocusing plane mirror (RPM) keeps the beam in the horizontal plane common to all beamlines at a height of $\sim$1.4 m. Out of it, thin conductive (B-doped) diamond films [37] are placed to measure the intensity of the flux before the sample; this signal is used to apply a proper normalization to spectra with respect to incident photon flux.

2.3.2 XMCD endstation

The core of XMCD branch of ID32 is its UHV high-field superconducting magnet [33]. It is made of two sets of split-pair superconducting coils which can generate a magnetic field up to 9 T along the beam direction and up to 4 T in the orthogonal direction. The superconducting coils are kept in a liquid-He (LHe) bath keeping them at 4.2 K, i.e. below the critical temperature for the

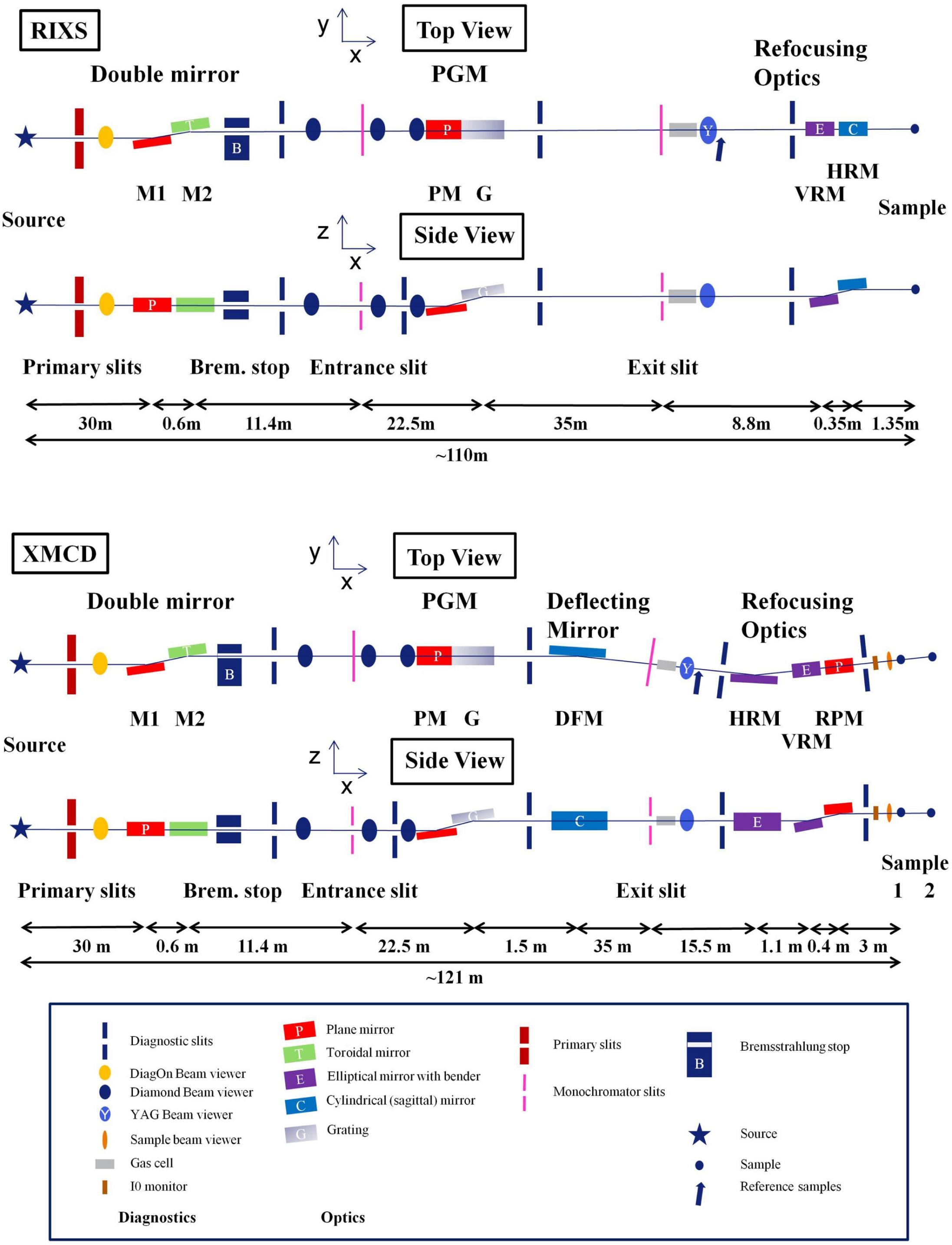

FIGURE 2.4: Optical layout for the two branches up to the refocusing optics. All the components are listed in the legend. In particular, beyond the components treated in the text, diagnostic tools are present at ID32. Beam viewer and diagnostic slits, which are open during experiments, are useful in aligning the beam and properly adjusting position of each optical element. Primary slits select the portion of the beam close to the optical axis, whereas monochromator slits fix the diffraction order. Slits are present also before the sample to define the hit portion. Finally, a gas cell is present to perform XAS measurement and estimate beamline energy resolution on well known gas edges. Image taken from [5].

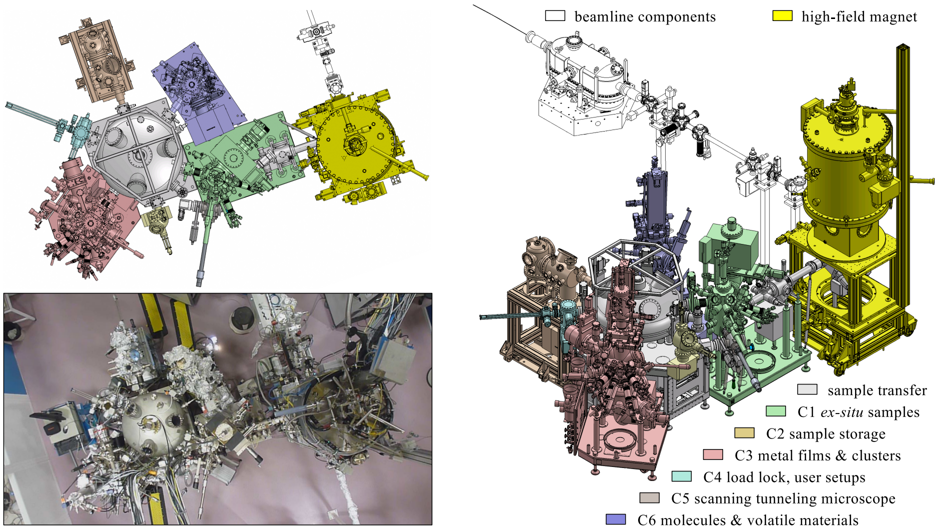

FIGURE 2.5: XMCD station. In figure the high-field superconducting magnet and the cluster of the six UHV chambers is highlighted. *C1* allows loading, storing and basic preparation of ex situ samples. *C2* is a sample storage for up to 20 sample plates. *C3* is committed to the growth and characterization of metal and oxide films and clusters. *C4* allows two sample to be loaded at a time; it is connected to the transfer system of the six chambers. *C5* hosts a scanning tunnelling microscope for characterization. *C6* is dedicated to the deposition of molecules and other volatile materials. Image taken from [33].

transition phase from the superconducting state to the normal one. As well as the magnet, a cluster of six UHV chambers connected to the magnet sets up the endstation; sample can be prepared, characterized and transferred to the magnet being in UHV, i.e. with negligible surface contamination. During experiments, indeed, the pressure in the magnet is typically in the 1×10^{-11} mbar regime. A scheme of the six chambers along with the magnet is provided in 2.5, together with a picture from the top view of the station.

Spectra are acquired exploiting the total electron yield (TEY) method [9]. As a result of a photon absorption event an electron-hole pair is created in the material; in the TEY method, all the electrons exiting the sample are measured. The signal is acquired by measuring the drain current from the sample by a detector put above the sample. The detected signal is the sum of Auger and secondary electrons collected; the first being very sensitive to the surface, the latter being the result of cascade processes. The mixing of these two effects leads to a probing depth with a lower boundary set by the Auger typical depth, i.e. $\sim$20 Å and an upper one of $\sim$200 Å [9]. Despite the uncertainty on probing depth, among other detection techniques, the TEY is characterized by ease of acquisition and a large signal, which make it the most exploited one. However, in ID32 it is possible to perform also measurements in total fluorescence yield (TFY) mode, where photons coming from the sample as a result of the fluorescence decay channel for the core hole are detected. On one side, photons exiting the sample have the same mean free path of the incident ones, i.e.

the probing depth is somehow only set by the beam energy, on the other side, saturation effects arise. When strong resonances are present fluorescence photons are likely to be reabsorbed in the sample; as a result, the spectra show to be flattened at highest peaks energy. The photodiode for TFY measurements is mounted at 90° with respect to the incident beam.

The magnet is equipped with a He^4 continuous-flow cryostat, allowing the sample to be brought down to 5 K. A resistive heater allows temperature control with a PID control loop on temperature sensors; both the heater and the sensors are properly electrically insulated to avoid introduction of noise in the detected signal. The temperature at the sample position can be set at any value from 5 K to a maximum of 320 K; ramp rates and temperature stabilization can be controlled with the heater with a typical time of stabilization in the order of 20 min.

Research about molecular magnets, topological insulator, magnetic impurities, exchange bias systems and single-crystalline systems have been carried out by external users at XMCD endstation. For the purpose of this work, the possibility to take measurements of the magnetization by integrating XMCD signal has been exploited. Further details, along with practical case studies and future perspectives can be found in [33].

In the next section, a description of RIXS branch will be given.

2.4 RIXS branch

2.4.1 RIXS optics

As for XMCD branch, also for RIXS two gratings are available at the PGM: one with a groove density of 800 l/mm for medium resolution and high throughput and another one with 1600 l/mm for high resolution measurements. The refocusing optics include a bent elliptical mirror for refocusing in the vertical plane (VRM) and a cylindrical HRM acting in the horizontal direction; the spot size at the sample is typically 3 µm ÷ 4 µm FWHM Gaussian shaped in the vertical direction and ∼35 µm in the horizontal one. Since photons having different energies are dispersed in the vertical plane, the constrain of the spot size is on this direction; indeed, the source size sets the limit in energy resolution. Finally, the last mirror before the sample is kept electrically isolated in order to use it as an intensity mirror, by measuring the drain current.

2.4.2 RIXS sample stage

Sample is hosted in a 711 mm diameter UHV chamber on a four-circle UHV diffractometer and kept electrically insulated, in order to perform TEY measurements, collecting the drain current. The stage can rotate about the vertical axis, i.e. the one normal to the horizontal plane of ID32, of an angle θ in the range $(-20°; 185°)$: θ is equal to 0° when the sample surface is parallel to the incident beam and 90° when the beam hits the surface perpendicularly. On top of it, two independent stages provide a ±45° χ and a 180° ϕ rotation. χ

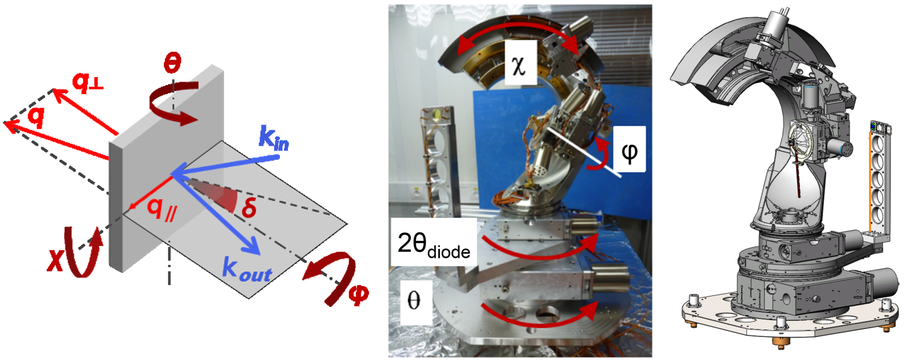

FIGURE 2.6: The four-circular diffractometer sketch, along with a picture and a definition of the experimental angles. Image taken from [4].

stands for the rotation of the sample about the axis defined by the intersection between the sample surface and the scattering plane, i.e. the plane containing the incident beam and the outgoing photons: it is set to -90° when the two planes are perpendicular. ϕ represents rotations about the axis normal to the sample surface: it is equal to 45° when the plane defined by χ and ϕ axes coincides with the horizontal plane of the beamline. Detector is provided with a 2θ (-10°; 175°) motion sharing the same vertical axis as the sample but fully independent from it: the angle 2θ is defined as the angle between the incoming beam and the direction selected by the user to analyze. In figure 2.6 ID32 diffractometer is displayed, along with the definition of the experimental angles.

Typically, during experiments, the sample temperature is set by a liquid Helium flow cryostat, fully compatible with UHV conditions; a sample temperature of 20 K is easily achieved. The presence of the cryostat limits ϕ to the range $-45^\circ \div 135^\circ$, whereas χ and θ dynamics are still fully exploitable.

2.4.3 ERIXS: the spectrometer

The aim of RIXS branch is to achieve an overall resolving power of ~30000 at Cu L_3 edge in high resolution setup and ~17000 in medium resolution one. In order to reach these targets, a state-of-the-art spectrometer is necessary, whose performances should match the beamline ones. Moreover, as explained in chapter 1, a dispersion and polarization analysis can yield interesting information in RIXS experiments; therefore, the spectrometer should rotate in the plane and host a module for the measurement of polarization resolved high resolution spectra. At the same conditions of spot size at the sample, grating line density and detector spatial resolution, the bandwidth of the spectrometer is proportional to the inverse of the distance between the sample and the detector. As a result, ERIXS spectrometer has been designed to be 12 m long, with a continuous variation of the scattering angle over 100° and a purposeful detector for polarization analysis. A picture of the huge structure is proposed in 2.7.

On the one hand, the long exit arm of the spectrometer, in combination with

the high degree of monochromaticity of the source, allows to match the wanted energy resolution targets, on the other side, rotating such a huge structure to allow dispersion analysis is a non trivial technological issue. The heavy structure lies on 8 airpads in order to lift the scattering arm up to 70 µm from the rest position and to let it slide on two concentric granite guides. The motion over 100° range is performed by a circular rail mounted close to the sample chamber and a small stepper motor at the end of the steel structure.
The mechanical arm is composed of three vacuum chambers.

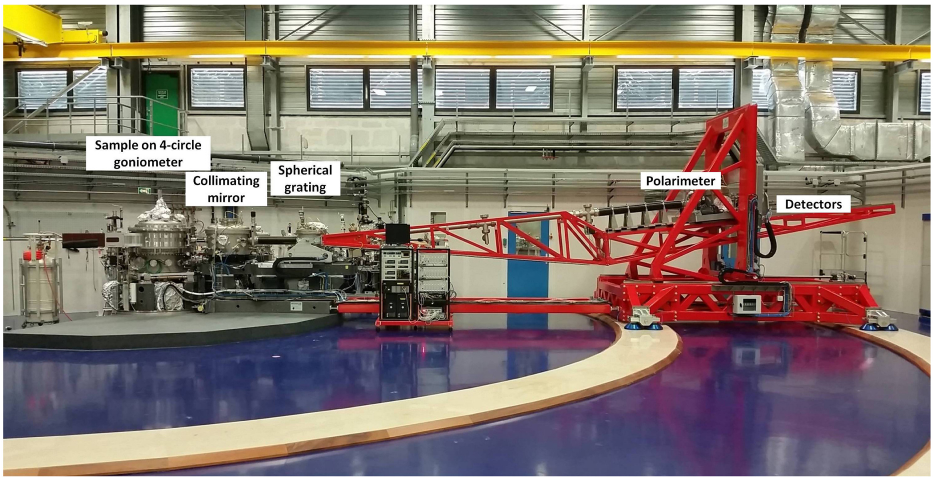

FIGURE 2.7: The 12 m long steel structure. The position of the main components is pointed out. Notably, the sample holder, i.e. the four-circle diffractometer, a collimating spherical mirror to increase acceptance angle in horizontal direction, a spherical grating to disperse photons coming from the sample and the detectors, for direct and polarized light. Image taken from [5].

The first one hosts a parabolic mirror whose purpose is to increase the acceptance angle from the sample up to ∼20 mrad in horizontal direction, in order to cope with the signal loss. Indeed, due to the high dispersion of the following monochromator and the small solid angle of the detector, which scales as the inverse of the squared length of the arm, a degradation of the intensity may occur.
The second chamber contains two VLS spherical gratings scattering the photons coming from the sample in the vertical direction. Therefore, the signal at the detector is a series of horizontal lines, each line being at a different energy. Two gratings are available, one for high resolution and one for high flux experiments, the first being 2500 l/mm dense, the latter 1400 l/mm; both matches the relative configuration of the beamline in achieving the target resolution. In particular, three configurations are typically used: high flux, exploiting the low density gratings, both in the monochromator and in the spectrometer, with an energy resolution of 56 meV at the reference energy of Cu L_3 edge, i.e. 932 eV; a medium one, using the low line density beamline grating and the high density one in the spectrometer, reaches a better resolution of ∼41 meV; a high resolution (∼30 meV) is achieved, exploiting both high density gratings.
In the third chamber, at the end of the steel arm, two detectors are located

one for the direct beam and one committed to the polarization analysis. Polarization optics reflect the polarized beam to the proper detector; the reflected polarized beam is obtained at the cost of a factor 10 in intensity with respect to the isotropic beam and without any loss in energy resolution.
The detectors used are 2D position sensitive CCD cameras. RIXS spectra are acquired by integration of the isoenergetic horizontal lines, i.e. a parallel acquisition of the whole energy range is performed. A proper conversion pixel to energy must be applied to the acquired signal, in order to get quantitative information out of the measurements. The conversion factor is evaluated checking the position on the detector of the elastic peak of carbon tape reference sample. The spatial resolution of the CCD cameras should not affect the overall energy resolution; therefore, many efforts have been put in order to push the contribution coming from the detectors far below the objective resolution [4]. First of all, the detector is inclined by 25° with respect to the optical axis so that two photons, following parallel trajectories from the sample, will hit the surface at a distance increased by a factor $1/\sin(25°)$. Moreover, a centroid algorithm has been developed to reconstruct the single photon impact position by calculating the centre of mass of the intensity distribution for each photon. As a result single photon counting (SPC) measurements are performed at ID32 and the contribution to the energy resolution of the spectrometer is about 7 meV, safely below the 30 meV value of high resolution setup.
The RIXS branch has been valuable in measuring features with never achieved before resolution, such as phonon dispersion in transition metals and crystal field splittings in rare earths compounds. More details about RIXS and ID32 in general can be found in [4, 5].
In the next chapter, an outline of the physics related to rare earth elements will be provided.

Chapter 3

Rare earth physics

The term rare earth is ambiguous, when referring to the 15 f-shell elements, since it includes Scandium (Sc) and Yttrium (Y) as well, whose Z is respectively 21 and 39. The name Lanthanides is more appropriate to identify the elements in the periodic table following Lanthanum (La), thus having the 4f shell partly filled. Nevertheless, in literature the terms rare earths and lanthanides are typically used as synonyms [1, 2, 17]; therefore, in this work as well, with the label rare earths, 4f elements are considered. Despite their name, rare earth elements are quite abundant on Earth and the origin of their rarity must be accounted to the fact that, due to their chemical similarity, they are seldom found as pure minerals but more often in mixed ores [2, 38].

In compounds, rare earth atoms are usually in the configuration $4f^n(5d6s)^3$, with the 3 electrons belonging to the 5d and 6s being shared with the surrounding atoms [2]. Therefore, the 4f electrons do not participate in chemical bonds and are somehow screened, preserving their atomic character. Accordingly, when modelling the Hamiltonian for a rare earth element, one can safely start from the isolated atomic term and add as a perturbation all collective solid-state effects.

Corrections to the atomic energetic levels provided by the perturbation theory are typically in the order of tens of meV, so that lanthanide compounds show to be model materials to be studied by high resolution techniques such as RIXS and XAS.

Moreover, being the 4f shell unfilled, the total angular momentum is different from zero, leading to a significant magnetic moment, which can be in the order of 10 μ_B per ion, due to the high value of orbital angular momentum of the f shell and the high number of electrons contributing to the spin momentum.

Owing to the atomic like character of 4f shell, i.e. the weak coupling to electrons of the surrounding atoms and to lattice vibrations, the rare earth elements are widely used in photonic applications [1]. As well as that, the high magnetic moment exhibited by lanthanide ions make them strong magnets for industrial applications.

On the other side, exotic properties have been found in rare earth ternary compounds arising from the interaction of the strong localized f shell with the delocalized electrons belonging to the conduction band [3]. Because of this plethora of properties, the scientific interest in lanthanide compounds has been increasing lately [3].

In this chapter, the themes quickly depicted here will be deepened, starting

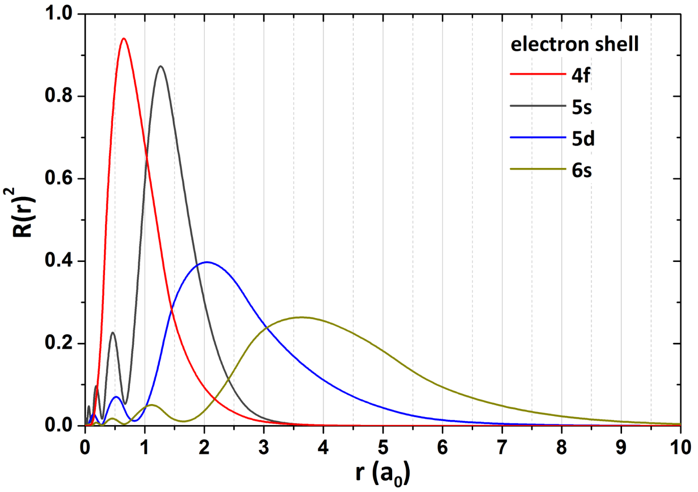

FIGURE 3.1: Square module of the radial part of electronic wavefunction for different shells, coming from Hartree-Fock calculations for Ce^{3+}. The position of the maximum is a rough estimation of the average position of an electron belonging to a specific shell. The coordinate r is expressed in numbers of Bohr radius a_0. Image taken from [13].

from the model Hamiltonian, passing towards crystal field perturbation theory, finally touching notions about the heavy fermion state and correlated RKKY and Kondo effect.

3.1 Free atom Hamiltonian

As already said, 4f electrons are not involved in chemical bonds. As evidence of the atomic character of the 4f shell, one can look at the square module of the radial part of the electronic wavefunction of electrons belonging to different shells in figure 3.1. The square modulus can be seen as the probability of finding one electron at r, being the origin of the axis the position of the nucleus. The sketched wavefunctions are calculated for the Ce^{3+} ion, with only one electron in 4f shell, thus being a rather simple case among rare earths. Nevertheless, the inner character of 4f shell with respect to 5s and 5d ones can be accounted for as a general property of rare earths [39]. Accordingly, 4f ions are typically found in a trivalent state in solid state compounds.

Then, it is clear that a proper Hamiltonian can be built starting from the isolated atomic term and adding terms modelling solid state effects as a perturbation [1, 2, 17, 18]. The Hamiltonian for an isolated atom containing N electrons in the outer subshell will be written as

$$\mathcal{H} = -\sum_{i=1}^{N}\left(\frac{\hbar^2}{2m}\nabla_i^2 + \frac{Z_{eff}e^2}{r_i}\right) + \sum_{i<j}^{N}\frac{e^2}{r_{ij}} + \sum_{i=1}^{N}\xi(r_i)\mathbf{l}_i\cdot\mathbf{s}_i, \tag{3.1}$$

where the first term stands for the potential of the electron in the field of the nucleus, being the sum of a kinetic part and an electrostatic one: Z_{eff} is put in place of Z atomic number to take into account the screening of nuclear charge by inner shells. The second term arises from electrostatic interactions between electrons belonging to the same shell and it depends on the distance r$_{ij}$ between couples. The third term describes the spin-orbit energetic contribution as a dipole-dipole interaction between the spin and angular momentum of electrons, with the constant ξ(r$_i$) being function of the distance from the nucleus.

It is impossible to find an exact solution for a quantum problem involving many electrons whose coordinates are mixed. Therefore, when dealing with N electrons, the central field approximation is exploited. In the framework, of this approximation each electron moves in a spherical average of the potentials of the other electrons [1, 2, 17, 18]. The difference with the real potential is treated as a perturbation to the spherically averaged case. One makes also the approximation that the spin-orbit term is much weaker than the electrostatic one, so that also the third term of 3.1 can be tackled in a perturbative approach. In formulas the Hamiltonian will be expressed as

$$\mathcal{H} = \underbrace{\sum_{i=1}^{N}\left(-\frac{\hbar^2}{2m}\nabla_i^2 - \frac{Z_{eff}e^2}{r_i}\right) + \langle\sum_{i<j}^{N}\frac{e^2}{r_{ij}}\rangle}_{\mathcal{H}_0} + \underbrace{\sum_{i<j}^{N}\frac{e^2}{r_{ij}} - \langle\sum_{i<j}^{N}\frac{e^2}{r_{ij}}\rangle}_{\mathcal{H}'_C} + \underbrace{\sum_{i=1}^{N}\xi(r_i)\mathbf{l}_i\cdot\mathbf{s}_i}_{\mathcal{H}'_{SO}}, \tag{3.2}$$

where the spherical part $\mathcal{H}_0$ has been separated from the perturbative Coulomb term, i.e. the non-spherical part of the electron-electron interaction $\mathcal{H}'_C$, and from the spin-orbit term $\mathcal{H}'_{SO}$. Since in $\mathcal{H}_0$ the coordinates of each electron are independent, the solution of the approximated Schrödinger equation $\mathcal{H}_0\Psi = E\Psi$ is a proper linear combination of single-electron wavefunctions for a hydrogen-like system.

The single-electron wavefunctions can be expressed as the product of a radial part and an angular function of the spherical harmonics, i.e. to the wavefunction is assigned a label made with the quantum numbers n, l and m_l. The principal quantum number n represents the electron shell, l stands for the orbital angular quantum number, i.e. it sets the subshell, and m_l is the magnetic number, representing the projection of l on a quantization axis. The spin part of the wavefunction is added by multiplying the spatial wavefunction by a function in the spin space. The ensemble of quantum numbers then includes also m_s: the projection of the spin momentum on a quantization axis.

A proper mechanical way to write the antisymmetric total wavefunction is calculating the Slater determinant [40], i.e.

$$\Psi_{TOT}(\tau_1, ..., \tau_N) = \frac{1}{\sqrt{N!}}\begin{vmatrix} \psi_1(\tau_1) & \psi_1(\tau_2) & \cdots & \psi_1(\tau_N) \\ \psi_2(\tau_1) & \psi_2(\tau_2) & \cdots & \psi_2(\tau_N) \\ \vdots & \vdots & \ddots & \vdots \\ \psi_N(\tau_1) & \psi_N(\tau_2) & \cdots & \psi_N(\tau_N) \end{vmatrix} \tag{3.3}$$

where the τ stand for the coordinates of each wavefunction, both spatial and in the spin representation, while the subscripts label a combination of the quantum numbers n, l, m_l and m_s.

The way electrons arrange in occupying the single-electron wavefunctions determines the energy of the system. Depending on the ratio between $\mathcal{H}'_c$ and $\mathcal{H}'_{SO}$ the orbital and spin momenta of the electrons combine following different schemes [1, 17]. When the electrostatic correction is more important than the spin-orbit term, the quantum number of orbital momenta l_i and the spin ones s_i of the electrons combine to give the total L and S of the many electron state, i.e. $\mathbf{L} = \sum_i \mathbf{l}_i$ and $\mathbf{S} = \sum_i \mathbf{s}_i$. This implies that, in the so-called Russel-Saunders, or LS coupling scheme, L and S are good quantum numbers for the electrostatic correction. Whereas, in the opposite case, the orbital momentum of each electron combines with the spin to give the quantum number j for the total angular momentum of each electron. Then, j_i combine to give the good quantum number J, considering the j-j coupling scheme. Since, spin-orbit correction shows a dependence of Z^4, the j-j coupling scheme is expected to be more appropriate when dealing with heavier elements.

In the case of lanthanides, the corrections due to the electrostatic term is always larger than the effects due to the spin-orbit [1, 17]. As a result, Russel-Saunders scheme holds and the first splitting of all the possible levels will occur for combinations with different L and S, i.e. different way for electrons to arrange in the subshell, with a degeneracy given for each term of (2L + 1)(2S + 1). The spin-orbit interaction will lead to a further splitting into terms with different J, with $\mathbf{J} = \mathbf{L} + \mathbf{S}$, leading to the so-called multiplets, with a degeneracy equal to 2J + 1 for each one. The overall scheme is then formally accounted for as an intermediate coupling one. Even if L and S are no more good quantum numbers, for rare earths, one can safely make the approximation that different LS terms do not mix, so that L and S can still characterize each multiplet. Therefore, following spectroscopic notation, each multiplet will be labeled with a term summarizing its S, L and J: the spectroscopic term will be written as ${}^{2S+1}X_J$ (X = S, P, D, F... for L = 0, 1, 2, 3...).

The struggle is then to find the best spherical approximation in order to treat the electrostatic and the spin-orbit interaction as perturbative corrections. The spherical part of the Hamiltonian 3.2 will provide for a 4f^n ion a number $\binom{14}{n} = \frac{14!}{(14-n)!n!}$ of degenerate combinations. Once the set of all the possible LS terms is found from the diagonalization of $\mathcal{H}_0$, the electrostatic corrections are evaluated by means of matrix elements of the kind

$$\langle {}^{2S+1}L | \mathcal{H}'_C | {}^{2S'+1}L' \rangle = \sum_k f_k F^k + \sum_k g_k G^k, \tag{3.4}$$

which will split the levels according to their LS term. The matrix elements in 3.4 have been expressed as sums of terms which are product of an angular and a radial part. The angular parts (f, g) can be written in terms of 3j symbols, already seen in chapter 1 and solved analytically, being integrals over spherical harmonics; the radial terms (F, G), called Slater integrals, must be computed [41] or left as fitting parameters [1]. The F integrals are related to interaction of electrons belonging to the same subshell and are accordingly defined as direct Slater integrals. The G terms, or indirect/exchange Slater integrals, take into account interactions occurring between electrons of different subshells. The expressions of the Slater integrals are

$$\begin{aligned} F^k(n_i l_i, n_j l_j) &= e^2 \int_0^\infty \int_0^\infty \frac{r_<^k}{r_>^{k+1}} R_{n_i l_i}^2(r_i) R_{n_j l_j}^2(r_j) r_i^2 r_j^2 \, dr_i dr_j \\ G^k(n_i l_i, n_j l_j) &= e^2 \int_0^\infty \int_0^\infty \frac{r_<^k}{r_>^{k+1}} R_{n_i l_i}(r_i) R_{n_i l_i}(r_j) R_{n_j l_j}(r_j) R_{n_j l_j}(r_i) r_i^2 r_j^2 \, dr_i dr_j, \end{aligned} \tag{3.5}$$

where the term $1/r_{ij}$ has been expressed in a multipole expansion of interactions for couples of electrons, $r_< = min(r_i, r_j)$, $r_> = max(r_i, r_j)$ and R_{nl} are the radial wavefunctions defined by the quantic numbers n and l [1].
Once again, as in the case of selection rules seen in chapter 1, the interaction between two electrons can be seen as a scattering event in which total angular momentum is conserved. The angular part will select, among the infinite terms of the multipole expansion, the Slater integrals which are different from zero. Since $k \leq l_a + l_b$ holds, for rare earths, the only terms which are different from zero are F^0, F^2, F^4 and F^6 among the direct. Dealing with M edge, one should also consider the interaction between two different shells, i.e. 3d and 4f: following the same argument related to the composition of spherical harmonics for two electrons in the same shell, one gets the direct terms F^0, F^2, F^4 and the indirect G^1, G^3 and G^5 different from zero [1, 2, 42].
Following the perturbative approach for the spin-orbit term as well, matrix elements similar to those of eq. 3.3 should be calculated as

$$\langle {}^{2S+1}L_J | \mathcal{H}'_{SO} | {}^{2S'+1}L'_{J'} \rangle = \zeta_{nl} A_{SO}(nl), \tag{3.6}$$

where now the degeneracy with respect to J is lifted [1, 2, 17]. Once again, the corrections are written as product of a radial and an angular part: the angular function sets constrains on the possible values of J, whereas the radial part ζ can be evaluated numerically or considered as a fitting parameter [41].
Since in the intermediate coupling, L, S and J can be considered all as good quantum numbers for the lowest energetic multiplet with a good approximation[2], to predict the way electrons arrange in the ground state of a rare earth ion, one can exploit the empirical Hund's rules [17]. The rules state that the multiplet at the lowest energy is characterized by a spectroscopic term with:

- S maximum.
  Since for Pauli's exclusion principle, electrons with parallel spin will occupy different orbitals, maximizing S they will stay at larger distance minimizing the electron-electron repulsion term.

- L maximum.
  Occupying orbitals with the same sign for L, electrons are orbiting in the same direction; this implies, that they can keep as far as possible from each other, minimizing once again the repulsion term.

- J maximum (J minimum) for a shell more than half full (less than half full).
  The third rule minimizes the spin-orbit interaction contribution. Since the constant in the spin-orbit term $\zeta \mathbf{L} \cdot \mathbf{S}$ switches sign from positive to negative for shells more than half full, the overall term is minimum if **L** and **S** lie parallel.

In table 3.1 a list of the rare earth trivalent ions is proposed, along with ground state valence and corresponding spectroscopic term expected following Hund's rules.

Z	Element	Valence	Spectroscopic Term
57	Lanthanum (La)	$4f^0$	$^1S_0$
58	Cerium (Ce)*	$4f^1$	$^2F_{5/2}$
59	Praseodymium (Pr)	$4f^2$	$^3H_4$
60	Neodymium (Nd)*	$4f^3$	$^4I_{9/2}$
61	Promethium (Pm)	$4f^4$	$^5I_4$
62	Samarium (Sm)	$4f^5$	$^6H_{5/2}$
63	Europium (Eu)	$4f^6$	$^7F_0$
64	Gadolinium (Gd)*	$4f^7$	$^8S_{7/2}$
65	Terbium (Tb)	$4f^8$	$^7F_6$
66	Dysprosium (Dy)	$4f^9$	$^6H_{15/2}$
67	Holmium (Ho)*	$4f^{10}$	$^5I_8$
68	Erbium (Er)	$4f^{11}$	$^4I_{15/2}$
69	Thulium (Tm)	$4f^{12}$	$^3H_6$
70	Ytterbium (Yb)	$4f^{13}$	$^2F_{7/2}$
71	Lutecium (Lu)	$4f^{14}$	$^1S_0$

TABLE 3.1: Lanthanides series. For each element the atomic number, the valence and the ground state spectroscopic term expected from Hund's rules are displayed. Compounds containing the elements marked have been examined in this work.

3.2 Crystal Electric Field theory

To further lift the remaining 2J + 1 degeneracy of the levels, terms which break the spherical symmetry must be added to the Hamiltonian 3.2. The presence of the crystalline matrix surrounding the rare earth ion sets axes to the structure, reducing the symmetry of the system. Therefore the multiplets term will be split depending on their orientation in the space, i.e. depending on the value of the projection of J on a quantization axis [1, 2, 10, 13, 17, 18].
In the framework of the crystal electric field (CEF) theory, a point charge electric field mimics the presence of the surrounding atoms [1, 2, 17, 18]. Therefore, the CEF Hamiltonian is written as

$$\mathcal{H}_{CEF} = -eV_{CEF}(\mathbf{r}), \tag{3.7}$$

where V_{CEF} is the fictitious crystal electric field potential.
The crystal field must resemble the symmetry of the environment surrounding the ion; this implies that only some electrostatic configurations can mimic the system properly. In other words, expressing the CEF Hamiltonian 3.7 as the product of a radial and a spherical part, like for the free ion interactions, i.e. in the Stevens' notation [43], one gets

$$V_{CEF}(r,\theta,\phi) = \sum_{k=0}^{\infty} \sum_{m=-k}^{k} A_k^m r^k C_k^m(\theta,\phi), \tag{3.8}$$

where only certain coefficients A_k^m are different from zero depending on the combination of the symmetry of the crystal with the one of the 4f shell, thus limiting expansion. In eq. 3.8, the angular dependence has been stressed writing (r,θ,ϕ) in place of $(\mathbf{r})$, where θ and ϕ are the polar and azimuthal angle. The $C_k^m = \sqrt{\frac{4\pi}{2k+1}} \cdot Y_k^m(\theta,\phi)$ are the renormalized spherical harmonics (Y_k^m) [44].
The same perturbative approach followed for the electrostatic and spin-orbit terms will lead to corrections to the energies of the ${}^{2S+1}L_J$ terms as

$$\begin{aligned}\langle {}^{2S+1}L_{J,M}|\mathcal{H}_{CEF}|{}^{2S'+1}L'_{J',M'}\rangle = &\sum_{k,m} A_k^m \langle r^k\rangle (-1)^{J-M} \times \\ &\begin{pmatrix} J & k & J' \\ -M & q & M' \end{pmatrix} D_J^k\end{aligned} \tag{3.9}$$

where the formalism of the 3j symbols has been exploited as already done in chapter 1 [1]. In the coefficient D_j^k is hidden a 3j symbol $\begin{pmatrix} l & k & l \\ 0 & 0 & 0 \end{pmatrix}$, which limits for the 4f shell (l=3) the possible coefficients to $A_{0,2,4,6}^m$, with the term A_0^0 typically neglected in calculations, being a monopole contribution thus leading to a rigid shift of all the energy levels. Due to the 3j symbol in eq. 3.9, the condition $|q| \leq k$ holds, i.e. the crystal field Hamiltonian must be invariant under all symmetric operations of the point group. Indeed, for the tetragonal group D_{4h}, which is the one of the the rare earth compounds examined in this work, the four-fold symmetry implies that $m = 0, 4$. In the D_J^k coefficient a 6j symbol is present as well, whose effect is to impose that no crystal field splitting is expected for multiplets characterized by an orbital angular number L=0, i.e. orbitals which exhibit a spherical symmetry in space are not expected to be affected by surrounding environment [1]. Therefore, for instance, for Gd^{3+} ion (see table 3.1), no CEF splitting is expected in the ground state multiplet [45].
Since the angular part is fully determined for each multiplet, it is clear that the only terms left to be determined are the Stevens' coefficients $A_k^m\langle r^k\rangle$ which include, as a parameter, the evaluation of the radial matrix elements $\langle R_{nl}|r^k|R_{nl}\rangle$.
The fact that the Hamiltonian must be hermitian sets the condition that $A_k^m = (-1)^m(A_k^{-m})^*$, further reducing the needed set of parameters to be calculated.
The levels are now split, depending on the magnetic number M and terms with

different M combine in such a way that the relation $-M+q+M'=0$ is fulfilled, i.e. $\Delta J_z = q$. Then, formally, both J and M are no more good quantum numbers. Nevertheless, typically corrections introduced by the crystal field Hamiltonian are much smaller than the splitting between different J terms [1, 18]. According to the same argument exploited as in the case of the spin-orbit interaction, one can then safely make the approximation that L, S and J are still good quantum numbers. Moreover, the 3j symbol in eq. 3.9 sets also the constrain that different multiplets characterized by the same J value will split in the same way. One may exploit this condition to study, in an indirect way, the splitting occurring to multiplets which may be not well resolved in experimental data [27].

It is evident that the full determination of the crystal field set is crucial in determining the ground state properties of rare earth compounds. Indeed, the crystal field due splittings determine the orientation of the orbitals of the rare earth ions; different orientations will lead to different ways the ion can interact with the crystalline environment. Therefore, the small crystal field corrections, determining the ground state shape, will lead to effects involving many sites of the crystal, such as hybridization of the ion with the ligand atoms and magnetic ordered states [12]; both effects will be more extensively discussed in section 3.4 of this chapter.

However, under a theoretical point of view, it is not trivial to accomplish the task of finding an unambiguous set of crystal field parameters and an empirical approach is by far the most effective way [1]. On the other side, the presence of the crystal matrix around the ion will affect also the parameters for the Coulomb electron-electron and spin-orbit corrections, typically reducing the radial integrals with respect to the isolated atom situation [1, 17]. Therefore, applying a fitting approach in order to reproduce experimental data, one will face the fact that a consistent number of parameters must be set. In the end, the high number of degrees of freedom will lead to huge time consuming calculations, if one would try to fit all of them at the same time, reducing to a problem without solutions in practice. Thus, one is left with a trial and error approach, with a fitting which should proceed from the most weighted parameters following the energy scale of the corrections, i.e. the free ion multiplet terms, to the less important crystal field parameters, one at a time. Still, this procedure can obviously lead to a false convergence since imposes biases; therefore, the combination of different experimental techniques is crucial in order to draw meaningful conclusions [4].

In this work, a combined analysis of polarized XAS data, RIXS spectra, fitting of anisotropic susceptibility and of low temperature magnetization data has been exploited to determine the set of crystal field parameters for $HoIr_2Si_2$.

The sensitivity of XAS data to the symmetry of the environment surrounding the ion has been already discussed in chapter 1 and has already proven to be effective [11–13, 46].

The measurement of the magnetic susceptibility is another indirect way to determine the crystal field corrections [47, 48]. Indeed, the magnetization occurring in rare earth compounds is due to the partially filled 4f shell. The magnetic moment is proportional to the magnetic quantic number, i.e. $\mu = -\mu_B g_J M$, where μ_B is the Bohr magneton and g_J the Landé factor. As already seen, the presence of the crystal lowers the symmetry of the ion, so that the electronic clouds will orient along some directions, which are defined as easy axes, rather than along hard axes [19]. The set of parameters determine the ground state and the hierarchy of the first excited states. When an external magnetic field is applied, a further energetic term $\mathbf{B}_{ext} \cdot \mu = g_J \mu_B B_{ext} M$ is added to the Hamiltonian which will let the system access the crystal field split excited states. Thus, depending on the direction along which the external magnetic field is applied, the system may exhibit different values for the magnetization, i.e. the system will occupy different orbitals, characterized by different values of the magnetic number M. Moreover, one can measure the susceptibility along different directions depending on the temperature. The thermal energy will let the system arrange in excited states following the Boltzmann statistics. All in all, a fitting of the crystal field parameters may be carried until the simulated curves resemble the experimental ones. This procedure is indirect and may be less straightforward to be applied when other magnetic effects are present with a physical origin different from the crystal field, e.g. exchange interaction and Kondo screening. In fact, in order to simulate the complete curves other parameters are needed, which increases the degree of uncertainty in the drawn considerations [4].

As already seen in chapter 1, RIXS spectra are in principle sensitive to *ff* excitations, thus directly providing information on the CEF splittings occurring in materials [4, 27, 49–51]. Moreover, RIXS is not limited to be sensitive to ground state properties like the aforementioned techniques, so that one is provided with a splitting scheme unambiguously involving also excited multiplets. This condition may be fruitfully exploited when the signal related to the ground state is not directly obtainable, e.g. when it is covered by the elastic peak tail or affected by other mechanisms different from the CEF, such as magnetic excitations or phonons. As well as that, RIXS has proven to be valuable in entangling contributions coming from mixed valence configurations occurring in some rare earth compounds [27].

3.3 Full multiplet calculations

All the approaches to determine CEF parameters seen in the previous section rely on a fitting mechanism. Therefore, experimental results have to be compared to simulations, which need to show a clear dependence on the parameters involved in the expression of the full Hamiltonian for a rare earth ion. The simulations exploited in this work have been performed with the aid of Quanty, a quantum many body Lua based script language [52].

Quanty is developed in the framework of a local Ansatz, i.e. solids are modeled by a small cluster, typically a single atom, whose Hamiltonian involves local Coulomb and multiplet interactions. In this scheme there is no chance to reproduce band effects and non-local dispersions, nevertheless the local approach allows to model most of the features related to rare earth compounds. One then can build the Hamiltonian describing the system in the same way as it has been developed in the previous; starting from the atomic terms, the crystal field contribution from the surrounding atoms is included as a perturbation.

Moreover, Quanty has proven to be a flexible tool. Not only it allows to find the eigenstates and perform calculations of a plethora of useful expectation values for the ion considered, which can be exploited to sketch Tanabe-Sugano diagrams or magnetic susceptibility graphs for instance, but also to simulate several core level spectroscopy experiments, including XAS and RIXS.

Once the basis set has been built in terms of number of fermionic modes, i.e. spin-orbitals in this work, typical quantum operators, expressed in the second quantization formalism, are combined to build the Hamiltonian or to calculate expectation values of physical quantities, e.g. energy, orbital, spin and total angular momentum. When dealing with the Hamiltonian 3.2 in Quanty the term $\mathcal{H}_0$ is not explicitly considered since its only effect is to produce a rigid shift of the energy levels, whereas the corrections $\mathcal{H}'_C$ and $\mathcal{H}'_{SO}$ are implemented; the electrostatic and spin-orbit term will lead to a relative variation of the various states with respect to the reference energy set to zero.

Below the code used to implement the electron-electron repulsion and the spin-orbit interaction, considering transition of a 3d electron into the 4f shell, i.e. the $M_{4,5}$ edge for a 4f^n ion.

```
-- Number of total fermionic modes considering the f and the d shell
NFermions = 24

--Number of electrons in the 3d shell
NElectrons_3d = 10

-- Number of electrons in the 4f shell
NElectrons_4f = n

--Labelling of the spin-orbitals dividing them between spin-up and
   spin-down sites
IndexDn_3d = {0, 2, 4, 6, 8}
IndexUp_3d = {1, 3, 5, 7, 9}
IndexDn_4f = {10, 12, 14, 16, 18, 20, 22}
IndexUp_4f = {11, 13, 15, 17, 19, 21, 23}

--Slater integrals for the 4f-shell, before promotion of the 3d
   electron in the 4f shell
F0_4f_4f = NewOperator('U', NFermions, IndexUp_4f, IndexDn_4f, {1,
   0, 0, 0})
F2_4f_4f = NewOperator('U', NFermions, IndexUp_4f, IndexDn_4f, {0,
   1, 0, 0})
F4_4f_4f = NewOperator('U', NFermions, IndexUp_4f, IndexDn_4f, {0,
   0, 1, 0})
F6_4f_4f = NewOperator('U', NFermions, IndexUp_4f, IndexDn_4f, {0,
   0, 0, 1})

--Slater integrals for the direct term (4f shell) and exchange term
   (4f and 3d electron interaction), after promotion of 3d electron
   in the 4f shell
F0_3d_4f = NewOperator('U', NFermions, IndexUp_3d, IndexDn_3d,
   IndexUp_4f, IndexDn_4f, {1, 0, 0}, {0, 0, 0});
F2_3d_4f = NewOperator('U', NFermions, IndexUp_3d, IndexDn_3d,
   IndexUp_4f, IndexDn_4f, {0, 1, 0}, {0, 0, 0});
```

```
F4_3d_4f = NewOperator('U', NFermions, IndexUp_3d, IndexDn_3d,
    IndexUp_4f, IndexDn_4f, {0, 0, 1}, {0, 0, 0});
G1_3d_4f = NewOperator('U', NFermions, IndexUp_3d, IndexDn_3d,
    IndexUp_4f, IndexDn_4f, {0, 0, 0}, {1, 0, 0});
G3_3d_4f = NewOperator('U', NFermions, IndexUp_3d, IndexDn_3d,
    IndexUp_4f, IndexDn_4f, {0, 0, 0}, {0, 1, 0});
G5_3d_4f = NewOperator('U', NFermions, IndexUp_3d, IndexDn_3d,
    IndexUp_4f, IndexDn_4f, {0, 0, 0}, {0, 0, 1});

--Spin-orbit term for the 4f electrons
ldots_4f = NewOperator('ldots', NFermions, IndexUp_4f, IndexDn_4f)

--Spin-orbit term for the 3d electrons
ldots_3d = NewOperator('ldots', NFermions, IndexUp_3d, IndexDn_3d)

--Initial Hamiltonian, before electron transition
H_i = H_i + Chop(
    F0_4f_4f_i * F0_4f_4f
  + F2_4f_4f_i * F2_4f_4f
  + F4_4f_4f_i * F4_4f_4f
  + F6_4f_4f_i * F6_4f_4f
  + zeta_4f_i * ldots_4f)

--Final Hamiltonian, after electron transition
H_f = H_f + Chop(
    F0_4f_4f_f * F0_4f_4f
  + F2_4f_4f_f * F2_4f_4f
  + F4_4f_4f_f * F4_4f_4f
  + F6_4f_4f_f * F6_4f_4f
  + F0_3d_4f_f * F0_3d_4f
  + F2_3d_4f_f * F2_3d_4f
  + F4_3d_4f_f * F4_3d_4f
  + G1_3d_4f_f * G1_3d_4f
  + G3_3d_4f_f * G3_3d_4f
  + G5_3d_4f_f * G5_3d_4f
  + zeta_4f_f * ldots_4f
    + zeta_3d_f * ldots_3d)
```

In the code, the values of the radial part of the Slater integrals and of the spin-orbit interaction are left as parameters, which can be fitted or imported from Hartree-Fock kind calculations[41]; for this work, the parameters have been obtained from Crispy [53], a graphical interface to let user generate Quanty script, without directly writing the lua code. A scaling parameter for each atomic term has been fitted comparing calculations with experiments, in order to take into account the screening effect seen in the previous section.
Considering the case of the ion Ho^{3+} whose valence is $4f^{10}$, one would expect 1001 states combining the 10 electron in the 14 spin-orbitals available. Below the first 76 states computed by Quanty are displayed, considering the electron-electron repulsion and the spin-orbit term splittings; the levels are divided into multiplets with relative spectroscopic terms; for each state the expectation values for the energy in eV, taking the ground state as the reference, $\mathbf{S^2}$, $\mathbf{L^2}$ and $\mathbf{J^2}$, in numbers of $\hbar^2$, are shown; finally, the last three columns are the expectation values, with the ground state as the reference again, for the corrections split in eV and the Boltzmann occupation probability calculated at 200 K. The

1001 degenerate states are split, with the first Coulomb split multiplets, i.e. ^{5}I and ^{5}F, at a distance higher than the one set by spin-orbit interaction, in accordance with what discussed in the previous; the final ground state degeneracy is 2J+1=17.

```
5
 I
  8
#   <E_i>   <S^2>  <L^2>   <J^2>   <H_ee>   <H_so>  dZ
1   0.000   5.736  42.951  72.000   0.000   0.000   1.000
2   0.000   5.736  42.951  72.000   0.000   0.000   1.000
3   0.000   5.736  42.951  72.000   0.000   0.000   1.000
4   0.000   5.736  42.951  72.000   0.000   0.000   1.000
5   0.000   5.736  42.951  72.000   0.000   0.000   1.000
6   0.000   5.736  42.951  72.000   0.000   0.000   1.000
7   0.000   5.736  42.951  72.000   0.000   0.000   1.000
8   0.000   5.736  42.951  72.000   0.000   0.000   1.000
9   0.000   5.736  42.951  72.000   0.000   0.000   1.000
10  0.000   5.736  42.951  72.000   0.000   0.000   1.000
11  0.000   5.736  42.951  72.000   0.000   0.000   1.000
12  0.000   5.736  42.951  72.000   0.000   0.000   1.000
13  0.000   5.736  42.951  72.000   0.000   0.000   1.000
14  0.000   5.736  42.951  72.000   0.000   0.000   1.000
15  0.000   5.736  42.951  72.000   0.000   0.000   1.000
16  0.000   5.736  42.951  72.000   0.000   0.000   1.000
17  0.000   5.736  42.951  72.000   0.000   0.000   1.000
5
 I
  7
#   <E_i>   <S^2>  <L^2>   <J^2>   <H_ee>   <H_so>  dZ
18  0.624   5.883  42.383  56.000  −0.082   0.706   0.000
19  0.624   5.883  42.383  56.000  −0.082   0.706   0.000
20  0.624   5.883  42.383  56.000  −0.082   0.706   0.000
21  0.624   5.883  42.383  56.000  −0.082   0.706   0.000
22  0.624   5.883  42.383  56.000  −0.082   0.706   0.000
23  0.624   5.883  42.383  56.000  −0.082   0.706   0.000
24  0.624   5.883  42.383  56.000  −0.082   0.706   0.000
25  0.624   5.883  42.383  56.000  −0.082   0.706   0.000
26  0.624   5.883  42.383  56.000  −0.082   0.706   0.000
27  0.624   5.883  42.383  56.000  −0.082   0.706   0.000
28  0.624   5.883  42.383  56.000  −0.082   0.706   0.000
29  0.624   5.883  42.383  56.000  −0.082   0.706   0.000
30  0.624   5.883  42.383  56.000  −0.082   0.706   0.000
31  0.624   5.883  42.383  56.000  −0.082   0.706   0.000
32  0.624   5.883  42.383  56.000  −0.082   0.706   0.000
5
 I
  6
#   <E_i>   <S^2>  <L^2>   <J^2>   <H_ee>   <H_so>  dZ
33  1.064   5.826  41.713  42.000  −0.019   1.082   0.000
34  1.064   5.826  41.713  42.000  −0.019   1.082   0.000
35  1.064   5.826  41.713  42.000  −0.019   1.082   0.000
36  1.064   5.826  41.713  42.000  −0.019   1.082   0.000
37  1.064   5.826  41.713  42.000  −0.019   1.082   0.000
38  1.064   5.826  41.713  42.000  −0.019   1.082   0.000
39  1.064   5.826  41.713  42.000  −0.019   1.082   0.000
40  1.064   5.826  41.713  42.000  −0.019   1.082   0.000
```

```
41   1.064    5.826   41.713   42.000   -0.019    1.082    0.000
42   1.064    5.826   41.713   42.000   -0.019    1.082    0.000
43   1.064    5.826   41.713   42.000   -0.019    1.082    0.000
44   1.064    5.826   41.713   42.000   -0.019    1.082    0.000
45   1.064    5.826   41.713   42.000   -0.019    1.082    0.000
5
 I
  5
#    <E_i>    <S^2>   <L^2>    <J^2>    <H_ee>    <H_so>    dZ
46   1.387    5.689   41.016   30.000    0.090    1.297    0.000
47   1.387    5.689   41.016   30.000    0.090    1.297    0.000
48   1.387    5.689   41.016   30.000    0.090    1.297    0.000
49   1.387    5.689   41.016   30.000    0.090    1.297    0.000
50   1.387    5.689   41.016   30.000    0.090    1.297    0.000
51   1.387    5.689   41.016   30.000    0.090    1.297    0.000
52   1.387    5.689   41.016   30.000    0.090    1.297    0.000
53   1.387    5.689   41.016   30.000    0.090    1.297    0.000
54   1.387    5.689   41.016   30.000    0.090    1.297    0.000
55   1.387    5.689   41.016   30.000    0.090    1.297    0.000
56   1.387    5.689   41.016   30.000    0.090    1.297    0.000
5
 I
  4
#    <E_i>    <S^2>   <L^2>    <J^2>    <H_ee>    <H_so>    dZ
57   1.642    5.619   40.805   20.000    0.136    1.506    0.000
58   1.642    5.619   40.805   20.000    0.136    1.506    0.000
59   1.642    5.619   40.805   20.000    0.136    1.506    0.000
60   1.642    5.619   40.805   20.000    0.136    1.506    0.000
61   1.642    5.619   40.805   20.000    0.136    1.506    0.000
62   1.642    5.619   40.805   20.000    0.136    1.506    0.000
63   1.642    5.619   40.805   20.000    0.136    1.506    0.000
64   1.642    5.619   40.805   20.000    0.136    1.506    0.000
65   1.642    5.619   40.805   20.000    0.136    1.506    0.000
5
 F
  5
#    <E_i>    <S^2>   <L^2>    <J^2>    <H_ee>    <H_so>    dZ
66   2.244    5.172   14.207   30.000    2.075    0.169    0.000
67   2.244    5.172   14.207   30.000    2.075    0.169    0.000
68   2.244    5.172   14.207   30.000    2.075    0.169    0.000
69   2.244    5.172   14.207   30.000    2.075    0.169    0.000
70   2.244    5.172   14.207   30.000    2.075    0.169    0.000
71   2.244    5.172   14.207   30.000    2.075    0.169    0.000
72   2.244    5.172   14.207   30.000    2.075    0.169    0.000
73   2.244    5.172   14.207   30.000    2.075    0.169    0.000
74   2.244    5.172   14.207   30.000    2.075    0.169    0.000
75   2.244    5.172   14.207   30.000    2.075    0.169    0.000
76   2.244    5.172   14.207   30.000    2.075    0.169    0.000
```

With the same approach, the CEF Hamiltonian in eqs. 3.7, 3.8 and 3.9 is added; in the code below the case of a 4f shell splitting occurring in a D_{4h} symmetry environment is taken into account.

```
--Definition of the Akm for the 4f shell
Akm = {
        {0, 0, A00_4f},
        {2, 0, A20_4f} ,
        {4, 0, A40_4f} ,
```

```
        {4,-4, A44_4f} ,
        {4, 4, A44_4f} ,
        {6, 0, A60_4f} ,
        {6,-4, A64_4f} ,
        {6, 4, A64_4f}
      }

--CEF Hamiltonian before and after transition in the approximation
    that the crystal field is not affected
H_i = H_i_noCEF + Chop(NewOperator('CF', NFermions, IndexUp_4f,
    IndexDn_4f, Akm))
H_f = H_f_noCEF + Chop(NewOperator('CF', NFermions, IndexUp_4f,
    IndexDn_4f, Akm))
```

The angular part of the coefficients A_k^m is fixed by the first two numbers in the string for each parameter, whereas the radial part is once again left as an open parameter; depending on the value of these parameters indeed the states will be further split due to the crystal field.

One then would like to exploit the possibility of building such in a flexible way the proper Hamiltonian in order to simulate experiments. Then, adding a Zeeman term to the Hamiltonian it is possible to simulate magnetization versus field curves as well as magnetic susceptibility as a function of temperature, also in magnetic ordered phases, e.g. ferromagnetic and antiferromagnetic samples. Details about this kind of simulations can be found in the SolidStatePhysics package of Quanty.

Furthermore, the XAS and RIXS cross-sections (eqs. 1.11 and 1.1) are implemented [42], exploiting the fact that the element matrix $|\langle f|T|g\rangle|^2$ can be rewritten as $\langle g|T|f\rangle \times \langle f|T|g\rangle$ and replacing the δ with a Green's function to take into account intrinsic core-hole lifetime broadening, as explained in section 1.2.1. Therefore, when the functions CreateSpectra(H_f, T, ψ_g) is called in the script, Quanty calculates the following Green's function

$$G_{XAS}(E) = \langle \psi_g | T^{\dagger} \frac{1}{E - H_f + i\Gamma/2} T | \psi_g \rangle, \tag{3.10}$$

where for the $M_{4,5}$ edge the Hamiltonian H_f is the one after transition of the 3d electron in the 4f shell, T is the dipole operator and ψ_g the initial spin-orbital wavefunction. In the same way, calling CreateResonantSpectra(H_f, H_i, T_1, T_2, ψ_g), one obtains

$$\begin{aligned} G_{RIXS}(E_1, E_2) = & \langle \psi_g | T_1^{\dagger} \frac{1}{E_1 - H_f - i\Gamma_1/2} T_2^{\dagger} \\ & \frac{1}{E_2 - H_i + i\Gamma_2/2} T_2 \frac{1}{E_1 - H_f + i\Gamma_1/2} T_1 | \psi_g \rangle, \end{aligned} \tag{3.11}$$

where H_i and H_f stand respectively for the Hamiltonian before and after the electronic transition; T_1 and T_2 are the dipole operators for the excitation and de-excitation processes; E_1 is the incident energy, whereas E_2 represents the energy loss with respect to the elastic peak reference; finally, Γ_1 and Γ_2 are the

broadenings in the in the final low-excited state and in the intermediate higly-out-of-equilibrium state: typically, Γ_2 is three orders of magnitude bigger than Γ_1.
In the next section, the phenomena occurring when the local 4f states interact with more delocalized electrons, i.e. the conduction electrons are briefly discussed. In view of the above, with a multiplet calculation approach there is no chance to reproduce such effects, whereas a procedure which mixes local multiplet and band calculations would be more fruitful [54], at the cost of a huge increase in time needed for simulations. Nevertheless, Quanty can be adapted to reproduce further effects, deriving from collective behaviours, e.g. ferromagnetism, by introducing other ad hoc parameters, i.e. exchange constants, and increasing the number of sites involved in calculations.

3.4 Exotic properties

Striking effects arise when the localized f electrons interact with the itinerant electrons belonging to the conduction band [2, 3, 55]. In particular, depending on the nature of interaction, two effects have been reported in literature. On the one hand, Kondo effect originates when the conduction electrons couple on-site with the 4f ones, screening the magnetic moment of the rare earth ion. On the other side, itinerant electrons can correlate the ion sites in magnetically ordered ground states, as a result of the Ruderman-Kittel-Kasuya-Yoshida (RKKY) interaction [2, 56].
In the light of the previous, the local model is not able to account for effects linked to interaction with strongly delocalized electrons belonging to the conduction band. Indeed, rare earth compounds are accounted for as strongly correlated electron systems, i.e. the electron-electron interaction is stronger than the one-electron band width so that the effective mean field theory is no more exploitable [4]. Nevertheless, performing multiplet calculations can shed light on the spatial anisotropy of the rare earth ion ground state, which in principle drives the on-site correlation with the ligand orbitals and the inter-site one with other ions [12]. In this section, a brief insight about these *exotic properties* of rare earth materials will be provided.
Some lanthanide-intermetallic compounds, typically Ce or Yb metallic systems, are reported in literature to show a minimum in the electrical resistivity as a function of the temperature, when approaching the 0 K temperature [57]. This is in contrast with general behaviour of metals whose resistivity monotonically decreases lowering temperature towards 0 K. Kondo deduced that a logarithmic term should be added in the resistivity to temperature dependence, to account for the unexpected increase [58]. Associated to this effect, measurements of specific heat coefficients have been reported to be 1000 times larger than the values obtained for typical metals, thus suggesting a huge increase - of the same factor - of the effective electron mass [59]: this class of materials is labeled as heavy-fermion compounds.
In the Anderson impurity model [54], the rare earth ion is treated as a single magnetic impurity and couples with the conduction electrons to form singlet states at each site. Due to the proximity in energy of the localized f states and

of the conduction band, a *c*-*f* hybridization occurs, leading to the formation of a new scattering channel and an associated increase of the resistivity. Moreover, mixed valence states, i.e. 4f^n valence occupation n being a non-integer number, have been reported to be a result of the partial delocalization of the f electrons [60]. The singlets act as heavily dressed quasi-particle and, due to the mixed local and itinerant properties, a raise of the effective mass, i.e. a decreasing of the momentum, of the electrons occurs.
The interaction leading to the formation of the coherent Kondo lattice state is an exchange-type interaction; therefore a suitable Hamiltonian to describe the physics of heavy-fermion materials should be [61]

$$\mathcal{H}_{KL} = \sum_{k\sigma} \epsilon_{\mathbf{k}} c^{\dagger}_{\mathbf{k}\sigma} c_{\mathbf{k}\sigma} + J_{ex} \sum_{i} \mathbf{s}_i \cdot \mathbf{S}_i, \tag{3.12}$$

where the second quantization formalism has been exploited, being $c^{\dagger}_{\mathbf{k}\sigma} c_{\mathbf{k}\sigma}$ the density of conduction electrons and $\epsilon_{\mathbf{k}}$ the relative dispersion energy. $\mathbf{S}_i$ and $\mathbf{s}_i$ are the spin operators of the localized and conduction electron respectively, at every lattice site i.
Indeed, the same exchange interaction, mediated by the polarized conduction electrons, is responsible for the formation of magnetically ordered states, where the local magnetic moments are not screened but align along preferred directions in the crystal. In RKKY model [2], the localized magnetic moment associated to the rare earth ion is approximated as a $\delta(\mathbf{r} - \mathbf{R})$ spatially localized perturbation centered in the ion position $\mathbf{R}$. Then, the exchange constant can be seen as the response of the material to this perturbation: an extremely localized in space perturbation has a wide spectrum in the reciprocal space. In the approximation of free-to-move particles, conduction electrons can provide a spectral response up to a wavevector $\mathbf{k} = \mathbf{k}_F$, in the 0 K limit, k$_F$ being the wavevector at the Fermi energy. The truncated square-shaped spectral filter provided by the polarized conduction band results in an oscillatory-like susceptibility function and of the exchange constant as well, as sketched in figure 3.2. As a result, ferromagnetic or antiferromagnetic ground states set, as a function of the distance between magnetic ions.
Depending on the value of the exchange constant J$_{ex}$, one of the two competing effects is likely to appear. To understand which one has to be expected, one may look at the dependence of the characteristic temperature for each phenomenon [61]:

$$\begin{aligned} T_K &\propto n(E_F)^{-1} \frac{1}{e^{\frac{1}{n(E_f)\cdot J_{ex}}}}, \\ T_{RKKY} &\propto n(E_F) \cdot J_{ex}^2, \end{aligned} \tag{3.13}$$

where n(E$_F$) stands for the electron density at Fermi energy. When n(E$_F$)·J$_{ex}$ approaches zero, T$_K$ goes to zero faster than T$_{RKKY}$ and the RKKY ordering effect dominates over the Kondo screening. Depending on a control parameter, e.g. the exchange constant, the external pressure and the chemical doping, heavy-fermion materials may be in a different phase [62]; in figure 3.3 the

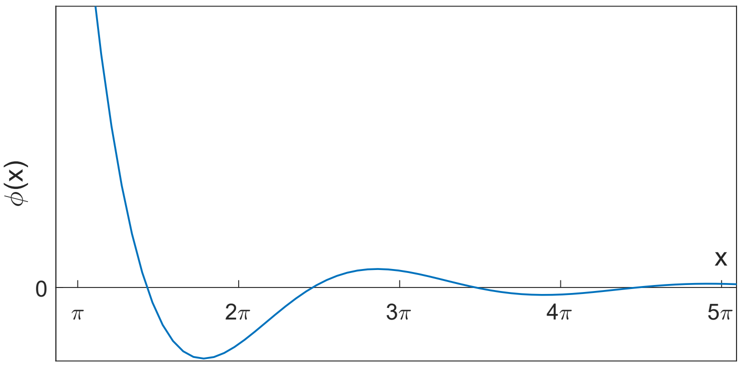

FIGURE 3.2: Response to a $\delta(\mathbf{r}-\mathbf{R})$ spatially localized perturbation. The susceptibility is proportional to the function $\phi(x) = \frac{sin(x) - x \cdot cos(x)}{x^4}$, $x = 2k_F(\mathbf{r}-\mathbf{R})$, which oscillates around zero and decays as cos(x)/x^3. The function diverges approaching zero, that is not physically true and a consequence of the δ approximation. Depending on the distance between ion sites a negative or positive sign is associated to the exchange constant, thus favouring ferromagnetic and antiferromagnetic ordering.

so-called Doniach phase diagram is provided. In the Kondo phase, a paramagnetic regime with strongly interacting electrons is set in the solid, described in the framework of the so-called Fermi liquid state model [63]. At the edge of the transition from the magnetically ordered to the disordered state, huge magnetic fluctuations arise in the material, leading to unconvential states of matter, such as magnetically driven superconductivity and non-Fermi liquid behaviour [64, 65]. Indeed, the material is crossing a quantum critical point (QCP), i.e. a phase transition is present at the absolute zero temperature [66]. In the next chapter, some rare earth ternary compounds will be quickly reviewed. A comparison of RIXS experimental and calculated spectra will fit scaling parameters, for Slater integrals and spin-orbit constant of ions in solids with respect to the case of isolated atoms.

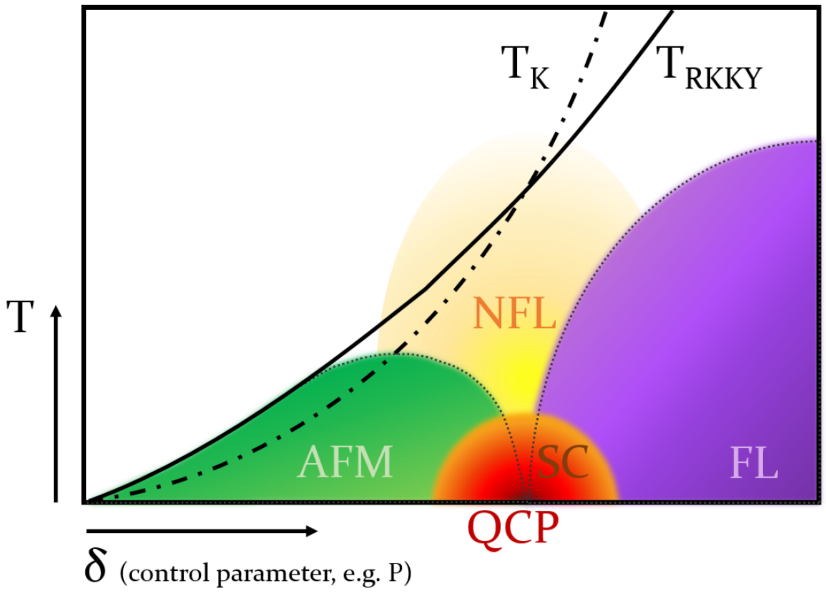

FIGURE 3.3: Doniach phase diagram. Depending on the ratio between T_{RKKY} and T_K, a magnetically ordered (typically AFM) or disordered ground state is set in the material. In the Kondo phase, the material exhibits paramagnetic properties with electrons strongly interacting among theme: a Fermi liquid model is suitable. At the crossing point, magnetic fluctuations arise as a result of a phase transition occurring in the material. Unconventional state of matters have been found close to the critical point, i.e. magnetically driven superconductivity and non-Fermi liquid behaviour. Image taken from [4].

Chapter 4

Atomic parameters fitting

In this chapter a quick review of the rare earth ternary compounds probed in this work is proposed.

The samples are 122 alloys, whose chemical composition is RETM$_2$X$_2$, being RE a rare earth ion, TM a transition metal and X an atom with the p shell partially filled, e.g. Si, P, Ge, As. For each sample the crystal structure obtained from [67] is displayed, along with the striking characteristics. Finally, experimental RIXS spectra are compared to simulations in order to obtain a fit of the rescaling parameter for Slater integrals and for spin-orbit ζ constant with respect to the isolated atom case. The fitting process relies on Matlab written codes for the minimization of quantities, e.g. the squared distance between simulated and experimental points and sum of distances between calculated and data peaks.

4.1 CeRh$_2$As$_2$

In figure 4.1 the unit cell of CeRh$_2$As$_2$ compound is proposed. The unit cell crystallizes in a CaBe$_2$Ge$_2$-type structure, whose crystallographic space group is P4/nmm, i.e. its spatial point group belongs to the tetragonal crystal system D$_{4h}$. The Ce^{3+} ions arrange in a Kondo state below 20 K $\div$ 30 K and show mixed valence behaviour [68].

4.1.1 RIXS fitting

The valence for the Ce^{3+} is 4f^1, therefore the 4f electron can arrange in the 14 f spin-orbitals. Since there is only one electron, no electron-electron correction is expected in the initial state, whereas, depending on the relative projection on a quantization axis of **S** and **L**, one would get a splitting of the levels in the two multiplets $^2F_{5/2}$ and $^2F_{7/2}$, with a six-fold and an eight-fold degeneracy respectively.

The experimental RIXS spectrum for CeRh$_2$As$_2$ is shown in figure 4.2. The estimated experimental resolution from the reference sample is $\sim$34 meV. Therefore, the wider broadening of the peaks can be accounted for as a CEF effect, with an overall upper bound of $\sim$50 meV for the ground state and of $\sim$70 meV for the spin-orbit split peak.

Simulations have been carried varying the scaling factor of the radial parameter ζ for the 4f spin-orbit interaction: figure 4.3 displays the simulated ^{2}F$_{7/2}$

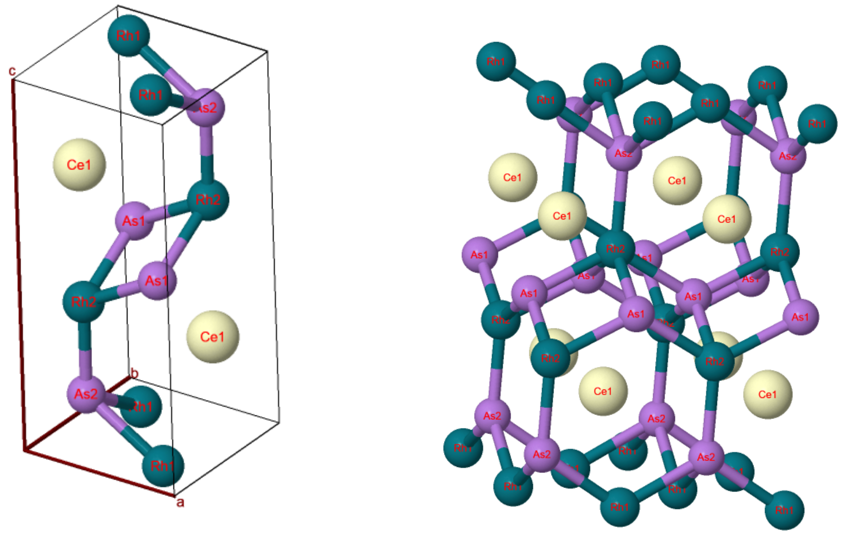

(A) (B)

FIGURE 4.1: (A) Unit cell of the $CaBe_2Ge_2$-type structure ternary compound $CeRh_2As_2$. For each element a label is provided: the 1 and 2 sites are symmetrically different. Indeed, the Ce atom locally lacks of inversion symmetry, whereas the unit cell is invariant under inversion with the centre of inversion being the point between the Ce sites. The axes of the unit cell are a = b = 4.283 Å, c = 9.850 Å [69]. (B) Coordination around the Ce atom. The nearest neighbours are 16 atoms, 8 Rh and 8 As. Under specular reflection with respect to a horizontal plane, the Rh1 atoms go into the As1, the same for the 2 sites: the local symmetry for the Ce atom is then further lowered to the C_{4v} spatial point group.

peak as a function of the scaling factor. Two minimization analysis have been carried out: a mean squared error fitting of the intensity of calculations in the data points and an evaluation of the distance between the centre of mass of experimental and calculated peak. For the first, the calculated spectra have been interpolated in the experimental points. A linear method of interpolation has been safely applied, for the number of simulated points is one order of magnitude higher than the experimental ones. For the latter, the tails have not been considered, since the peak shows to be asymmetric, i.e. the centre of mass have been calculated in the interval $-0.24\,\text{meV} \div -0.31\,\text{meV}$. The value for the scaling which minimizes both the quantities is 0.89, i.e. $\zeta = 0.89 \times 0.087$, leading to a spin-orbit splitting between the two multiplets of $\sim$271 meV.

A similar evaluation for the scaling factor of Slater integrals can not be performed as straightforwardly as the one for the spin-orbit parameter, since the only electron in the 4f shell is not subjected to electron-electron repulsion, both in the initial and final state of RIXS transition. This implies that the energy separation between the peaks is not a function of the scaling factor of the Coulomb repulsion. The only effect is to change the relative intensity of the inelastic peak with respect to the elastic one. The intensity of the elastic peak in a RIXS

spectrum depends on different boundary conditions of the experiment, e.g. diffuse scattering due to strain and defects in the crystal and crystalline surface quality [22]. In the simulations performed with Quanty there is no chance to reproduce such dependence.
Different spectroscopic techniques can be exploited to fit the scaling factor for Slater integrals: more details about this sample can be found somewhere else

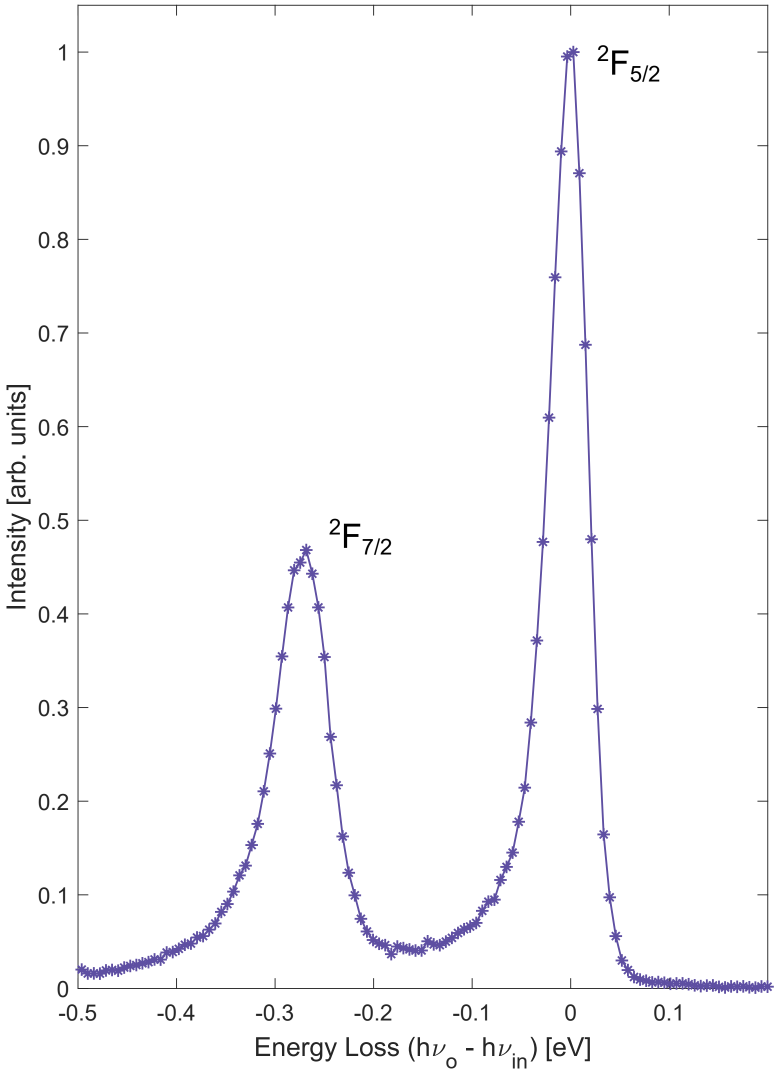

FIGURE 4.2: RIXS spectrum of the compound CeRh$_2$As$_2$. Data obtained at T = 20 K; $\theta = 75°$, $2\theta = 150°$, $\phi = 45°$ and $\chi = -90°$ in accordance to the definition of the geometry provided in chapter 2; linear polarization in the horizontal plane, as defined in chapter 2; incident energy equal to 881 eV, on the maximum of the XAS M$_5$ edge to enhance the resonance. The spectrum is the sum of 600 single photon counts (SPC) signals, acquired with an integration time of 20 seconds each. The signal has been normalized with respect to the photon current at the mirror before the sample stage. The two spin-orbit split multiplets have been labeled. The elastic peak (on the right) displays a FWHM of ∼50 meV, while the excited ^{2}F$_{5/2}$ peak is ∼70 meV broadened.

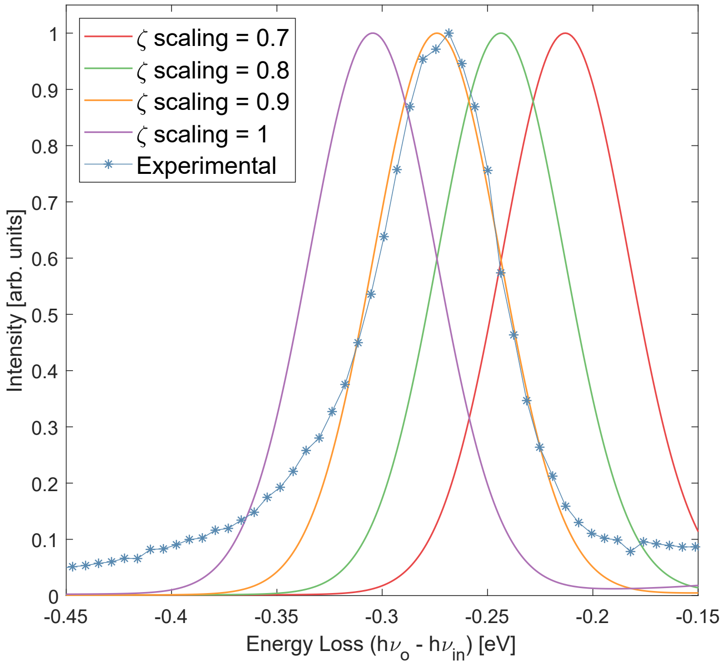

(A)

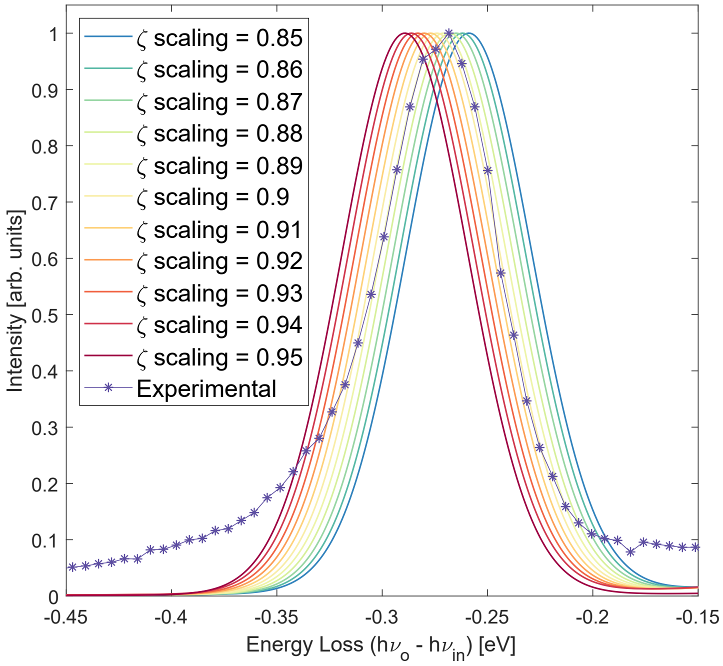

(B)

FIGURE 4.3: (A) Simulations of $^2F_{7/2}$ peak, as a function of the scaling factor for the atomic value of ζ parameter. (B) The scaling factor has been varied with a finer step, around the closer value from (A). A Gaussian broadening of 70 meV has been applied to the simulated spectra, to get a shape close to the experimental CEF broadened peak.

[68].

4.2 NdRh$_2$Si$_2$

The NdRh$_2$Si$_2$ compound crystallizes in the ThCr$_2$Si$_2$-type structure; its unit cell is equivalent to the one of GdIr$_2$Si$_2$, displayed in figure 4.6 below, with the Nd^{3+} trivalent ion in place of Gd^{3+} and Rh atoms substituting Ir. The axes are a = b = 4.059 Å and c = 10.003 Å [70]. NdRh$_2$Si$_2$ exhibits an antiferromagnetic ordering, below the Néel temperature T_N = 53 K, with moments aligned along c axis, as reported in literature [70]. At higher temperature, the compound displays paramagnetic behaviour, with a magnetic moment equal to 3.59 μ_B, very close to the theoretical expected one for Nd^{3+} free ion.

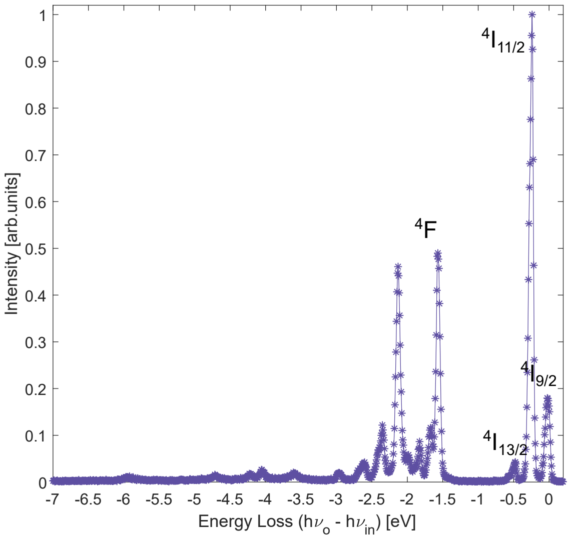

FIGURE 4.4: RIXS spectrum of the compound NdRh$_2$Si$_2$. Data obtained at T = 25 K; θ = 45°, 2θ = 90°, $\phi = -45°$ and $\chi = -90°$; linear polarization in the horizontal plane; incident energy equal to 980 eV, on the maximum of the XAS M$_5$ edge. The spectrum is the sum of 500 single photon counts (SPC) signals, acquired with an integration time of 60 seconds each. The signal has been normalized with respect to the photon current at the mirror before the sample stage. The first excited peaks belong to the ^{4}I term and are split by spin-orbit interaction. The ^{4}I peaks shows to be asymmetric to the side of higher energies loss (more negative value in figure). The feature at ~ -1.5 eV is labeled with its leading LS character.

4.2.1 RIXS fitting

The three electrons belonging to the 4f shell can arrange in 364 states, being the expected Hund's rules ground state the $^4I_{9/2}$ multiplet. Applying the arguments of chapter 3, the electron-electron repulsion and the spin orbit term will split the states in multiplets. The first excited states lie close to the ground state configuration, within ∼500 meV; indeed they belong to the same LS character and are spin-orbit split.

The experimental RIXS spectrum for $NdRh_2Si_2$ is shown in figure 4.4.
The experimental resolution has been estimated to be $\sim$ 40 meV; the first peaks exhibit an higher FWHM and asymmetric character, leading to the consideration that the 2J + 1 degeneracy is lifted. Indeed, the asymmetries in the ^4I peaks may be accounted for as CEF effects, splitting the different J_z states. The spin-orbit degeneracy for the ground state is 2J + 1 = 10; therefore, in principle, all the CEF terms A_k^m for electrons belonging to the 4f shell should be fitted to have a proper agreement with the experimental data. Here, in this work, the fitting will be proposed, as done previously, considering the electrostatic term and the spin-orbit corrections only, minimizing the distance between the centre of mass of calculated and experimental peaks.
The fitting of the scaling factor for F^K parameters is proposed in figure 4.5. The variation of the scaling parameter for the electrostatic terms does not affect the positions of the first excited peaks, in agreement to the fact that they are spin-orbit split. All the experimental features seem to be reproduced in simulations in terms of position. The relative intensity of the elastic peak is astonishingly different between calculations and experiments; once again this is due to the fact that Quanty is not able to reproduce properly the elastic scattering process. The agreement both in terms of relative intensities and distances of the peaks seem to get worse for energy losses higher in module than ~ -1.9 eV. Moreover, the experimental features exhibit a larger broadening with respect

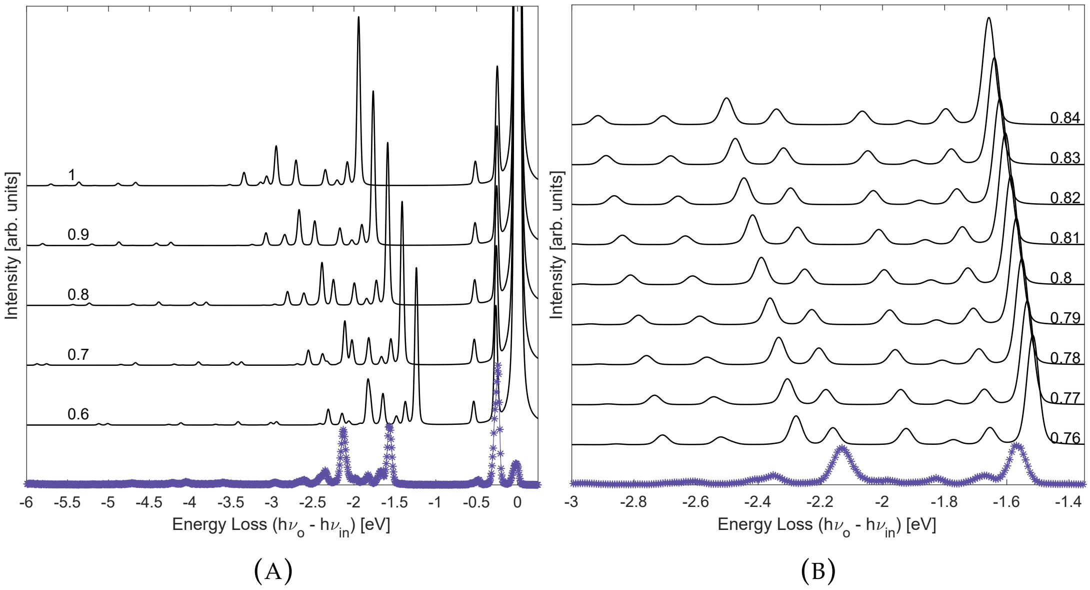

FIGURE 4.5: (A) Simulations of RIXS spectrum for the trivalent ion Nd^{3+}, as a function of the scaling factor for the atomic values of Slater integrals F^k: the value of the factor is shown in figure next to each plot. A Gaussian broadening of 40 meV has been applied to the simulated spectra to reproduce the experimental broadening. (B) Focus on the range $-3\,\text{eV} \div -1.4\,\text{eV}$ energy loss. The scaling factor has been varied with a finer step, around the closer value from figure on the left.

to simulations, which once again may be accounted for as a CEF splitting effect.

Considering also the fact that the features at energy losses higher in module than −1.5 eV are mixed LS terms, the fitting is not as straightforward as in the Ce case. Minimizing the distance between the maxima of the first three peaks in figure 4.5 (B) the best fitting parameter has been found to be 0.77; thus $F^2 = 0.77 \times 12.7211$, $F^4 = 0.77 \times 7.9821$ and $F^6 = 0.77 \times 5.7426$.

The scaling factor for ζ parameter in simulations shown in 4.5 is 1, i.e. the atomic value is considered. The first two spin-orbit peaks in figure 4.5 seem to be well aligned with simulated one; therefore $\zeta = 0.1187$.

4.3 $GdIr_2Si_2$

The $GdIr_2Si_2$ sample crystallizes in two structures, exhibiting polymorphism: a high temperature phase $CaBe_2Ge_2$-type structure with a crystallographic symmetry P4/nmm and a low temperature $ThCr_2Si_2$-type one, whose symmetry is labelled I4/mmm, both exhibiting a D_{4h} point group symmetry. The two phases are displayed in figure 4.6.

The experimental data considered in this work have been taken from a low temperature phase sample; no Kondo effect and local-moment magnetism have been reported in literature for $ThCr_2Si_2$-type structures [45, 71–73]. Moreover,

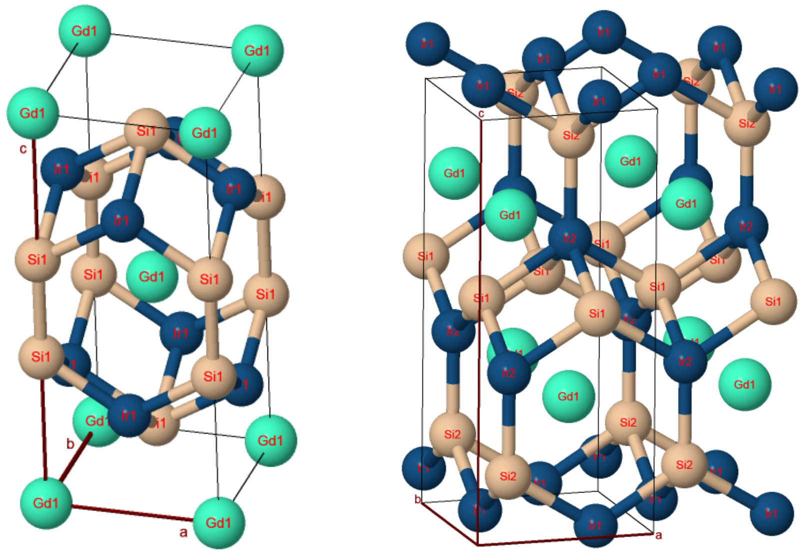

(A)

(B)

FIGURE 4.6: (A) Unit cell of the $ThCr_2Si_2$-type structure ternary compound $GdIr_2Si_2$. The axes of the unit cell are a = b = 4.06 Å, c = 9.930 Å. (B) Unit cell of the $CaBe_2Ge_2$-type structure ternary compound $GdIr_2Si_2$. The axes of the unit cell are a = b = 4.111 Å, c = 9.733 Å [71]. The coordination around the Gd atom is provided as well. The nearest neighbours are 16 atoms, 8 Ir and 8 Si. The same arguments of figure 4.1 apply here.

measurements have been performed in order to characterize the surface states of this class of materials [73]. Indeed, the aim is to find control parameters by which it is possible to tune the 2D-states exploitable in novel spin-based devices. More details can be found in [71].

4.3.1 RIXS fitting

The $4f^7$ valence for Gd^{3+} implies that the number of possible states is 3432. The ground state expected from Hund's rules exhibits a spherical symmetry, therefore no CEF splitting will occur [45]. Indeed, the FWHM of the elastic peak is equal to the experimental estimated resolution, i.e. ∼55 meV, in figure 4.7. The degeneracy of the elastic peak is related to the projection of the spin angular moment on a quantization axis, i.e. it is equal to $2S + 1 = 8$. The lifting of such a degeneracy can be achieved applying a magnetic field.

Simulations have been performed varying the scaling factor of the radial parameters both the electrostatic and spin-orbit corrections of the initial state, i.e. the terms F^2, F^4 and F^6 introduced in chapter 3 and ζ constant. Since the first are responsible for the splitting of different LS multiplets, the fitting has been performed considering the distance of the elastic peak from the inelastic peaks which show a different LS term, along with the relative distance among them.

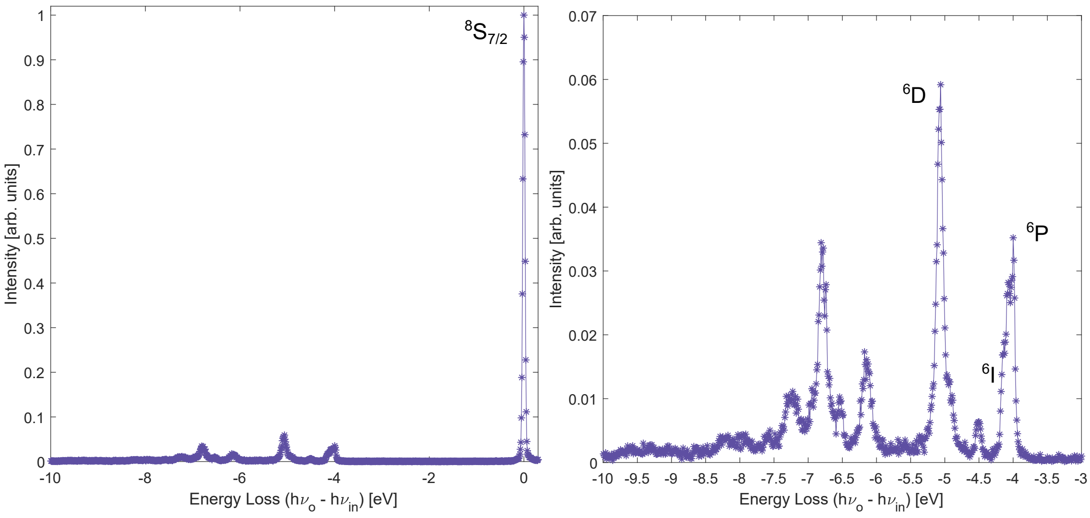

(A) (B)

FIGURE 4.7: (A) RIXS spectrum of $GdIr_2Si_2$ compound. Data obtained at T = 25 K; $\theta = 45°$, $2\theta = 60°$, $\phi = 45°$ and $\chi = -90°$; linear polarization in the horizontal plane; incident energy equal to 1184 eV, on the maximum of the XAS M_5 edge. The elastic peak exhibits a FWHM of ∼55 meV. The first excited states lie at ∼4 eV. The spectrum is the sum of 400 SPC signals, acquired with an integration time of 60 seconds each. The spectrum has been normalized with respect to the photon current. (B) Focus on the inelastic region of the spectrum. The LS character of the first peaks is provided. At higher energies multiplets get mixed and the LS notation is no more meaningful.

Next, a fitting of the spin-orbit parameter has been performed to get a better agreement with experimental data.
In figure 4.8, the calculations are proposed. Simulations seem to reproduce properly the experimental peaks up to $-6\,\text{eV}$ energy loss; at higher energies the local model is no more appropriate and the discrepancy may be accounted for as hybridization effects occurring between the local 4f levels and the surrounding ligand orbitals. The ^6I feature at $\sim -4.5\,\text{eV}$ in experiments is visible only as a little peak in calculations and its alignment is not good as for the other higher in energy features. By eye inspection and a minimization of the distance between the experimental and calculated data with respect to the ^{6}P ($\sim -4\,\text{eV}$) and ^{6}D ($\sim -5\,\text{eV}$) peaks, the best fitting value has been evaluated to be 0.83, i.e. $F^2 = 0.83 \times 14.502$, $F^4 = 0.83 \times 9.1012$ and $F^6 = 0.83 \times 6.5482$.
Following the same approach for the spin-orbit interaction, which is accounted to be a further correction with respect to the electrostatic repulsion term, calculations made varying the scaling for ζ parameter have been performed. The variation of ζ parameter towards the atomic value results in a broadening of the ^{6}P peak, due to a shifting of the highest in intensity peak $^6I_{7/2}$ multiplet to lower energies, and in a fluctuation of the intensity of the ^{6}D peak. Indeed, in this case a straightforward fitting of RIXS features is not applicable, since CEF effects will also affect the broadenings of the peaks and the relative intensities and positions as well. Nonetheless, one may guess the closest scaling factor

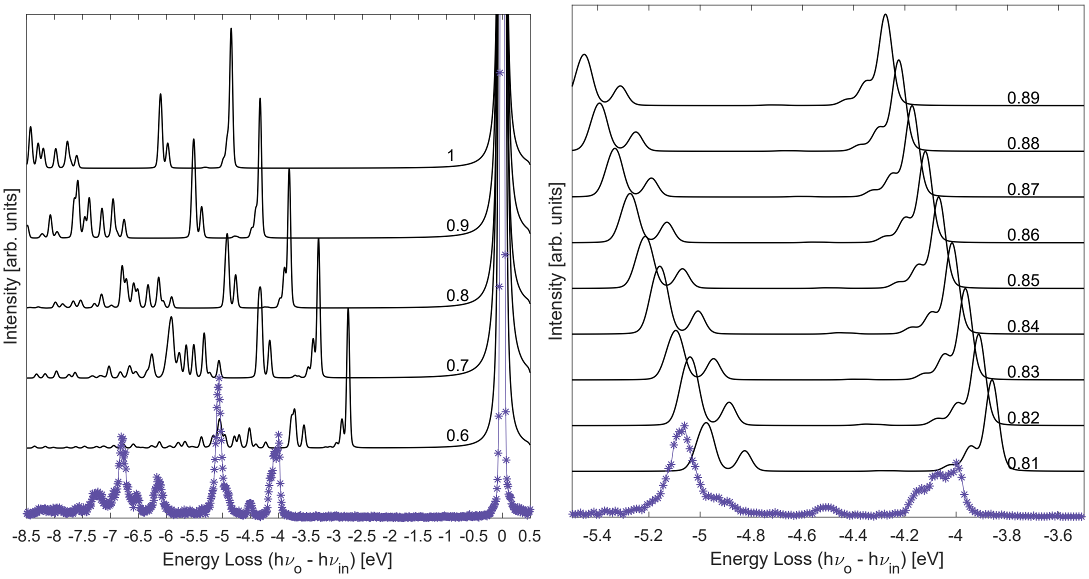

(A) (B)

FIGURE 4.8: (A) Simulations of RIXS spectrum for the trivalent ion Gd^{3+}, as a function of the scaling factor for the atomic values of Slater integrals F^k: the value of the factor is shown in figure next to each plot. A Gaussian broadening of 55 meV has been applied to the simulated spectra, to reproduce the experimental broadening. (B) Focus on the range $-5.5\,\text{eV} \div -3.5\,\text{eV}$ energy loss. The scaling factor has been varied with a finer step, around the closer value from figure on the left.

in the approximation that CEF will not mix multiplets with different J, i.e. by fitting the position of the relative maxima of each multiplet.
In figure 4.9 simulations of ζ scaling factor are proposed taking into account four possible values for the scaling factor of F^k parameters in order to avoid a false convergence result.

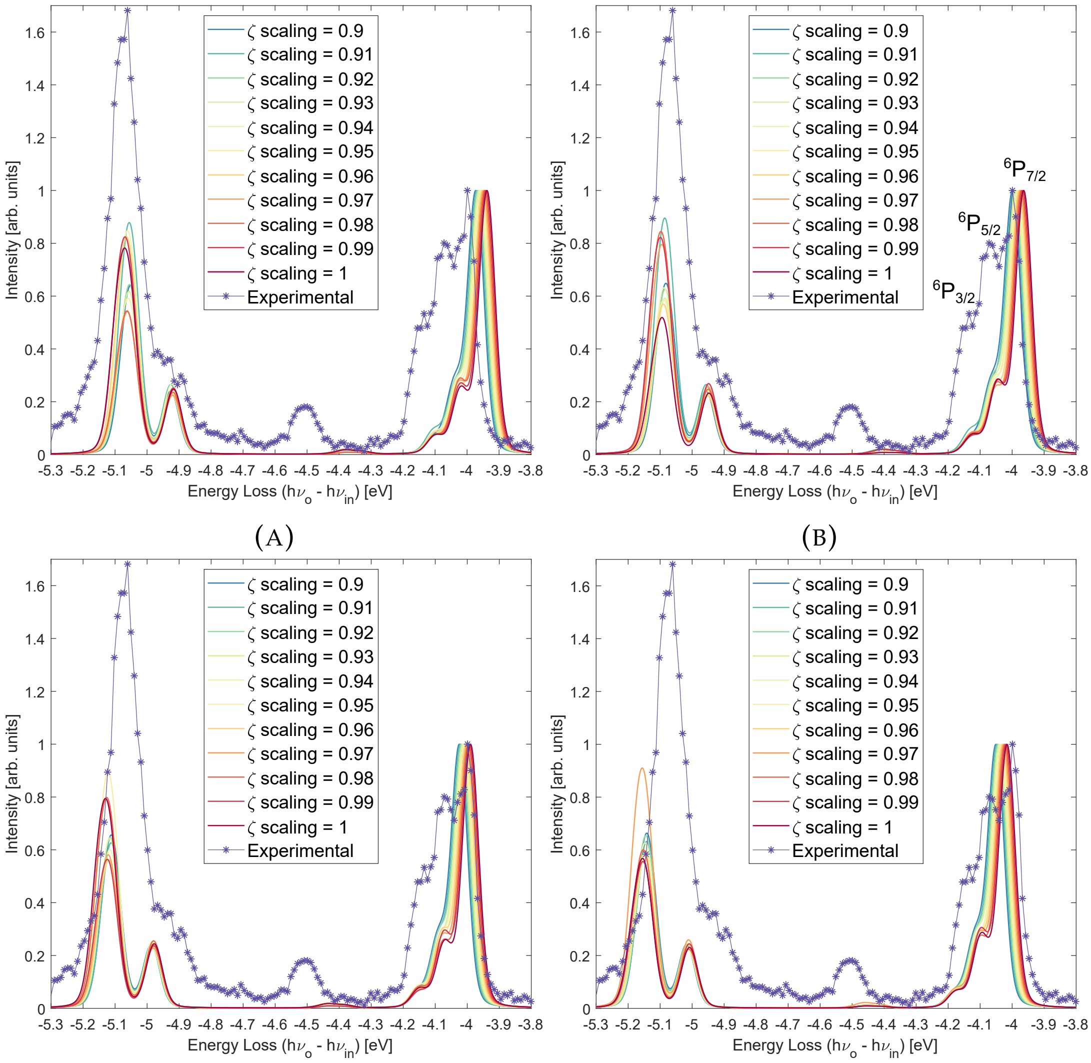

(A) (B)

(C) (D)

FIGURE 4.9: Simulations of the RIXS spectrum for the trivalent ion Gd^{3+}, as a function of the scaling factor for the spin-orbit radial parameter ζ, with three different scaling factors for F^k around the previously found minimum. (A) F^k Scaling = 0.825. (B) F^k Scaling = 0.83. (C) F^k Scaling = 0.835. (D) F^k Scaling = 0.84.

For the evaluation of the best fitting value a minimization of the sum of the distances between the maxima of the highest simulated and experimental peaks has been performed, leading to the value of 0.9, i.e. $\zeta = 0.9 \times 0.1973$, still being 0.83 the best parameter for the electrostatic interaction; blue plot in figure 4.9 B.

4.4 $HoIr_2Si_2$

$HoIr_2Si_2$ sample exhibits polymorphism as $GdIr_2Si_2$ compound; the two possible phases are indeed shown in figure 4.6, being the Ho^{3+} ion in place of the Gd atom. The single crystal low temperature phase is characterized by a = b =4.0476 Å and c =9.884 Å [71].
The possibility of crystallizing in two different phases has to be face when trying to grow a monocrystalline sample. Indeed, in the case of related Gd compound it was not possible to grow single crystals in the low temperature phase without traces of the high temperature phase, whereas the optimization of the growth process for the Ho compounds led to a significant enlargement of the single crystal sizes in the $ThCr_2Si_2$-type structure [71]. Nonetheless, the fact that the compound may crystallize in two different phases increases the uncertainty on a fitting of the CEF parameters, for the high temperature phase symmetry is further reduced with respect to the D_{4h} point group space, as already said when dealing with $CeRh_2As_2$. More details about $HoIr_2Si_2$ sample can be found in chapter 5 and in [71, 72].

4.4.1 RIXS fitting

The valence $4f^{10}$ electronic configuration for the Ho trivalent ion is the sum of 1001 possible states. The electronic and spin-orbit corrections lift the degeneracy, setting the $^5I_8$ multiplet to be the ground state, with a seventeen-fold degeneracy. The FWHM of the elastic peak is ∼105 meV very close to the estimated experimental resolution of ∼100 meV, therefore RIXS spectra with present resolution in figure 4.10 show no clear evidence of the splitting occurring for the ground state due to CEF. Nonetheless, there are proofs that the ground state degeneracy is lower than 17, as discussed in chapter 5.

Following the same approach as in the previous, a fitting of the atomic parameters is proposed. In particular, the electrostatic term is expected to affect mostly the position of the feature at ~ -2.7 eV with respect to the elastic peak, whereas the spin-orbit term is expected to act on the shifts of the first excited peaks with the same ^5I terms as the ground state. Accordingly, a minimization of the distances between the two features within simulated and experimental peaks has been performed to fit the scaling parameters.
Simulations for the scaling of Slater integrals are proposed in figure 4.11. Once again should be noted that the agreement gets worse at higher energies, where hybridization effects are likely to occur. Moreover, the discrepancy can also be accounted for as a consequence of the fact that the intermediate state in RIXS process is not properly reproduced. Nonetheless, features down to ~ -3.5 eV seem to be well reproduced both in terms of relative intensities and positions. The best fitting value considering the positions of the three features in the range $-2\,\text{eV} \div -4\,\text{eV}$ is estimated to be 0.88, i.e. $F^2 = 0.88 \times 15.7059$, $F^4 = 0.88 \times 9.8538$ and $F^6 = 0.88 \times 7.0859$.
With the found value for the scaling of F^k parameters, a fitting of the scaling of ζ is proposed in figure 4.12, considering the positions of the first two features closest to the elastic peak. Minimizing the sum of the distances between the

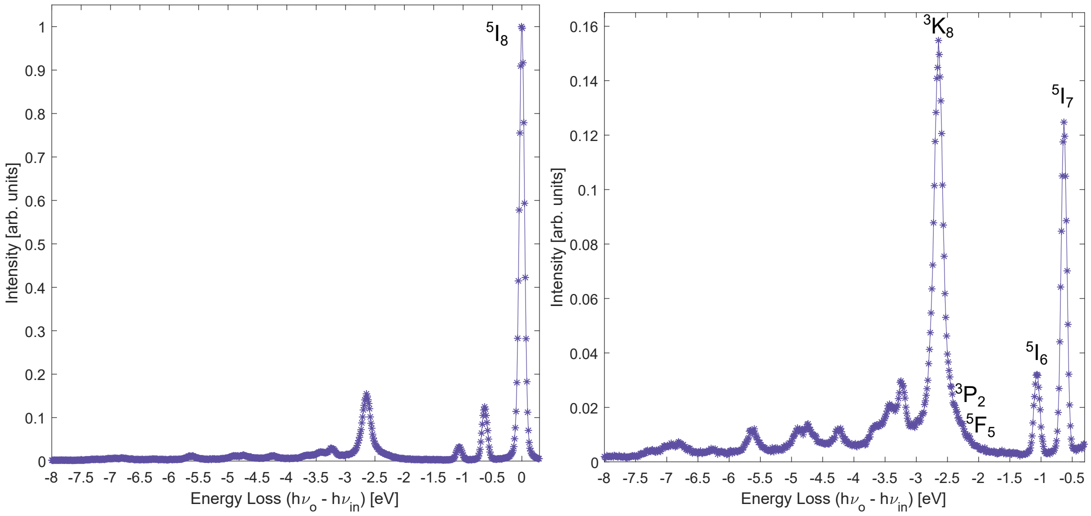

(A) (B)

FIGURE 4.10: (A) RIXS spectrum of $HoIr_2Si_2$ compound. Data obtained at T = 26 K; $\theta = 75°$, $2\theta = 150°$, $\phi = 45°$ and $\chi = -90°$; linear polarization in the horizontal plane; incident energy equal to 1349 eV, on the maximum of the XAS M_5 edge. The elastic peak exhibits a FWHM of ~105 meV. The first excited states are spin-orbit split and lie within ~600 meV with respect to the ground state. The spectrum is the sum of 325 SPC signals acquired with an integration time of 30 seconds each. The spectrum has been normalized with respect to the photon current. (B) Focus on the inelastic region of the spectrum. The spectroscopic terms for the first excited peaks is provided. The feature at ~ -2.7 meV is the sum of mixed $^{2S+1}L_J$ multiplets; indeed, the labels put express the closest atomic values for the expectation values of S^2, L^2 and J^2, yet calculated values show that the atomic model is no more so straightly applicable.

calculated and experimental maxima of the peaks, the best fitting value has been found to be 0.97, i.e. $\zeta = 0.97 \times 0.2734$.

The fitting values here found will be useful in chapter 5, as fixed parameters for simulations committed to the research of a crystal field set for $HoIr_2Si_2$.

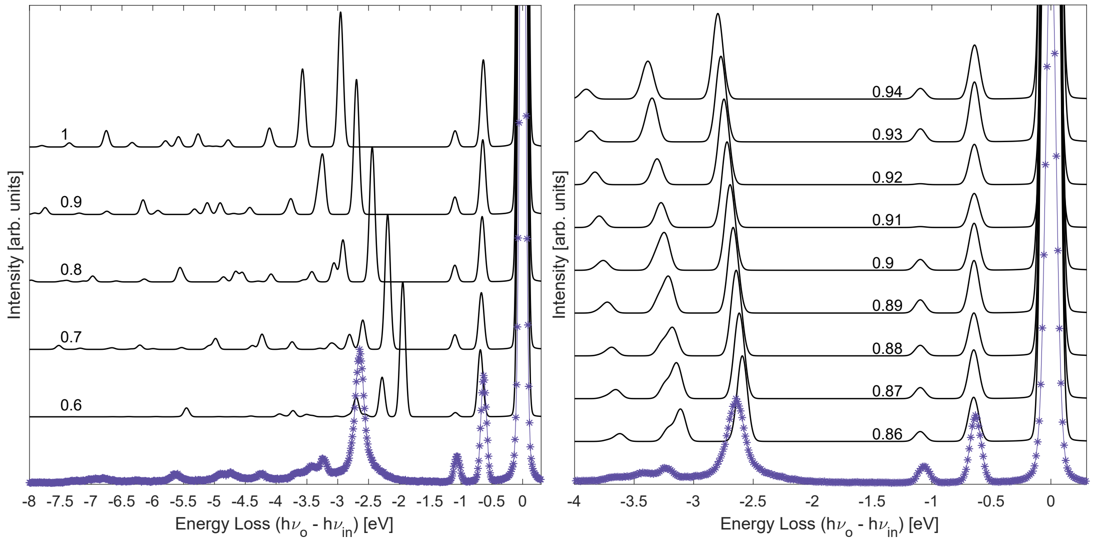

(A) (B)

FIGURE 4.11: (A) Simulations of RIXS spectrum for the trivalent Ho^{3+} ion, as a function of the scaling factor for the atomic values of Slater integrals F^k: the value of the factor is shown in figure next to each plot. A Gaussian broadening of 100 meV has been applied to the simulated spectra to reproduce the experimental broadening. (B) Focus on the region of energy loss down to -4 eV. The scaling factor has been varied with a finer step around the closest value from figure on the left.

4.5 Summary

RIXS has proven to be a spectroscopic technique deeply sensitive to multiplet interactions in rare earth compounds. Moreover, starting from a local model, as done by Quanty, most of the experimental features are successfully reproduced. The atomic character of rare earth ions is therefore experimentally confirmed.

On the other side, in order to get a further agreement with experimental data solid state effect should be included in calculations. In the framework of the local model exploited by Quanty, an improvement of the fitting is expected including CEF parameters.

As well as that, the accordance between relative intensities of simulated and experimental features is limited, the reader may see 4.9 for instance or consider the elastic peak in figure 4.5. Concerning the elastic peak, considerations about the fact that Quanty can not reproduce boundary conditions such as crystalline purity have already been expressed. Besides, phononic excitations contribute to the elastic peak as well [22]; in the performed simulations such contributions have not been taken into consideration. Whereas, the discrepancy in relative intensities occurring in the inelastic region may be ascribed to the incorrect evaluation of the intermediate state in simulations.

In the intermediate state a core hole is present whose strong potential affects the cross-section of RIXS scattering event, as seen in chapter 1. In principle a scaling of the atomic parameters should be performed also after the electronic transition from 3d to 4f, with a scaling factor which may be different from the one obtained for the initial and final state. XAS is more sensitive to the final state of electronic transition from d to f shell, i.e. the intermediate state in RIXS. Hence, in chapter 5, a fitting of experimental XAS spectra will be carried to characterize the scaling factor of atomic parameters in the intermediate state for Ho^{3+}.

A final remark should be done about the agreement of simulations with experimental data at increased in module energy loss. Comparisons between experiments and simulations suggest that increasing energy loss experimental features tend to stay closer to the elastic peak with respect to calculated ones. Again, the effect of the strong core hole potential in the intermediate state may have not been properly modeled in simulations.

In table 4.1, the fitting parameters are reported for each element. As a general trend we can infer that increasing the valence, i.e. the nuclear charge as well, the corrections to electrostatic interactions with respect to the isolated atom case decrease. This trend may be a consequence of the fact that increasing the Z_{eff} number in eq. 3.2 electrons are likely to stay closer to the nucleus thus being less affected by surrounding environment.

The same conclusions can not be drawn for the scaling factor acting on ζ. Regarding the scaling parameter for spin-orbit interaction, the atomic values seem already to be close to the experimentally fitted ones.

In figure 4.13 the trends for the atomic F^k and ζ parameters are displayed; an

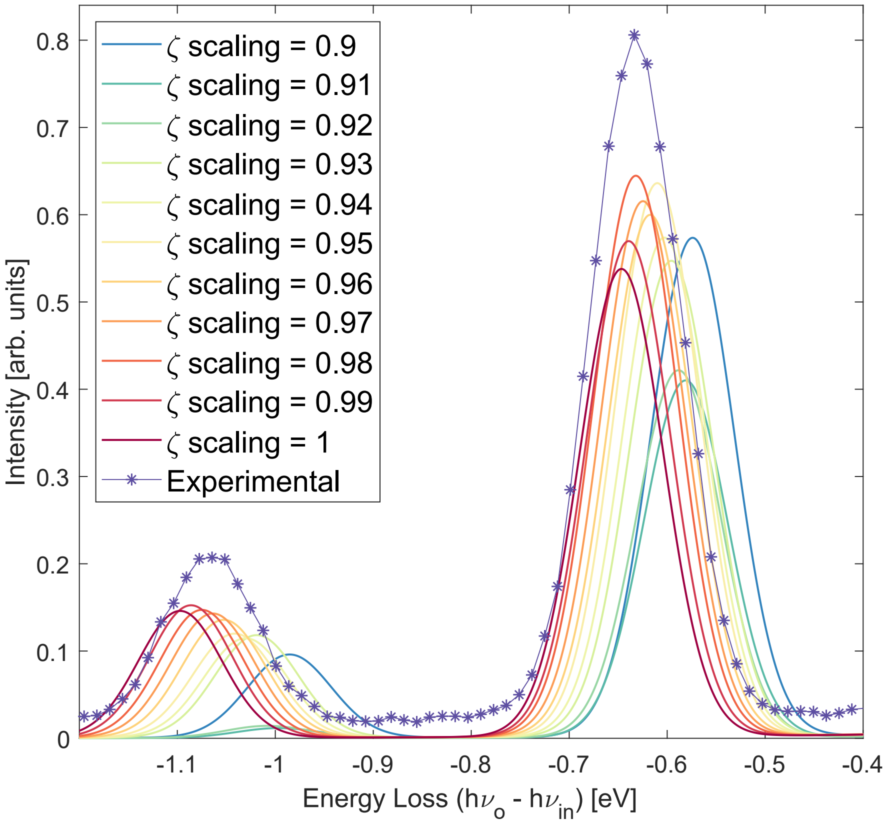

FIGURE 4.12: Simulations of the ^5I peaks, as a function of the scaling factor for the atomic ζ parameter.

Z	Element	Valence	F^k Scaling	ζ Scaling
58	Cerium (Ce)	$4f^1$	–	0.89
60	Neodymium (Nd)	$4f^3$	0.77	1
64	Gadolinium (Gd)	$4f^7$	0.83	0.99
67	Holmium (Ho)	$4f^{10}$	0.88	0.97

TABLE 4.1: Fitting of the scaling of radial parameters for electrostatic and spin-orbit interaction in some rare earth trivalent ions in compounds exhibiting a D_{4h} point group symmetry.

increase in module of the parameters seems to occur moving in the 4f shell toward heavier elements, in agreement with [1].

In the next chapter a further investigation of $HoIr_2Si_2$ compound is proposed.

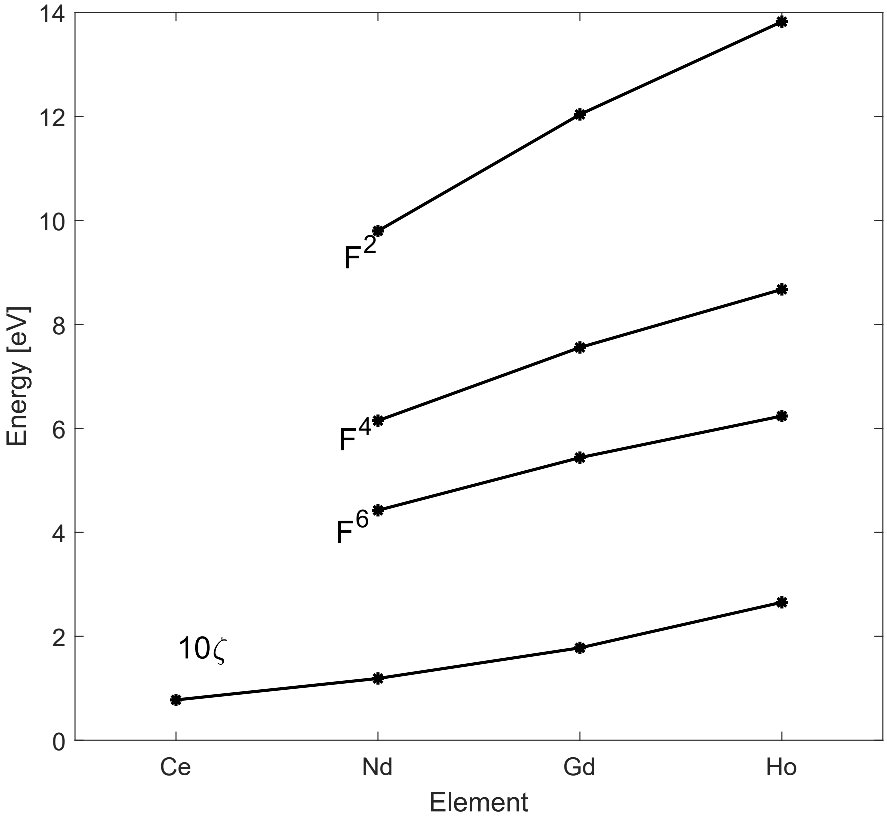

FIGURE 4.13: Trends of Slater and spin-orbit parameters. The values result from the multiplication of scaling factors, linked to crystal environment, and Hartree-Fock calculated values from Crispy [53] for isolated atoms.

Chapter 5

$HoIr_2Si_2$: analysis of CEF due magnetic properties

In this chapter a further analysis of $HoIr_2Si_2$ compound is provided.
The sample belongs to the ternary $RETM_2Si_2$ class of materials, RE being Sm, Gd or Ho, TM, being Rh or Ir [71, 74]. The sample can crystallize in two different phases; the low temperature $ThCr_2Si_2$-type structure exhibits local-moment magnetism, due to the 4f ions localized moments. The magnetic moments of the rare earth ion polarize conduction electrons, as a consequence magnetic ordered ground states due to RKKY interaction are reported in literature for this class of materials [71, 72, 74–79]. Moreover, materials like $HoIr_2Si_2$ are suspected to possess electronic surface states, which can be manipulated by external control parameters [73, 80]. As well as that, a strong anisotropy in bulk magnetizations have been reported in literature [71, 72, 81, 82]. The possibility to access different magnetic states both in bidimensional and bulky systems can be of relevant interest for spintronic applications. On the other side, no Kondo effect is ascribed to these materials.
Starting from the properties of $HoIr_2Si_2$ reported in literature, XMCD data will be provided as a validation of the magnetization data; a comparison between the reported magnetization and the results coming from the application of sum rules will be proposed. Then, measured magnetic susceptibility curves, along with specific heat capacity data, will be discussed in the framework of CEF model. The analysis of XAS spectra will be the successive step; exploiting the sensitivity of this spectroscopic technique to different experimental geometries, a CEF set of parameters will be fitted with the aid of Quanty. Finally, the consistency of the found set will be verified trying to reproduce in simulations experimentally measured magnetic data, i.e. fitting magnetization and susceptibility curves.

5.1 Properties of $HoIr_2Si_2$

As already said, $HoIr_2Si_2$ ternary compound is characterized by a tetragonal structure; powder x-ray diffraction data confirmed for the analyzed sample the I4/mmm tetragonal structure reported in figure 5.1. The orientation of the sample has been determined by Laue pattern; from the analysis of 15 samples the c axis was determined to be perpendicular to the largest surface in figure

5.1. The Bragg's spots in Laue measurements are not as sharp as in the equivalent $RERh_2Si_2$ structures, suggesting a poorer crystalline purity and hinting to the coexistence of the high temperature phase $CaBe_2Ge_2$-type structure.

Measurements of magnetic susceptibility along three different axes as a function of the temperature have been also made. Magnetic susceptibility curves show to be anisotropic in figure 5.2. The one measured along c has a maximum, hinting to the occurrence of a transition to an antiferromagnetic state at T_N = 22 K, being T_N the Néel temperature. In the ab plane, the susceptibility seems to be constant up to T_N and goes to zero following a Curie dependence. The anisotropy in the magnetic susceptibility suggests for an alignment of magnetic moments along (001) axis.

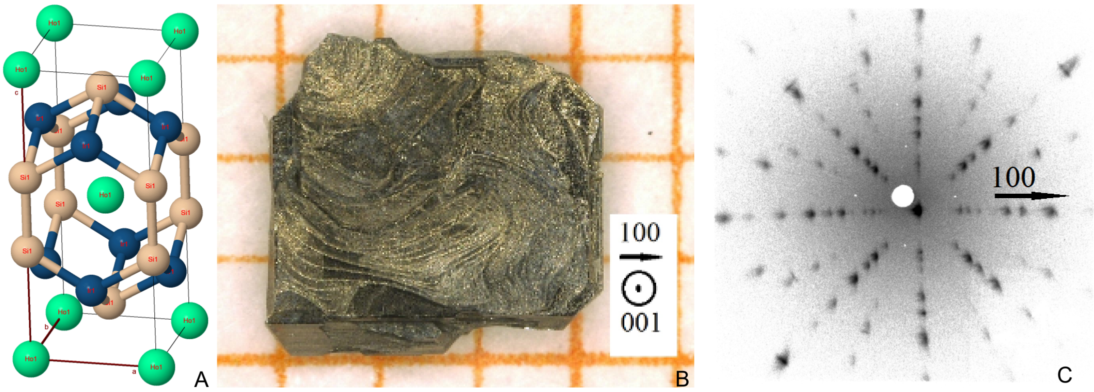

FIGURE 5.1: (A) $ThCr_2Si_2$-type structure for $HoIr_2Si_2$ compound. The point group symmetry for Ho^{3+} ion enveloped in the unit cell is D_{4h}. a, b and c axes are labeled. (B) Picture of $HoIr_2Si_2$ single crystal; (100) axis is equivalently a or b axis, while (001) is the c axis in (A). The orientation of the sample was determined with Laue diffraction measurements displayed in (C). (C) Laue pattern. The tetragonal symmetry is confirmed. The distance between the spots yielded a = b =4.0600(12) Å and c = 9.930(4) Å [71].

Indeed, considering a couple of magnetic moments antiparallel aligned, if a magnetic field is applied at 0 K along the axis of the moments, no net magnetization is expected. Increasing temperature, the thermal fluctuations will make the two spins tilt, so that they can get more oriented along the symmetry axis set by the field; therefore, the total magnetization of the system is proportional to the temperature. For temperatures higher than T_N, the thermal energy will act as a disordering factor, since k_BT term is higher than Zeeman splitting. As a result, the probability of occupation of states with an antiparallel projection of the magnetic moment along the magnetic field axis becomes significant, leading to a reduced magnetization increasing temperature. Instead, considering again the system made by the two spins, if the magnetic field is applied in the perpendicular direction with respect to their common axis, a net magnetization is expected also for 0 K, since moments will symmetrically align parallel to the field. If temperature is increased, applying the same argument as before, a decrease in magnetization is expected [57].

In figure 5.2, the measured inverse susceptibility of $HoIr_2Si_2$ is reported as well. It is useful now to express the magnetic susceptibility for a paramagnetic substance, as a function of the temperature, i.e.

$$\chi_{mol}(T) = \frac{\mu_0 N_A J(J+1)(g_J \mu_B)^2}{3k_B T} = \frac{\mu_0 N_A n_{eff}^2 \mu_B^2}{3k_B T} \tag{5.1}$$

where N_A is the Avogadro number, J(J+1) is the expectation value for $\mathbf{J}^2$ and g_J, the Landé factor. The inverse susceptibility is a linear function of temperature, whose slope is proportional to n_{eff}^2, which is the number of effective Bohr magnetons. Therefore, from the characteristic of the function χ_{mol} of T, the magnetic moment per Ho^{3+} ion can be evaluated: $\mu_{eff}^{100} = 10.53(10)\ \mu_B$, $\mu_{eff}^{110} = 10.52(10)\ \mu_B$ and $\mu_{eff}^{001} = 10.64(10)\ \mu_B$, very close to the theoretically expected magnetic moment 10.6 μ_B putting $J = 8$ and $g_J = 5/4$ in eq. 5.1.
A measurement of the magnetization in numbers of μ_B per ion at 2 K as a function of the external applied magnetic field is proposed in figure 5.3 as well. The anisotropy between c axis and ab plane is still evident. Moreover, in the (001) direction, the magnetization follows a step-like function, with two critical field at B_1 ~1.4 T and B_2 ~4.1 T, hinting to the occurrence of two metamagnetic transitions [83]; the function seems to reach a saturation value of 8 μ_B for magnetic field higher than 5 T. In the ab plane, magnetization increases almost linearly, saturating for fields higher than ~6 T; a slight anisotropy between the (100) and (110) axis is visible in the saturation region, with the magnetization measured along the first direction reaching a saturation value of ~5 μ_B and the latter ~4 μ_B. In figure 5.3 a phase diagram in the B-T plane for the (001)

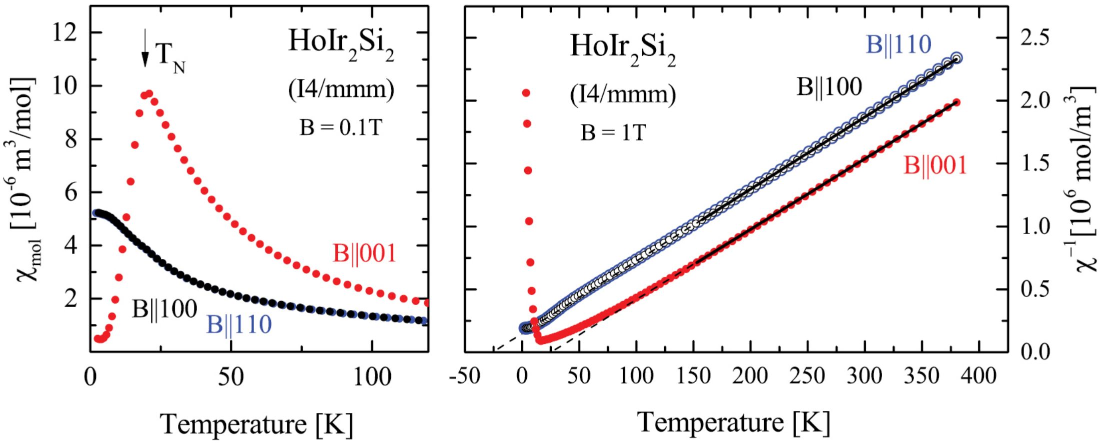

FIGURE 5.2: On the left: plot of the measured molar magnetic susceptibility for $HoIr_2Si_2$. A strong anisotropy between measurements taken along c and in the ab plane is present. The magnetic susceptibility shows a maximum for T_N, hinting to an antiferromagnetic ordering of the sample along the (001) axis. On the right: plot of the inverse molar susceptibility in the paramagnetic regime. The anisotropy is still evident, for the inverse susceptibility measured along c is always smaller than the planar one. From the slope of the curves it is possible to deduce the magnetic moment per atom. Image taken from [72].

direction is also shown. The critical fields of the magnetization curve along (001) are indeed the boundaries of two antiferromagnetic phases, defined as AFI and AFII. For fields higher than B_2, the sample exhibits a paramagnetic behaviour. Moving along isothermal lines, the magnetic susceptibility of figure 5.2 is reproduced, with a transition from an antiferromagnetic ground state to a paramagnetic excited one.

In chapter 1, XMCD has been briefly discussed. In the following, the formalism of sum rules will be exploited to confirm, at least in a qualitative way, the peculiar magnetization step-like function.

In figure 5.4, XMCD data for $M_{4,5}$ edges of HoIr$_2$Si$_2$ are shown; data have been collected with an applied magnetic field along c axis of 1 T, 3 T and 8 T and at a 9.4 K, so that one can safely say that only the lowest states are occupied. Using a conventional definition, right circular polarized light (R) in figure 5.4 is defined as radiation whose helicity is antiparallel to the applied external magnetic field, while being L parallel [84]. According to the arguments discussed in chapter 1, the integral of the dichroism signal is proportional to the expectation value of the magnetic moment along z; XMCD spectra shown in figure 5.4 are taken in the three steps of the magnetization for HoIr$_2$Si$_2$ (the reader may see figure 5.3). The spectra resemble the step-like trending for the magnetization. In order to confirm the data reported in literature, sum rules have been applied to a series of XMCD data taken from 0 T to 9 T with a step of 0.5 T between scans, again at a temperature of 9.4 K. The Pymca tool 5.0.3 version has been exploited to apply sum rules [85]. Once XMCD data are imported in the tool, the code performs a subtraction of the non-magnetic contribution to

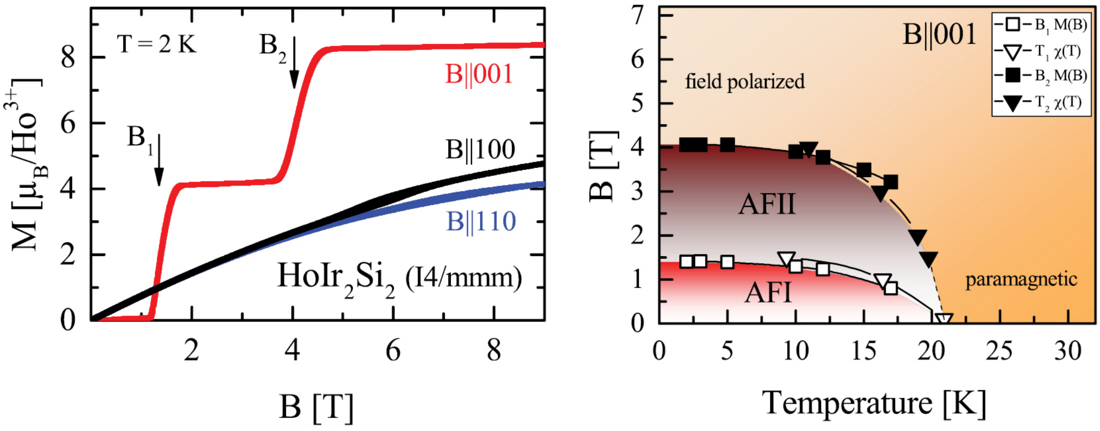

FIGURE 5.3: On the left: plot of the measured magnetization along three different crystallographic axes at T = 2 K The anisotropy is evident; in the (001) direction the magnetization follows a step-like function hinting to the occurrence of magnetic transitions of phase at B_1 and B_2. Whereas in the ab plane a paramagnetic-type behaviour is evident. On the right: phase diagram of Hoir$_2$Si$_2$ compound in the B-T plane for the (001) direction. The phase region boundaries (closed and open squares) are B_1 and B_2 functions of temperature. The triangles stand for the maxima of $\chi(T)$. Image taken from [72].

spectra, i.e. the steps occurring at the edges due to the excitation to the continuum, with the proper branching ratio set by the user: for the M$_{4,5}$ edges the ratio is $\frac{2j_{-}+1}{2j_{+}+1} = 2/3$. Thanks to an user-friendly graphical interface, it is possible to set the energy position of the edges, where steps must be subtracted, and the boundaries for the integration of the XMCD and of the estimated isotropic XAS signals.
The obtained results from application of sum rules, i.e. the expectation values for S$_z$, L$_z$ and number of Bohr magnetons as a function of the external applied magnetic field, are plotted in figure 5.5. XMCD data confirm the step-like behaviour for the magnetization reported in literature, the steps occurring near ∼1.5 T and ∼4 T in good agreement with data from [72]. Considering the expectation value for the orbital angular momentum projection, the experimental data saturate to a value equal to 6 $\hbar$ for B > 5 T. Indeed, this saturation value is in good agreement with the maximum projection available for the multiplet term ^{5}I$_8$, once again confirming the atomic character of Ho^{3+} and the validity

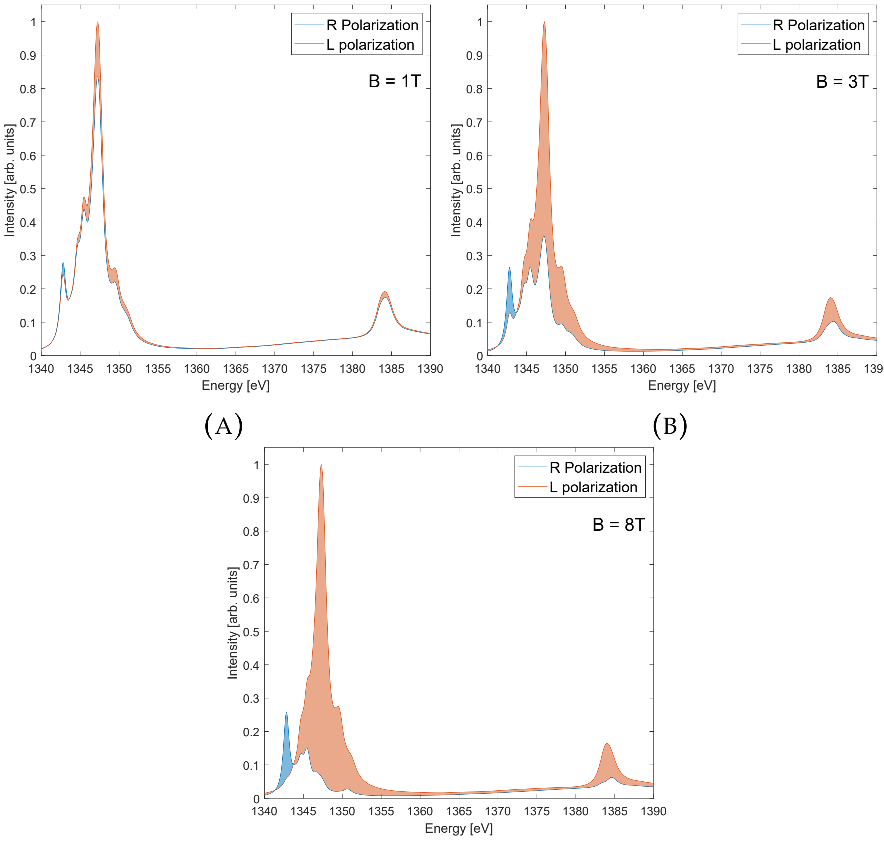

(A)

(B)

(C)

FIGURE 5.4: XMCD spectra of HoIr$_2$Si$_2$. The spectra are acquired at (A) B = 1 T, (B) B = 3 T and (C) B = 8 T along the c axis. R stands for right circular polarization, i.e. the helicity of the incoming radiation lies antiparallel with respect to the applied magnetic field; L stands for left circular polarized light. The dichroism signal is the difference between R and L signals; the shaded area is the integral of XMCD, proportional to the magnetic moment.

of Hund's rules in determining the ground state configuration. Concerning the quantitative evaluation of number of Bohr magnetons, a poor agreement is found with reported data. This is due to the uncertainty in the calculation of the expectation value for the spin moment projection. As already seen in chapter 1, the asphericity of the electronic distribution contributes to the second sum rule, thus leading to wrong evaluations. Indeed, in plot 5.5, the $<S_z>$ data saturate to a value of 3 $\hbar$, different from the 2 $\hbar$ value expected from the application of Hund's rules. Therefore, a positive contribution comes from the term $<T_z>$, which is linked to the non spherical symmetry of Ho^{3+} electronic cloud in the crystalline environment. The enhanced value of $<S_z>$, due to the presence of the crystal, may be seen as a further confirmation of the breaking of spherical symmetry and that a magnetic alignment along the c axis is favoured in HoIr$_2$Si$_2$ sample, in agreement with experimental anisotropy in magnetic susceptibility.

A measurement of the specific heat capacity for HoIr$_2$Si$_2$ is also present in literature and displayed in figure 5.6. The presence of a peak at T = 22 K is a further proof of the occurrence of a phase transition at T_N. The specific heat capacity plotted against temperature is sensitive to the number of states which are thermally accessible. In the approximation of a two-level system, thermal energy enhances the probability of occupation of the excited level. This implies that a peak in the specific heat function is expected, when the energy $k_B T$

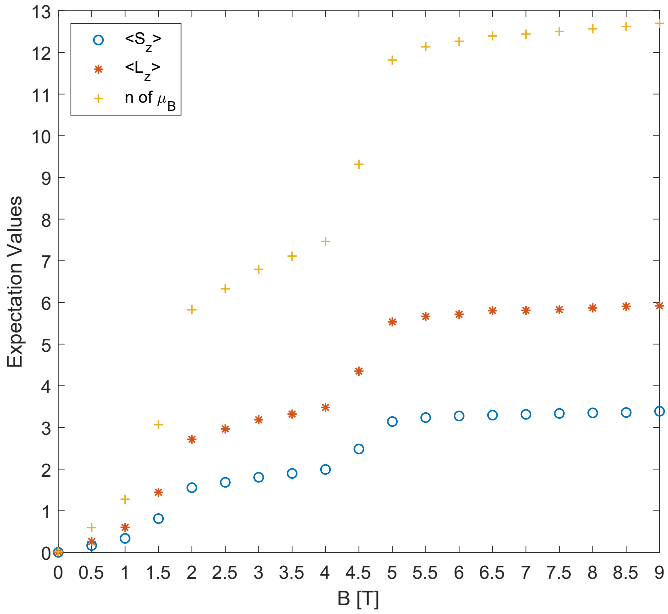

FIGURE 5.5: Results of the application of sum rules, discussed in chapter 1, for the evaluation of magnetic relevant expectation values of HoIr$_2$Si$_2$. The plots of $<S_z>$, $<L_z>$ in unity of $\hbar$ and number of Bohr magnetons as a function of the external applied magnetic field have been obtained with the aid of Pymca, a graphical interface for the analysis of X-ray spectroscopy data. A double step-like background has been subtracted to the data, the steps being set at the edges and in 3/2 ratio relationship, in order to remove contributions not related to $M_{4,5}$ transition.

is in the order of magnitude of the gap between a magnetically ordered ground state and an excited paramagnetic configuration [57]. At very low temperature with respect to T$_N$, thermal energy is not enough to excite transitions from the antiferromagnetic to the paramagnetic state, while at high temperature ground and excited states are equally populated; as a result thermal driven transitions decrease. Then, it is clear that the entropy plot against temperature, which is proportional to the integration of the specific heat capacity, is a measure of the available states for the system at a certain temperature. Therefore, in the framework of the statistical interpretation, entropy can be expressed as $S = Rln(N)$, where R is the gas constant and N the number of available microstates or, in other words, the degeneracy of the system. Figure 5.6 reports the magnetic entropy as well. In order to disentangle the magnetic contribution to specific heat capacity and accordingly entropy, the measured specific heat capacity of LuIr$_2$Si$_2$, a non-magnetic reference compound since the 4f shell of Lu^{3+} is completely filled, has been subtracted in figure. The magnetic entropy at T$_N$ is equal to Rln(4), suggesting a four-fold degeneracy, smaller than the spin-orbit expected seventeen-fold degeneracy for Ho^{3+} ground state. Moreover, measurements saturate to a Rln(12) value for temperature higher than 100 K, still below the atomic ground state degeneracy; the discrepancy, between the confirmation of a paramagnetic behaviour for temperature higher than 100 K and an incomplete reached degeneracy, is accounted, by the authors of the physical properties study of HoIr$_2$Si$_2$, for a large uncertainty in the measured heat

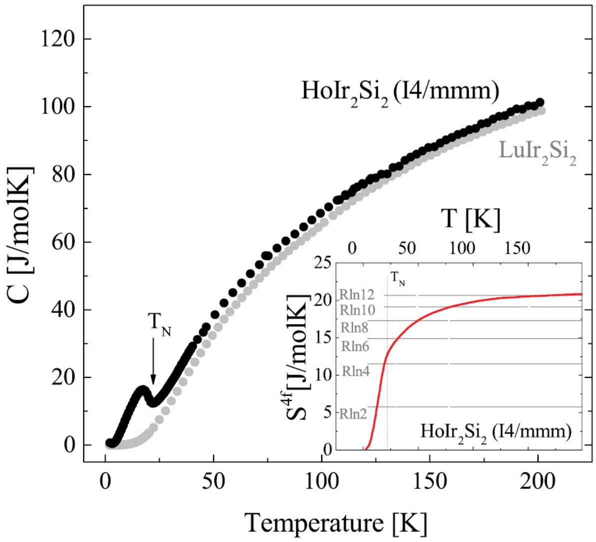

FIGURE 5.6: Measured specific heat capacity for HoIr$_2$Si$_2$. An anomaly is present at T = T$_N$, hinting to the occurrence of a magnetic phase transition. Data are compared with specific heat capacity measurements for a reference non-magnetic compound: Lu^{3+} in LuIr$_2$Si$_2$ is characterized by a complete 4f shell. In the inset, the magnetic entropy is displayed, being S^{4f} = $\int C(HoIr_2Si_2) - C(LuIr_2Si_2)$. The measured values are always smaller than the ground state seventeen-fold degeneracy expected for Ho^{3+}, suggesting for the occurrence of a further splitting of the ground state multiplet $^5I_8$. Image taken from [72].

capacity for T > 50 K.
In the next dedicated paragraph, a brief discussion of why the properties of HoIr$_2$Si$_2$ can be related to CEF effects.

5.1.1 Hints to the presence of CEF effects

The anisotropy in the magnetic susceptibility curves is a clear sign of the presence of solid state effects.
Indeed, in chapter 3 the fitting of magnetic susceptibility data has been listed as a method used to determine the CEF set of parameters. In a qualitative way, the presence of surrounding ligand atoms reduces the symmetry of the rare earth ion from the spherical symmetric one. The electronic orbitals, in the fictitious electric field of the crystal field model, will orient minimizing the electrostatic interaction with the surrounding atoms; therefore, the axis along which magnetic moments align will be labeled as easy axis in contrast to the hard axes of the crystal [19]. A way to determine the CEF set of parameters may be a fitting of the magnetic susceptibility data. However, in HoIr$_2$Si$_2$, a phase transition from a paramagnetic to an antiferromagnetic state occurs at low field for temperature smaller than the Néel temperature $T_N = 22$ K. Then, in order to fit the AFM region of the susceptibility, calculations need to include at least two atoms magnetically coupled, roughly doubling up the calculation time required to calculate the expection values of Ho^{3+}. Moreover, the exchange constant should be considered as a further fitting parameter, increasing the uncertainty of the conclusions.
One may look at the metamagnetic transitions occurring in the magnetization plot towards a ferromagnetic state at B$_1$ and B$_2$ as further proofs of the occurrence of CEF effects in HoIr$_2$Si$_2$. The coexistence of a Zeeman energy term and

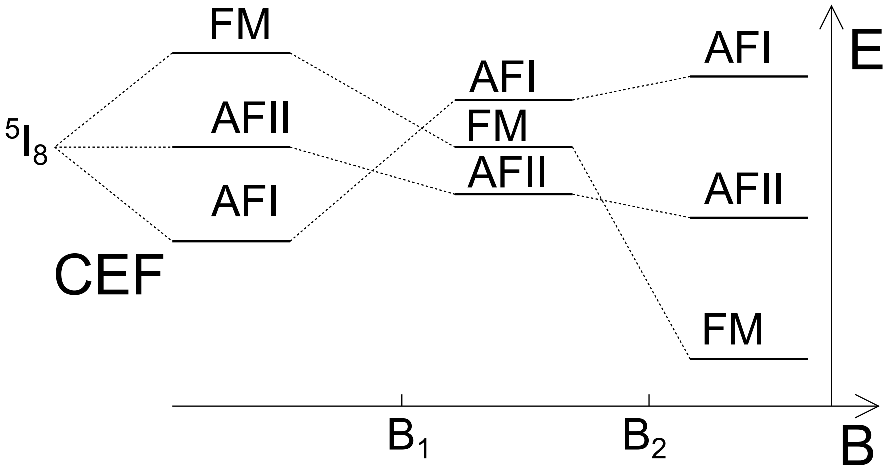

FIGURE 5.7: Scheme displaying the coexistence of CEF and Zeeman energetic terms in HoIr$_2$Si$_2$. The step-like magnetization against applied magnetic field of figure 5.3 can be understood in the view of the dependence of the energy of the magnetic states as a function of the field B. AFI and AFII stand for the first and second antiferromagnetic states in 5.3, whereas FM is the field polarized state reached for B > 6 T.

of the splitting due to the crystal field may be accounted for the occurrence of steps in the magnetization plot; a sketch is proposed in figure 5.7 to show how the mixing of the two energetic terms can lead to a step-like magnetization.
Finally, the measured magnetic entropy suggests for a lifting of the ground state degeneracy. Again, the reduced degeneracy with respect to the isolated ion case can be accounted for as a CEF effect, which further splits the $^5I_8$ multiplet. Moreover, the temperature is a rough measurement of CEF splittings; for instance at T_N the four lowest states are in an energetic range of $\sim k_B T_N$, i.e. $\sim$2 meV.
In the next section, a fitting of XAS data collected for this work will be proposed in order to derive a CEF set.

5.2 XAS analysis

In this section, XAS spectra acquired in the RIXS branch of ID32 will be shown. The spectra are acquired with TEY mode and with an experimental resolution negligible with respect to the estimated intrinsic lifetime broadening of $\sim$1 eV at the M_5 edge, i.e. $\sim$1350 eV. Two experimental geometries have been selected and are shown in figure 5.8: the first with the wavevector q perpendicular to the ab plane, i.e. θ = 90° according to the geometry explained in chapter 2; the latter with θ = 20°, both with light linear polarized in the horizontal plane, i.e. the plane of the beamline. Spectra have been normalized with respect to the incident photon flux at the last mirror before the sample; then, the intensity scale is related to the maximum of the signal for θ = 90° geometry. Both spectra are acquired at 25 K, so that only the lowest states are expected to be thermally occupied.
In XAS spectra two features are distinguishable, labeled M_4 and M_5, according to the IUPAC notation. The features are separated due to spin-orbit interaction of the core-hole 3d electron; according to the reciprocal orientation of **s** and **l**, the quantic number j can be 3/2, i.e. j = l - s = 2 - 1/2, or 5/2. In the first case, being the spin magnetic moment aligned to the magnetic field arising from the orbital motion of the electron, the state is more bounded, therefore a higher photon energy is required to promote the core electron to the valence shell. Accordingly, the M_4 edge is related to the j = 3/2 state, whereas the M_5 edge to the j = 5/2 state. The ratio of intensities of the two edges expected for the single-electron picture, i.e. 3/2, due to the occurrence of multiplet interactions, tackled in chapter 3, does not hold [17].
It is evident from figure 5.8 that depending on the incident angle different spectral features are enhanced or lowered, hinting to the lifting of the spherical symmetry for Ho^{3+} ion. Indeed, as already discussed in chapter 3, the presence of the crystal environment breaks the spherical symmetry, leading to the dependence on the experimental geometry in the spectral shape. In figure 5.8, the dichroism signal, i.e. the difference between the 90°-geometry and the 20°-geometry spectra, is shown as well. The M_5 edge is characterized by more features with respect to the M_4 edge and by a higher dichroism signal as well. Therefore, the fitting of CEF parameters will be carried considering only the M_5 edge in order to reduce time calculation.

Considering the Hamiltonian to include in simulations, no dichroism is expected including only the atomic terms for the spherical symmetry is not broken. In figure 5.9, the calculated spectra with both geometries are displayed for the M$_5$ edge, considering only the atomic Hamiltonian for the electronic transition from d to f shell. No dichroism is present in calculated spectra, which is in agreement with the theory developed so far. Moreover, in calculations all the 17 states of the $^5I_8$ ground state multiplet are considered. These states are not split since the spin-orbit interaction for the 4f shell does not lift the (2J + 1)-fold degeneracy. Therefore, the calculated spectrum with 90°-incidence geometry considering only the atomic Hamiltonian is an isotropic spectrum.
It is clear from figure 5.9, that the scaling factor for the Slater integrals in the final electronic configuration is different from the one obtained through RIXS fitting in chapter 4 for the initial electronic configuration. In literature, the need for different parameters is confirmed [4, 86]. Accordingly, XAS spectroscopy technique is more sensitive to 3d4f electronic configuration than RIXS, where the dependence on the intermediate state is not so directly obtainable.
Since the experimental spectrum with 90°-incident geometry seems to be closer

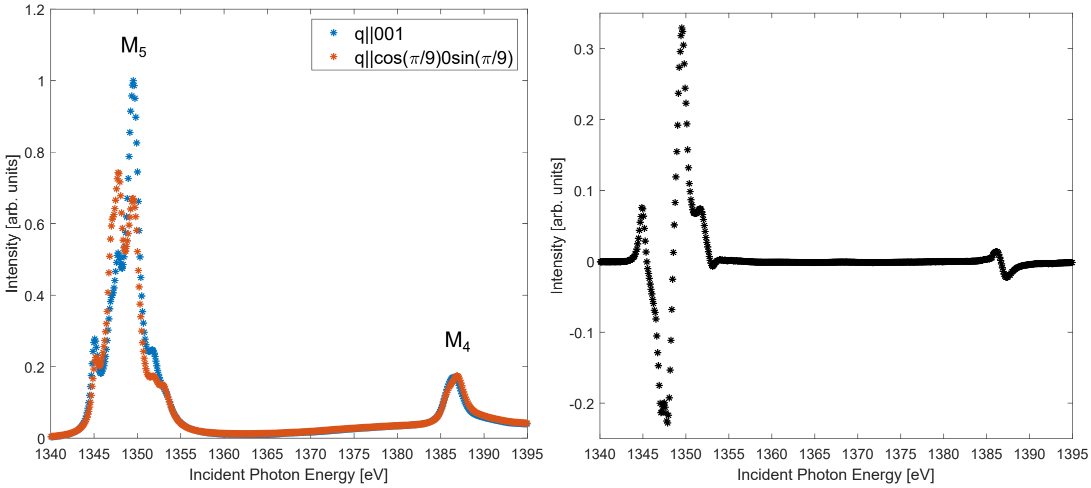

(A) (B)

FIGURE 5.8: (A) XAS spectra of HoIr$_2$Si$_2$: data acquired in two different experimental geometries, parallel to the c axis and lifted of 20° from the ab plane, both with light linear polarized in the horizontal plane and at 25 K. The spin-orbit core-hole split edges have been labeled using the IUPAC notation. M$_5$ edge is at lower incident photon energy, i.e. less bound. Spectra are normalized with respect to the incident photon flux at the last mirror before the sample. The intensity scale is relative to the maximum of the 90°-geometry spectrum. (B) XAS dichroism signal, being the difference between the 90°-geometry and the 20°-geometry spectrum. Differences in the two signals hint to the reduction of symmetry from the isolated atom spherical one. The differences between the two spectra are more significant at the M$_5$ edge with respect to the M$_4$ one.

to the isotropic spectrum, i.e. less affected by the CEF effects, than the 20°-incident one, the first will be used to perform the fitting of the scaling parameter for Slater integrals for the final $3d^9 4f^{11}$ XAS configuration. In figure 5.10 the fitting of the scaling of F^K and G^k parameters, for the final state of M electronic transition of $HoIr_2Si_2$, is reported. Applying the same methods as in chapter 4, the best fitting value is 0.75. Indeed, a proper fitting would require to compare an isotropic spectrum with simulations, in order to disentangle the atomic terms from the crystalline ones; as a result, the obtained value is affected by uncertainty and must not be considered as the best obtainable fitting.
Once fixed the complete set of atomic parameters, the fitting of CEF A_k^m has been performed minimizing the mean squared error between calculated and experimental dichroism signal. In principle, the ground state multiplet $^5I_8$ would require all the CEF parameters for the f shell in a D_{4h} point group symmetry environment, i.e. A_2^0, A_4^0, $A_4^{\pm 4}$, A_6^0 and $A_6^{\pm 4}$. Since simulations involving all the parameters are in practice impossible to be carried, due to the huge calculation time required, a simplified approach will be followed. First of all, the effect of the single A_k^0 parameters on spectra will be evaluated, in order to find reasonable intervals. Simulations involving A_2^0, A_4^0 and A_6^0 over a wide energy interval, i.e. $-300\,\text{meV} \div 300\,\text{meV}$, will be separately performed to extrapolate the effect of the variation of the parameters on the dichroism. According to the agreement with the experimental signal, boundaries for the best-fitting expected parameters will be drawn. Once the intervals are fixed, a simulation

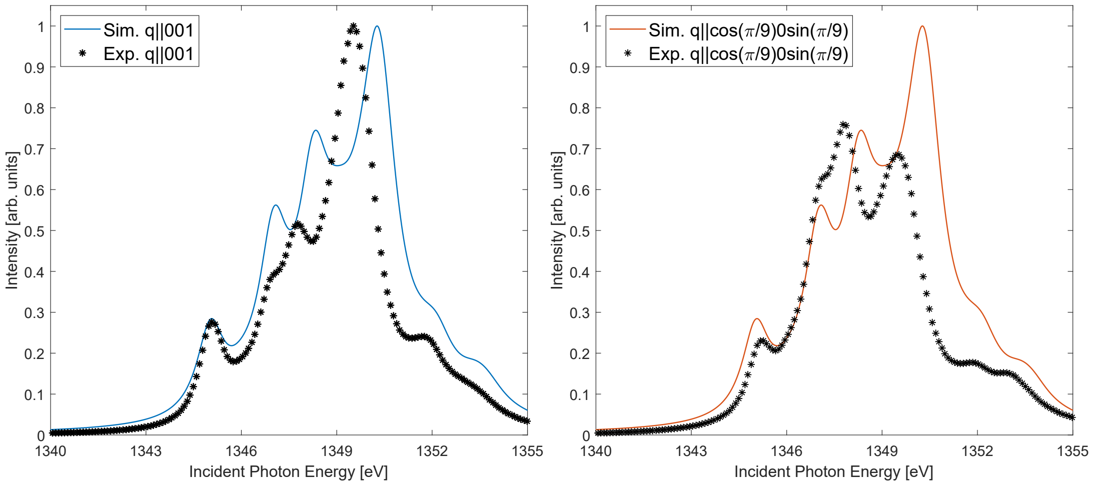

(A)

(B)

FIGURE 5.9: (A) XAS simulated spectrum in the 90°-incident geometry, along with the experimental spectrum of M_5 edge. (B) XAS simulated spectrum in the 20°-incident geometry, along with the experimental spectrum of M_5 edge. In both geometries, the parameters found in chapter 4 for $HoIr_2Si_2$ have been used in calculations, i.e. F^k scaling factor equal to 0.88 and ζ scaling factor to 0.97.

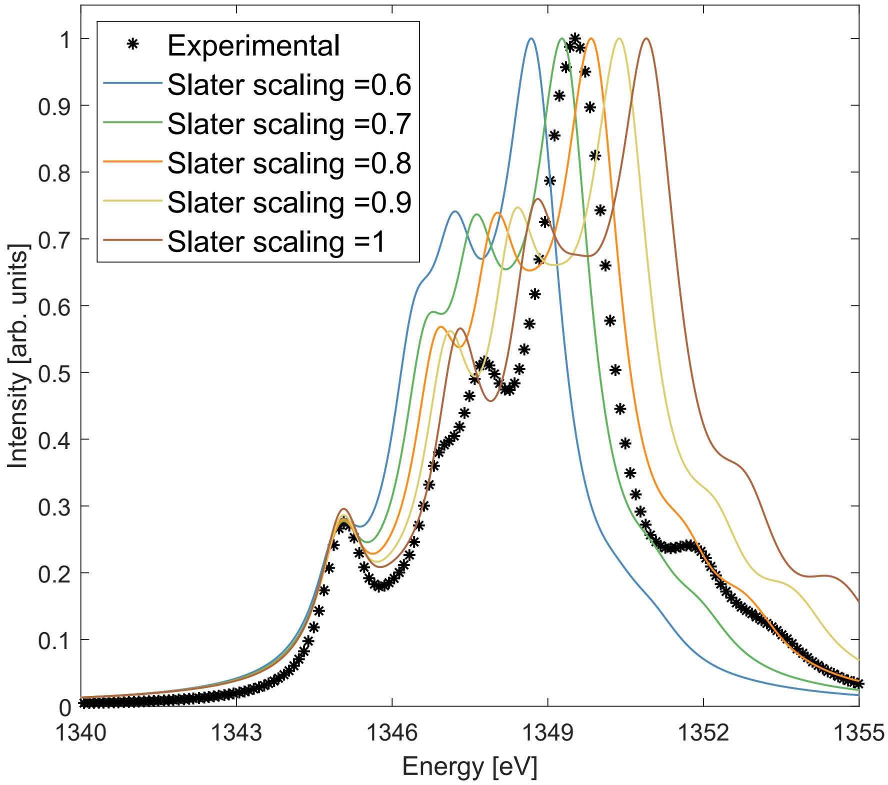

FIGURE 5.10: Fitting of the scaling parameter for Slater integrals in the final 3d^{9}4f^{1}1 electronic configuration. The normal incidence spectrum has been exploited, since it is closer to the isotropic spectrum, i.e. not affected by CEF effects, for HoIr$_2$Si$_2$ M$_5$ edge.

involving all the A_k^0 parameters will be carried, to derive the best combination minimizing the error or, at least, a minimum-error locus in the (A_2^0, A_4^0, A_6^0) space, avoiding false convergence results. Next, the fitting for $A_k^{\pm4}$ parameter will be carried out considering the slight planar anisotropy in magnetization data reported in figure 5.3, keeping in mind that m = 4 parameters mainly affect the planar orientation of wavefunctions. The idea is to reduce the calculation time for XAS spectra fitting, neglecting these higher order corrections, thus reducing the number of possible combinations. Moreover, XAS cross-section is mainly dipole dominated so that the technique is insensitive to effects related to four-fold planar symmetry CEF parameters [4].

In figure 5.11 the fitting for the A_2^0 parameter is reported considering the dichroism signal. For negative values of A_2^0, one gets a reverse dichroism signal with respect to the experimental one. For $A_2^0 > 0\,\mathrm{meV}$ a doublet ground state, with $J_z = \pm 8$ is found, hinting to an orientation of the electronic spin-orbital wavefunctions in the ab plane and to a magnetic moment aligned to the c axis, in agreement with the previous discussed magnetic properties of the sample. Therefore, the set of parameters needed to build the crystal field will include a positive value for A_2^0. The evidence that the sign of A_2^0 determines a magnetocrystalline anisotropy can be found in literature [19, 20]. In other words, the CEF A_2^0 parameter is linked to the position of the nearest neighbors with higher charge density. A positive sign implies that the fictitious electric field, which best resembles the crystalline environment, is built putting the closest-to-ion charges on the z axis. Then, the minimization of the CEF electrostatic potential requires the ground state to have a planar shape rather than an axial one. Thus, the orbital motion is mainly bound to be in the ab plane, with the orbital angular moment aligned to the c axis. Moreover, increasing the absolute value

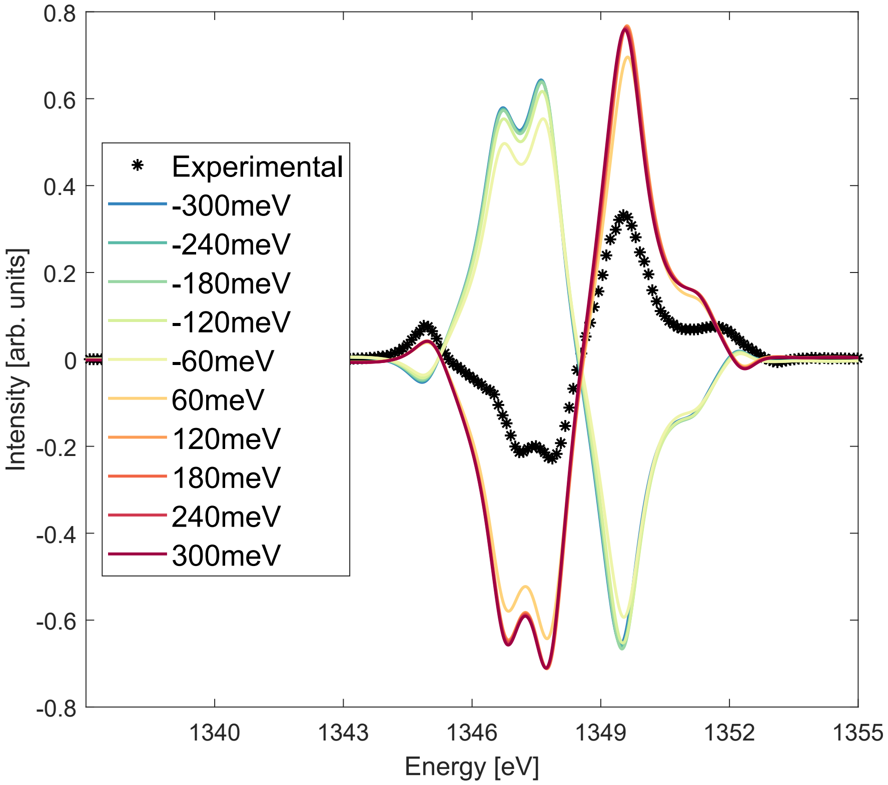

FIGURE 5.11: Simulated dichroism as a function of the CEF parameter A_2^0, being all the other parameters set to 0, for M_5 edge of $HoIr_2Si_2$ compared to the experimental one.

of the parameter the dichroism enhances, in accordance to the fact that states are more split if CEF corrections are more relevant, which is ultimately related to the fact that the spherical symmetry is lost if temperature allows occupation of only the lowest states. Then, a reasonable interval for the fitting of A_2^0 may be 10 meV ÷ 60 meV.

With the same approach, the effect of the variation of A_4^0 has been analyzed and reported in figure 5.12. The shape of the dichroism is obtained for any value of A_4^0 different from zero. The contribution of the 4th-order term then will be taken into account as a further correction to the effect of A_2^0. Indeed, the effect of higher orders parameter is to better define the shape of the ground state orbitals, once A_2^0 sets whether the wavefunction is oblate or prolate [19]. A reasonable interval for A_4^0 may be then -150 meV ÷ 60 meV.

In figure 5.13, simulated dichroism varying A_6^0 is reported along with experimental data. From simulations the interval -60 meV ÷ 60 meV has been selected.

Simulations varying A_2^0, A_4^0 and A_6^0 respectively in the intervals 10 meV ÷

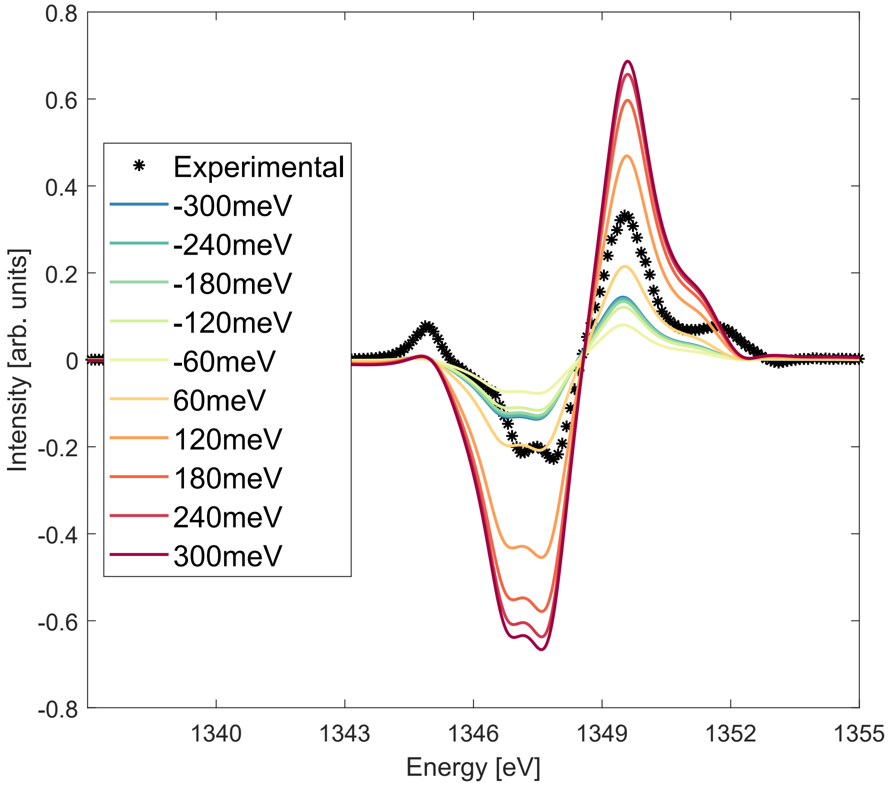

FIGURE 5.12: Simulated dichroism as a function of the CEF parameter A_4^0, being all the other parameters set to 0, for M_5 edge of HoIr$_2$Si$_2$ compared to the experimental one.

60 meV, −150 meV ÷ 60 meV and −60 meV ÷ 60 meV, with a mesh of 10 meV have been performed. In figure 5.14, the mean squared error between simulated and experimental dichroism at M_5 edge is displayed. The size of the dots is proportional to the agreement between simulations and data, i.e. the higher is the mean squared error associated to a certain combination (A_2^0, A_4^0, A_6^0), the smaller is the point in the chart. In chart 5.14, the five combinations leading to the lowest mean squared error are marked in red.

All the five sets of parameters yield to the same pure $J_z = \pm 6$ doublet ground state. Moreover, all the highlighted combinations share the same energy scheme of CEF excited levels with very slight differences regarding the splitting energies. The energy schemes for $^5I_8$ multiplet, associated to each marked combination, are depicted in figure 5.15.

The fact that, in all found solutions, the $J_z = \pm 8$ is the most CEF excited state may be an explanation of why in magnetization curve shown in figure 5.3, the saturation value for high applied external magnetic field does not achieve the expected theoretical value of 10 μ_B. Moreover, all the proposed solutions share the same ground state and first excited levels within $\sim 2\,\text{meV} \div 3\,\text{meV}$, in good agreement with the specific heat plot displayed in figure 5.6, since the splitting between the ground doublet and the first excited one is close to $k_B T_N \sim 2\,\text{meV}$; only set 2 would lead to a six-fold degeneracy at T_N, higher than the four-fold measured one. It is noteworthy that the states are pure J_z, this is due to the fact that no $A_k^{\pm 4}$ have been included so far in calculations. Actually, as seen in chapter 3, including $A_k^{\pm 4}$ parameters, a mixing of J_z states will occur. As well as that, solutions associated to A_k^0 CEF parameters display a cylindrical symmetry, for the spherical harmonics, with m = 0, used to build the CEF Hamiltonian, do not break the symmetry in the ab plane; the reader can see for instance the drawn renormalized spherical harmonics in [42]. Therefore, a proper combination is expected to be close to the proposed ones, since the magnetic susceptibility exhibits no planar anisotropy, while magnetization curve shows only to be slightly anisotropic, considering (100) and (110) axes, at very high applied magnetic field. One last remark about the provided energy schemes in figure 5.15. The CEF contribution to the overall Hamiltonian does not lift completely the $^5I_8$ multiplet symmetry; actually, the levels are at least two-fold degenerate, except for $J_z = 0$ state, which in set 4 is split from the other doublets. This is the typical case in systems characterized by an integer value of J, i.e. an even number of electrons filling the valence shell [19]. The fact that each doublet displays a zero net magnetic moment is a consequence of the time reversal symmetry [87]. Indeed, the fictitious electric field set by the CEF Hamiltonian does not distinguish between positive or negative oriented moments, once a reference direction has been fixed. As a result, the crystal field driven anisotropy should be defined as uniaxial, different from an unidirectional one which would lift the doublets degeneracy. Taking into account magnetic exchange terms in the Hamiltonian, as shown in the next section, will set an easy direction for the

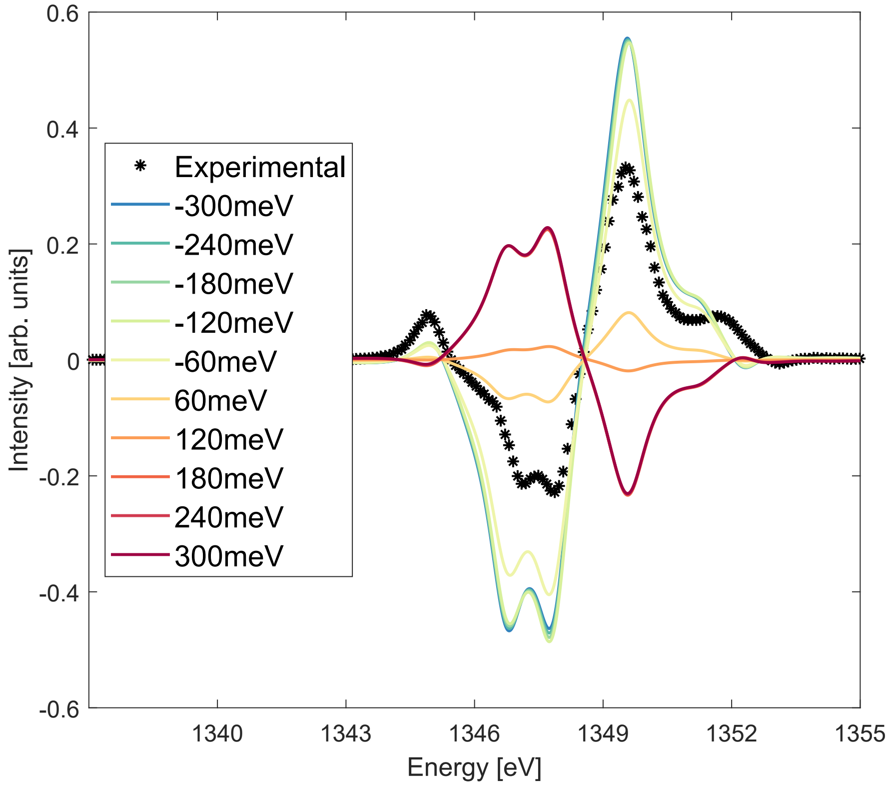

FIGURE 5.13: Simulated dichroism as a function of the CEF parameter A_6^0, being all the other parameters set to 0, for M_5 edge of $HoIr_2Si_2$ compared to the experimental one.

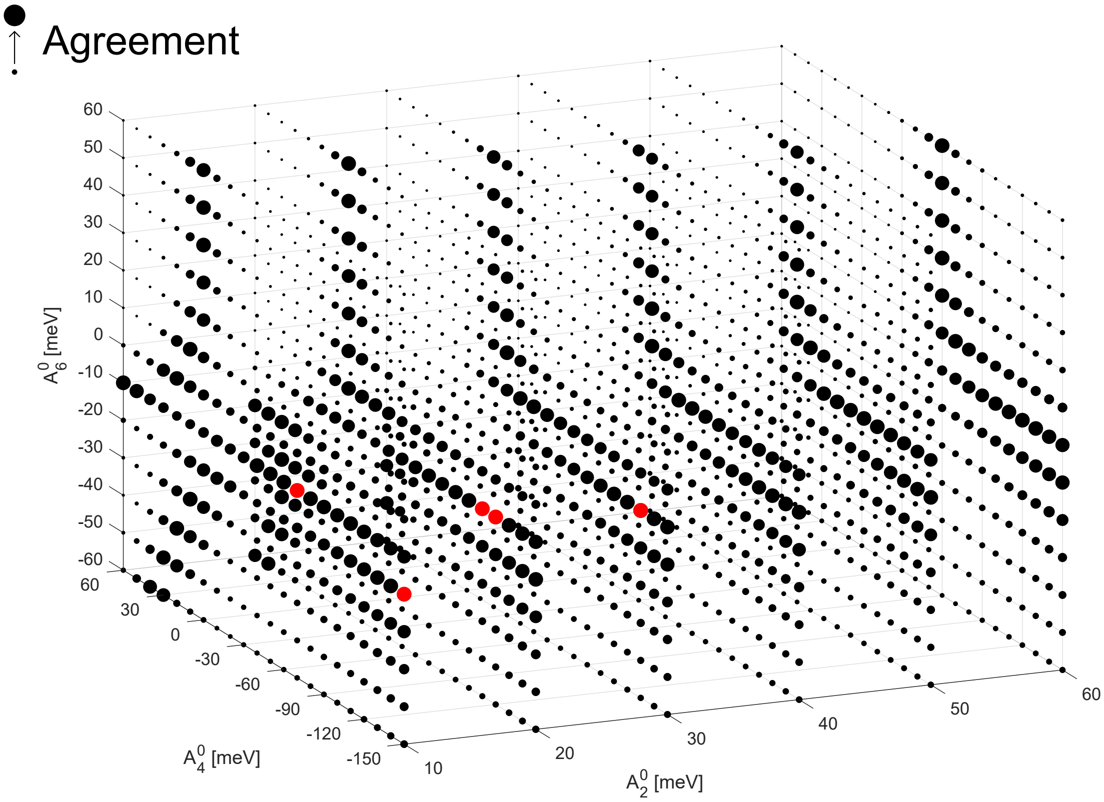

FIGURE 5.14: Inverse mean squared error between the simulated and experimental dichroism at M_5 edge for $HoIr_2Si_2$, depending on the combination of CEF parameters A_2^0, A_4^0 and A_6^0. The size of the dots is proportional to the agreement between simulations and experiments; bigger points are associated to simulations closer to experimental data. In red are marked the five best fitting combinations of CEF parameters, i.e. the ones associated to the five lowest mean squared errors.

atomic magnetic moments to align along.

In the next section, starting from the configuration which yields the least mean squared error, i.e. set 1 in figure 5.15, simulations of the magnetic properties of $HoIr_2Si_2$ previously depicted will be proposed.

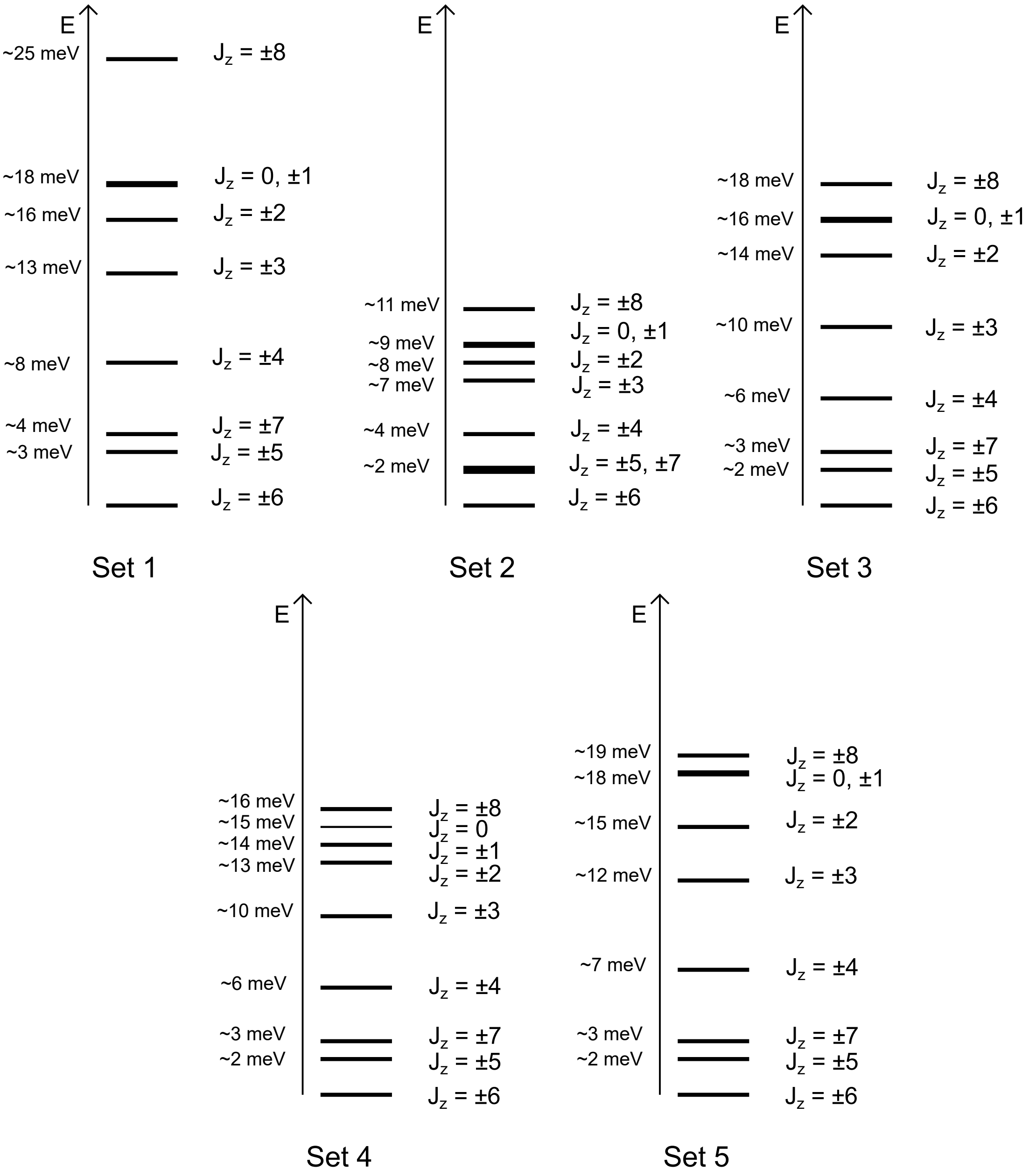

FIGURE 5.15: Energy schemes of the five best solutions, from figure 5.14, of $^5I_8$ multiplet for HoIr$_2$Si$_2$. All the combinations share the same ground state and excited energy levels. Set 1: A_2^0 = 10 meV, $A_4^0 = -150$ meV, $A_6^0 = -20$ meV. Set 2: A_2^0 = 10 meV, $A_4^0 = -70$ meV, $A_6^0 = -10$ meV. Set 3: A_2^0 = 20 meV, $A_4^0 = -120$ meV, $A_6^0 = -10$ meV. Set 4: A_2^0 = 20 meV, $A_4^0 = -110$ meV, $A_6^0 = -10$ meV. Set 5: A_2^0 = 30 meV, $A_4^0 = -130$ meV, $A_6^0 = -10$ meV.

5.3 Simulated magnetic properties

As said in the previous section, a very slight planar anisotropy can be deduced by magnetization curves displayed in figure 5.3; indeed, the difference in the measured magnetic moment along (100) and (110) directions is $\sim 1\ \mu_B$ at ~ 9 T applied magnetic field, whereas in magnetic susceptibilities data shown in figure 5.2 no difference can be detected between planar axes. Therefore, a small correction is needed from $A_k^{\pm 4}$ parameters to the proposed schemes in figure 5.15, which display a cylindrical symmetry, being solutions of a CEF Hamiltonian fully symmetric with respect to rotations in the plane ab, i.e. built with $A_k^{m=0}$ terms.

Thus, four combinations of $A_k^{\pm 4}$ have been included in CEF set of parameters starting from the combination yielding the least mean squared error in figure 5.14, i.e. set 1 in figure 5.15. Namely, in ($A_4^{\pm 4}$, $A_6^{\pm 4}$) space the four combinations with parameters equal to ±10 meV have been considered.

In order to simulate magnetic states of $HoIr_2Si_2$, the basis set of calculations must be extended; it is necessary to include more than one atomic site to account for collective exchange driven magnetic phenomena. In performed simulations the simplest configuration has been considered, i.e. two atomic sites. The considered atoms have been antiferromagnetically coupled, in agreement with the drawn properties of $HoIr_2Si_2$ seen in the previous. Moreover, since the antiferromagnetic order for $HoIr_2Si2$ displays a propagation vector (0, 0, 1/2) [88], the coupling considered in calculations is only along c axis, i.e. the two ion sites can be modeled as an Ising-type system [89].

Thus, an exchange term is added to calculations, i.e. a Heisenberg-type Hamiltonian, considering only projections along c axis of the two associated spin moments,

$$\mathcal{H}_{ex} = -J_{ex} S_1 \cdot S_2. \tag{5.2}$$

In eq. 5.2, J_{ex} is the exchange constant which couples the two simulated ion sites. S_i stand for the projection along z of the spin moment for ion at site i. It is clear then, that in the one-dimensional Ising model the scalar product between spin moments is replaced by the multiplication of pure numbers. Accordingly, with a positive J_{ex} a ferromagnetic alignment is favoured, whereas antiferromagnetic order arises with a negative exchange constant. Hence, a negative constant has been included in calculations, i.e. $J_{ex} = -0.91$ meV. The absolute value has been fixed by fitting in calculations the maximum peak of susceptibility at the experimental Néel temperature T_N.

It is noteworthy that in $HoIr_2Si_2$ is expected a ferromagnetic coupling between ionic sites moving along ab planes as well. In the considered model, due to the limitation to a two-site cluster, no other coupling interactions but the antiferromagnetic one have been included. Actually, an extension of the considered sites may lead to a closer agreement between simulations and experimental data, at the cost of an increase of calculation time, which roughly scales with the number of considered sites. As a final remark to the simulated magnetization curves shown in figure 5.16, in order to speed up calculations, only the five lowest states of $^5I_8$ multiplet have been considered in the evaluation of the expectation value of number of Bohr magnetons per ion. This is not expected to affect the analysis, since performing simulations at T = 2 K, i.e. considering a thermal energy of ∼0.2 meV, only the ground state is expected to be populated; once again, the reader can see figure 5.15 to have an idea of the differences in energy between ground and excited states.

Applying an external magnetic field, i.e. including a Zeeman term in the Hamiltonian, this picture still holds, for even at 9 T corrections to the energy levels will be in the order of ∼meV, thus, including the five lowest states, the contribution coming from possibly populated excited levels is safely accounted with the Boltzmann factor. In all simulated data the experimental anisotropy between c axis and ab plane is reproduced, confirming the quality of the fitting of XAS dichroism signal. Moreover, a clear metamagnetic transition is present for B ∼4 T; since in the exploited model the only energetic terms considered are exchange coupling and crystal field corrections, the transition can be safely accounted for as a consequence of the crystalline environment, hosting Ho^{3+} ion.

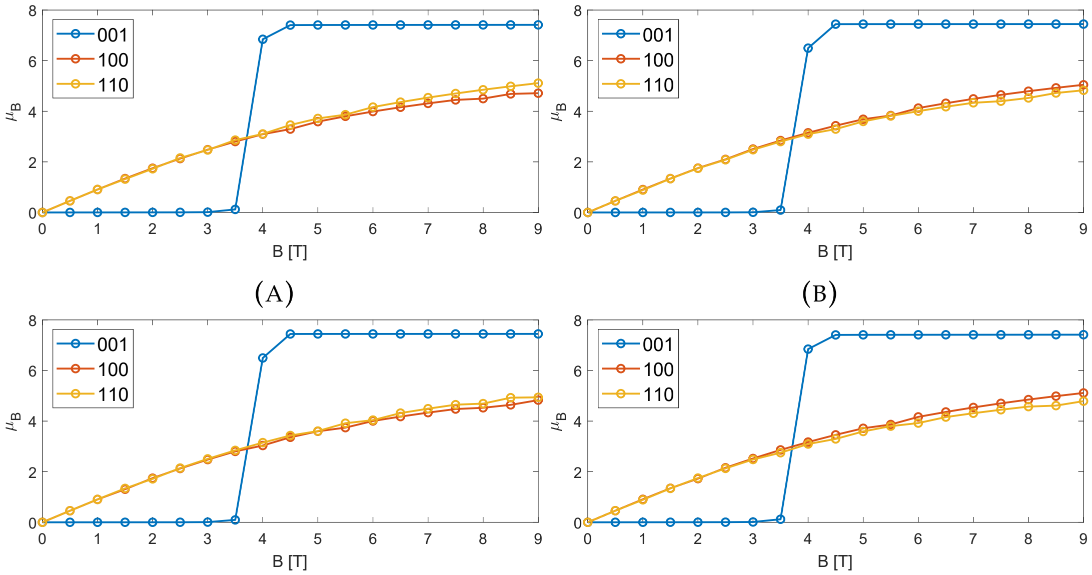

(A) (B)

(C) (D)

FIGURE 5.16: Simulations of magnetization curve at T = 2 K for Ho^3+ ion, as a function of $A_k^{\pm 4}$ CEF parameters, starting from A_k^0 parameters of set 1 in figure 5.15. (A) $A_4^{\pm 4} = -10$ meV, $A_6^{\pm 4} = -10$ meV. (B) $A_4^{\pm 4} = -10$ meV, $A_6^{\pm 4} = 10$ meV. (C) $A_4^{\pm 4} = 10$ meV, $A_6^{\pm 4} = -10$ meV. (D) $A_4^{\pm 4} = 10$ meV, $A_6^{\pm 4} = 10$ meV. All simulations were performed accounting for a probability of occupation of excited states given by Boltzmann factor at T = 2 K.

Still, considering simulated magnetization along (001) axis, there are two major discrepancies with respect to data reported in literature; the most evident one is the absence of one of the two steps, namely the one occurring at ∼1.4 T; as well as that, the saturation value is slightly smaller than what reported: all simulations saturate for B > 6 T to a value ∼7.4 μ_B. The absence of the first step in simulations can be accounted for as a consequence of the limitations of the exploited model system. Indeed, in HoIr$_2$Si$_2$ other exchange couplings are expected to be present, e.g. a ferromagnetic coupling among Ho^{3+} ionic sites along ab planes and along c axis, considering alternating layers of ordered magnetic atoms. All in all, the coexistence of more interactions, both local, such as the CEF term, and collective exchange couplings, may lead to metamagnetic states, in which some of the magnetic moments orient parallel to the external field, while other sites do not [83]. An extension of the cluster considered in calculations or an application of a statistical approach, in which each site may orient or not parallel to the external magnetic field, with a probability given by the ratio between Zeeman and exchange term, could confirm this hypothesis. Regarding the latter difference with respect to experimental data, simulations suggest that the ground state levels should exhibit an expectation value for the projection of angular moments along z higher than the $J_z = \pm 6$ doublet solutions proposed in figure 5.15. Therefore, among all the possible combinations proposed in chart 5.14, solutions yielding a doublet ground state characterized by $J_z = \pm 7$ or $J_z = \pm 8$ would result in a proper saturation value for magnetic moment along c axis.

Concerning simulations of the magnetization along (100) and (110) axis, among the explored combinations in ($A_4^{\pm 4}$, $A_6^{\pm 4}$) space, $A_4^{\pm 4} = A_6^{\pm 4} = 10\,\text{meV}$ leads to the proper anisotropy between planar axes, suggesting for a positive sign of both terms.

In order to check if the agreement with experimental data improves, in the light of the above, two simulations are proposed in figure 5.17, with two sets from chart 5.14 and including $A_4^{\pm 4} = A_6^{\pm 4} = 10\,\text{meV}$; the first is $A_2^0 = 10\,\text{meV}$, $A_4^0 = -100\,\text{meV}$, $A_6^0 = -40\,\text{meV}$ which yielded a doublet $J_z = \pm 7$ ground state; the second has $A_2^0 = 10\,\text{meV}$, $A_4^0 = 0\,\text{meV}$, $A_6^0 = 40\,\text{meV}$, which leads to a $J_z = \pm 8$ ground state. Simulated data along (001) axis, with CEF set of parameters in figure 5.17 (A), saturate to a value closer to the one reported in literature, i.e. $\sim 8.6\ \mu_B$. However, among proposed solutions, combination (D) from figure 5.16 still seems the closest to experimental data; the reader may check the agreement between planar magnetization measurements with simulated points.

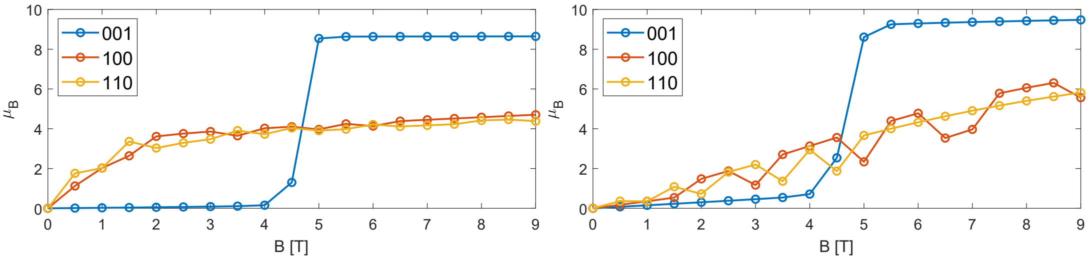

(A) (B)

FIGURE 5.17: Simulated magnetizations for HoIr$_2$Si$_2$, including $A_4^{\pm 4} = A_6^{\pm 4} = 10\,\text{meV}$ to set (A) $A_2^0 = 10\,\text{meV}$, $A_4^0 = -100\,\text{meV}$, $A_6^0 = -40\,\text{meV}$ and to (B) $A_2^0 = 10\,\text{meV}$, $A_4^0 = 0\,\text{meV}$, $A_6^0 = 40\,\text{meV}$. (A) yielded a $J_z = \pm 7$ doublet ground state, without considering $A_k^{\pm 4}$ parameters; (B) led to a $J_z = \pm 8$ doublet ground state. Both simulations were performed accounting for a probability of occupation of excited states given by Boltzmann factor at T = 2 K.

In table 5.1 all the parameters which yielded this solution are reported, along with the technique exploited to derive them.

Finally, simulations starting from a doublet $J_z = \pm 8$ and including $A_k^{\pm 4} = 10\,\text{meV}$

in figure 5.17 (B) seems to be quite in disagreement with experimental data.

To further check the quality of calculations compared to experiments, a plot of the simulated magnetic susceptibility for Ho^{3+} with all the found parameters for the best solution is proposed in figure 5.18. Once again, the agreement seems to be good: axis to planar anisotropy is confirmed, with a ratio between simulated points along c and planar ones close to what reported in paramagnetic regime experimental data in figure 5.2. Performed simulations strongly suggest that the exploited model can be properly applied to the description of magnetic properties of $HoIr_2Si_2$.

Parameter	Value	Methodology
Slater scaling *ff*	0.88	RIXS fitting
ζ scaling *ff*	0.97	RIXS fitting
Slater scaling *df*	0.75	XAS fitting
A_2^0	10 meV	XAS, magnetization fitting
A_4^0	−150 meV	XAS, magnetization fitting
$A_4^{\pm 4}$	10 meV	XAS, magnetization fitting
A_6^0	−20 meV	XAS, magnetization fitting
$A_6^{\pm 4}$	10 meV	XAS, magnetization fitting
$J_{ex,c-axis}$	0.91 meV	susceptibility maximum fitting

TABLE 5.1: Parameters found in this work for Ho^{3+} in $HoIr_2Si_2$. The reported parameters are exploited to model the magnetization of Ho^{3+} in figure 5.16 (D).

Finally, in figure 5.19 a sketch of the ground state wavefunction, resulting from the diagonalization of the Hamiltonian for Ho^{3+}, built with found parameters reported in table 5.1, is displayed, along with the energetic scheme of $^5I_8$ multiplet.

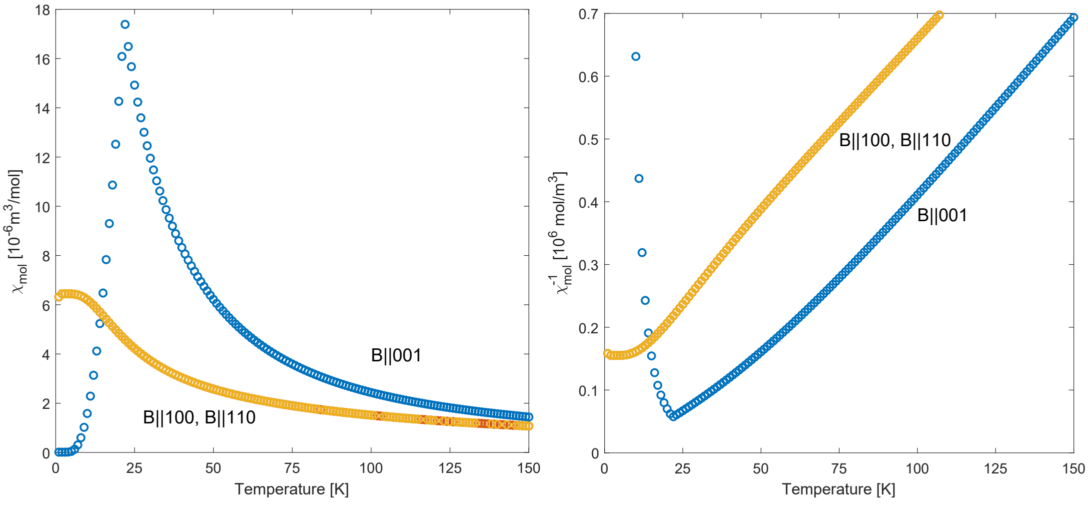

(A) (B)

FIGURE 5.18: Simulated magnetic susceptibility χ_{mol}(T) (A) and inverse susceptibility χ^{-1}_{mol}(T) (B) as a function of temperature and with an applied magnetic field B = 0.1 T, modeling Ho^{3+} hosted in HoIr$_2$Si$_2$, with found parameters in table 5.1. The agreement with experimental data is good, in terms of c-axis to ab-plane anisotropy and characteristic of the inverse curves.

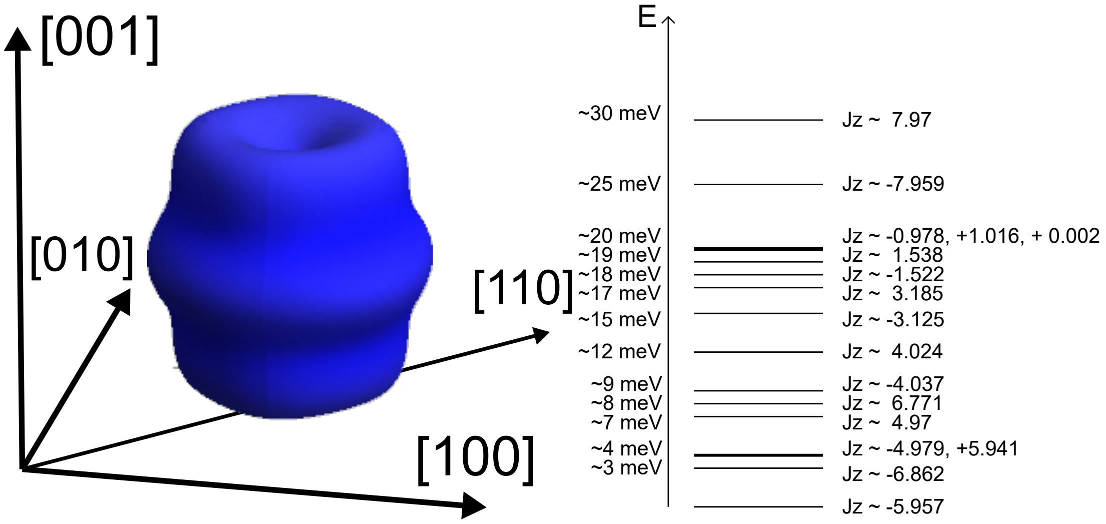

FIGURE 5.19: Plot of spin-orbital ground state for Ho^{3+} on the left, along with energy scheme of levels belonging to multiplet ^{5}I$_8$ on the right. The states are solution of Hamiltonian built with parameters listed in table 5.1. Anisotropy between c axis and ab plane is evident; a small difference between (100) and (110) direction can be detected, orbital exhibiting small bumps towards (110) direction and 90°-shifted ones. Levels still display a leading J$_z$ character, even if a mixing of states ±4 J$_z$-split states occurred due to $A_k^{\pm4}$ CEF parameters. The two-fold degeneracy which was present in energetic schemes proposed in figure 5.15 is lifted by the exchange term, which fixes an unidirectional anisotropy. The spin-orbital plot has been drawn with the aid of Mathematica package of Quanty.

Chapter 6

Summary and outlooks

In this thesis work, an analysis of X-ray spectroscopic data, with the aid of full multiplet atomic based calculations has been proposed.

Theoretical fundamentals of X-ray Absorption Spectroscopy (XAS) and Resonant Inelastic X-ray Scattering (RIXS) are provided to the reader in chapter 1.

In chapter 2, a quick description of ID32 beamline at European Synchrotron Radiation Facility (ESRF) is proposed, highlighting the striking results achieved in terms of energy resolution and repeatability in measurements, as well as the flexibility left to users.

Chapter 3 sets the proper framework to model the Hamiltonian for a rare earth ion in a crystalline environment; exploiting the atomic character of 4f valence shell, most of the properties of lanthanides can be described in terms of a local Ansatz.

Chapter 4 and 5 contain a fitting of the parameters needed to properly model physics of rare earth compounds. In particular, chapter 4 is based on the sensitivity of RIXS to *ff* excitations, i.e. scaling parameters modeling electrostatic and spin-orbit interactions have been fitted for four rare earth ion hosting compounds; namely, $CeRh_2As_2$, $NdRh_2Si_2$, $GdIr_2Si_2$ and $HoIr_2Si_2$.

The found atomic parameters for $HoIr_2Si_2$ have been the starting step in the investigation of its intriguing magnetic properties in chapter 5. A combined analysis of XAS spectra and magnetization curves performed with the aid of Quanty, a full multiplet based script language, yielded a set of crystal electric field (CEF) parameters for Ho^{3+} ground state in $HoIr_2Si_2$. The model Hamiltonian built with the found parameters has been finally tested, comparing simulated magnetic data points with experiments. Indeed, the combination of information coming from more techniques is crucial in avoiding false convergence results in fitting processes.

The performed study confirmed that rare earth compounds are model materials to be investigated with high resolution spectroscopic techniques, e.g. RIXS and XAS. Moreover, a local approach is able to account for most of the properties of rare earth ions hosted in a crystalline environment; solid state effects are properly reproduced by CEF theory. As well as that, with an extension of the number of sites, from a single ion to a cluster of at least two coupled atoms, magnetic properties arising from the concurrence of crystalline and exchange interactions can be fairly simulated. Then, a similar approach could be applied to samples exhibiting similar magnetic properties, with the final aim of fully describe systems characterized by tunable magnetic states, which are clearly promising for spintronic applications.

The carried out investigation relied on an indirect approach, to find the ground state for Ho^{3+} in $HoIr_2Si_2$ which is in best agreement with data reported in literature. Indeed, the splittings between ground state and excited levels in $^5I_8$ low energetic multiplet for Ho^{3+} ion have been derived by reproduction of effects which come as a consequence of the energetic scheme and not directly resolving levels. Thus, achieved results leave some room for interpretation, for many parameters had to be included in order to reproduce data, each of them adding uncertainty to drawn conclusions. As well as that, the performed analysis is mainly sensitive to the ground state rather than directly resolving the energetic scheme of the low excited levels in $^5I_8$ multiplet.

A direct approach in principle could be carried by fitting RIXS spectra, but the achieved energy resolution, i.e. $\sim$100 meV at $\sim$1458 eV M_5 edge, is not sufficient to resolve levels whose maximum splitting is in the order of tens of meV (the reader may see figure 5.15). Nonetheless, an analysis of excited multiplets in RIXS spectra exploiting angular sensitivity, i.e. measuring dichroism signals, could shed more light on CEF splittings occurring in $HoIr_2Si_2$ at excited levels. In principle, a relation between crystalline effects occurring at high excited levels and the ones affecting ground state can be deduced.

Investigations similar to the one proposed for this work are currently piling up large amounts of data, regarding heavy fermionic systems and more in general rare earth compounds, with the purpose of building up a general scheme able to properly describe this class of materials. A model, which is fully able to account for the plethora of striking properties associated to rare earth dilute materials, is the key to the understanding of exotic effects, such as intriguing magnetic ordered states and unconventional magnetically driven superconductivity. Such a theory could bridge the gap between superconductive and collective magnetic phenomena which are suspected to be strongly correlated.

Bibliography

[1] G. Liu, B. Jacquier. *Spectroscopic Properties of Rare Earths in Optical Materials*. Springer, 2005.

[2] K. N. R. Taylor, M. I. Darby. *Physics of Rare Earth Solids*. Chapman and Hall Ltd., 1972.

[3] J. X. Boucherle, J. Flouquet, C. Lacroix, J. Rossat-Mignod, ed. *Anomalous Rare Earths and Actinides Valence Fluctuation and Heavy Fermions*. Journal of Magnetism and Magnetic Materials, 1987.

[4] Andrea Amorese. "Une caractérisation complète du champ cristallin dans les réseaux Kondo à base de Cérium par diffusion inélastique résonante de rayons X". 2017GREAY013. PhD thesis. 2017. URL: `http://www.theses.fr/2017GREAY013/document`.

[5] N.B. Brookes et al. "The beamline ID32 at the ESRF for soft X-ray high energy resolution resonant inelastic X-ray scattering and polarisation dependent X-ray absorption spectroscopy". In: *Nuclear Instruments and Methods in Physics Research Section A: Accelerators, Spectrometers, Detectors and Associated Equipment* 903 (2018), pp. 175–192. ISSN: 0168-9002. DOI: `https://doi.org/10.1016/j.nima.2018.07.001`. URL: `http://www.sciencedirect.com/science/article/pii/S0168900218308234`.

[6] R Jenkins et al. "IUPAC—nomenclature system for x-ray spectroscopy". In: *X-Ray Spectrometry* 20.3 (1991), pp. 149–155.

[7] H. Burzlaff and H. Zimmermann. "Point-group symbols". In: *International Tables for Crystallography Volume A: Space-group symmetry*. Ed. by Th. Hahn. Dordrecht: Springer Netherlands, 2002, pp. 818–820. ISBN: 978-1-4020-5406-8. DOI: `10.1107/97809553602060000524`. URL: `https://doi.org/10.1107/97809553602060000524`.

[8] Akio Kotani and Shik Shin. "Resonant inelastic x-ray scattering spectra for electrons in solids". In: *Rev. Mod. Phys.* 73 (1 Feb. 2001), pp. 203–246. DOI: `10.1103/RevModPhys.73.203`. URL: `https://link.aps.org/doi/10.1103/RevModPhys.73.203`.

[9] F.M.F. de Groot. "X-ray absorption and dichroism of transition metals and their compounds". In: *Journal of Electron Spectroscopy and Related Phenomena* 67.4 (1994), pp. 529–622. ISSN: 0368-2048. DOI: `https://doi.org/10.1016/0368-2048(93)02041-J`. URL: `http://www.sciencedirect.com/science/article/pii/036820489302041J`.

[10] Maurits Haverkort. "Spin and orbital degrees of freedom in transition metal oxides and oxide thin films studied by soft x-ray absorption spectroscopy". PhD thesis. Universität zu Köln, 2005. URL: `https://kups.ub.uni-koeln.de/1455/`.

[11] F. Strigari et al. "Crystal-field ground state of the orthorhombic Kondo insulator $CeRu_2Al_{10}$". In: *Phys. Rev. B* 86 (8 Aug. 2012), p. 081105. DOI: `10.1103/PhysRevB.86.081105`. URL: `https://link.aps.org/doi/10.1103/PhysRevB.86.081105`.

[12] Thomas Willers et al. "Correlation between ground state and orbital anisotropy in heavy fermion materials". In: *Proceedings of the National Academy of Sciences* 112.8 (2015), pp. 2384–2388. ISSN: 0027-8424. DOI: `10.1073/pnas.1415657112`. eprint: `https://www.pnas.org/content/112/8/2384.full.pdf`. URL: `https://www.pnas.org/content/112/8/2384`.

[13] F. Strigari. "Hybridization and crystal-field effects in Kondo insulators studied by means of core-level spectroscopy". PhD thesis. Universität zu Köln, 2015.

[14] L. H. Tjeng et al. "Temperature dependence of the Kondo resonance in $YbAl_3$". In: *Phys. Rev. Lett.* 71 (9 Aug. 1993), pp. 1419–1422. DOI: `10.1103/PhysRevLett.71.1419`. URL: `https://link.aps.org/doi/10.1103/PhysRevLett.71.1419`.

[15] Masaichiro Mizumaki, Satoshi Tsutsui, and Fumitoshi Iga. "Temperature dependence of Sm valence in SmB6 studied by X-ray absorption spectroscopy". In: *Journal of Physics: Conference Series*. Vol. 176. 1. IOP Publishing. 2009, p. 012034.

[16] Gisela Schütz, Eberhard Goering, and Hermann Stoll. "Synchrotron Radiation Techniques Based on X-ray Magnetic Circular Dichroism". In: *Handbook of Magnetism and Advanced Magnetic Materials*. American Cancer Society, 2007. ISBN: 9780470022184. DOI: `10.1002/9780470022184.hmm304`. eprint: `https://onlinelibrary.wiley.com/doi/pdf/10.1002/9780470022184.hmm304`. URL: `https://onlinelibrary.wiley.com/doi/abs/10.1002/9780470022184.hmm304`.

[17] F. de Groot, A. Kotani. *Core Level Spectroscopy of Solids*. CRC Press, 2008.

[18] C. J. Ballhausen. *Introduction to Ligand Field Theory*. McGraw-Hill Book Company, 1962.

[19] J. M. D. Coey. "Magnetism of localized electrons on the atom". In: *Magnetism and Magnetic Materials*. Cambridge University Press, 2010, pp. 97–127. DOI: `10.1017/CBO9780511845000.005`.

[20] J. M. D. Coey. "Intermetallic Compounds and Crystal Field Interactions". In: *Science and Technology of Nanostructured Magnetic Materials*. Springer US, 1991, pp. 439–458. DOI: `10.1007/978-1-4899-2590-9`.

[21] CT Chen et al. "Experimental confirmation of the X-ray magnetic circular dichroism sum rules for iron and cobalt". In: *Physical review letters* 75.1 (1995), p. 152.

[22] Luuk J. P. Ament et al. "Resonant inelastic x-ray scattering studies of elementary excitations". In: *Rev. Mod. Phys.* 83 (2 June 2011), pp. 705–767. DOI: 10.1103/RevModPhys.83.705. URL: https://link.aps.org/doi/10.1103/RevModPhys.83.705.

[23] Marco Moretti Sala. "Magnetic and orbital resonant inelastic soft x-ray scattering". PhD thesis. Politecnico di Milano, 2011.

[24] Simo Huotari et al. "Crystal-field excitations in NiO under high pressure studied by resonant inelastic x-ray scattering". In: *Journal of Physics: Condensed Matter* 26.13 (Mar. 2014), p. 135501. DOI: 10.1088/0953-8984/26/13/135501. URL: https://doi.org/10.1088%2F0953-8984%2F26%2F13%2F135501.

[25] P Thakur et al. "Electronic structure of Cu-doped ZnO thin films by x-ray absorption, magnetic circular dichroism, and resonant inelastic x-ray scattering". In: *Journal of Applied Physics* 107.10 (2010), p. 103915.

[26] M. Guarise et al. "Measurement of Magnetic Excitations in the Two-Dimensional Antiferromagnetic $Sr_2CuO_2Cl_2$ Insulator Using Resonant X-Ray Scattering: Evidence for Extended Interactions". In: *Phys. Rev. Lett.* 105 (15 Oct. 2010), p. 157006. DOI: 10.1103/PhysRevLett.105.157006. URL: https://link.aps.org/doi/10.1103/PhysRevLett.105.157006.

[27] Andrea Amorese et al. "A RIXS investigation of the crystal-field splitting of Sm^{3+} in SmB_6". In: *arXiv e-prints*, arXiv:1901.10808 (Jan. 2019), arXiv:1901.10808. arXiv: 1901.10808 [cond-mat.str-el].

[28] URL: http://henke.lbl.gov/optical_constants/.

[29] L. Braicovich et al. "Spectroscopy of strongly correlated systems: Resonant x-ray scattering without energy resolution in the scattered beam". In: *Phys. Rev. B* 75 (7 Feb. 2007), p. 073104. DOI: 10.1103/PhysRevB.75.073104. URL: https://link.aps.org/doi/10.1103/PhysRevB.75.073104.

[30] L. Braicovich et al. "Resonant inelastic x-ray scattering from magnetic systems with angular resolution and polarization analysis of the scattered beam: Results on metallic Co, Fe, and Co ferrite at the $L_{3,2}$ edges". In: *Phys. Rev. B* 75 (18 May 2007), p. 184408. DOI: 10.1103/PhysRevB.75.184408. URL: https://link.aps.org/doi/10.1103/PhysRevB.75.184408.

[31] K Ishii et al. "Polarization-analyzed resonant inelastic x-ray scattering of the orbital excitations in KCuF 3". In: *Physical Review B* 83.24 (2011), p. 241101.

[32] H. A. Kramers and W. Heisenberg. "Über die Streuung von Strahlung durch Atome". In: *Zeitschrift für Physik* 31.1 (Feb. 1925), pp. 681–708. ISSN: 0044-3328. DOI: 10.1007/BF02980624. URL: https://doi.org/10.1007/BF02980624.

[33] K Kummer et al. "The high-field magnet endstation for X-ray magnetic dichroism experiments at ESRF soft X-ray beamline ID32". In: *Journal of synchrotron radiation* 23.2 (2016), pp. 464–473.

[34] URL: https://esrf.eu/about/synchrotron-science/synchrotron.

[35] URL: https://www.esrf.eu/about/upgrade.

[36] Shigemi Sasaki et al. "Design of a new type of planar undulator for generating variably polarized radiation". In: *Nuclear Instruments and Methods in Physics Research Section A: Accelerators, Spectrometers, Detectors and Associated Equipment* 331.1 (1993), pp. 763–767. ISSN: 0168-9002. DOI: https://doi.org/10.1016/0168-9002(93)90153-9. URL: http://www.sciencedirect.com/science/article/pii/0168900293901539.

[37] K Kummer et al. "Thin conductive diamond films as beam intensity monitors for soft x-ray beamlines". In: *Review of Scientific Instruments* 84.3 (2013), p. 035105.

[38] G. Haxel, J. Hedrick, J. Orris. "Rare Earth Elements-Critical Resources for High Technology". In: *United States Geological Survey* (2002).

[39] R. E. Watson A. J. Freeman. "Theoretical Investigation of Some Magnetic and Spectroscopic Properties of Rare-Earth Ions". In: *Phys. Rev.* 127 (6 Sept. 1962), pp. 2058–2075. DOI: 10.1103/PhysRev.127.2058. URL: https://link.aps.org/doi/10.1103/PhysRev.127.2058.

[40] J. C. Slater. "The Theory of Complex Spectra". In: *Phys. Rev.* 34 (10 Nov. 1929), pp. 1293–1322. DOI: 10.1103/PhysRev.34.1293. URL: https://link.aps.org/doi/10.1103/PhysRev.34.1293.

[41] R.D. Cowan. *The Theory of Atomic Structure and Spectra*. Los Alamos Series in Basic and Applied Sciences. University of California Press, 1981. ISBN: 9780520906150. URL: https://books.google.fr/books?id=tHOXLrXkJRgC.

[42] M. W. Haverkort. *Quanty - a quantum many body script language*. 2016. URL: http://quanty.org/.

[43] M. Rotter. *Crystal Field and Parameter Conventions*. URL: http://cpfs.mpg.de/~rotter/homepage_mcphase/manual/node130.html.

[44] URL: http://quanty.org/documentation/standard_operators/crystal_field.

[45] K. Kliemt et al. "$GdRh_2Si_2$: An exemplary tetragonal system for antiferromagnetic order with weak in-plane anisotropy". In: *Phys. Rev. B* 95 (13 Apr. 2017), p. 134403. DOI: 10.1103/PhysRevB.95.134403. URL: https://link.aps.org/doi/10.1103/PhysRevB.95.134403.

[46] T. Willers et al. "Crystal-field and Kondo-scale investigations of CeMIn$_5$ (M = Co, Ir, and Rh): A combined x-ray absorption and inelastic neutron scattering study". In: *Phys. Rev. B* 81 (19 May 2010), p. 195114. DOI: 10.1103/PhysRevB.81.195114. URL: https://link.aps.org/doi/10.1103/PhysRevB.81.195114.

[47] Z.-S. Liu. "The susceptibilities and molecular-field constants of rare-earth compounds from mean-field theory". In: *Materials Letters* 58.25 (2004), pp. 3111–3114. ISSN: 0167-577X. DOI: https://doi.org/10.1016/j.matlet.2004.05.051. URL: http://www.sciencedirect.com/science/article/pii/S0167577X04003726.

[48] Rikio Settai et al. "Single Crystal Growth and Magnetic Properties of CeRh 2Si 2". In: *Journal of the Physical Society of Japan* 66.8 (1997), pp. 2260–2263. DOI: `10.1143/JPSJ.66.2260`. eprint: `https://doi.org/10.1143/JPSJ.66.2260`. URL: `https://doi.org/10.1143/JPSJ.66.2260`.

[49] A. Amorese et al. "Crystal electric field in $CeRh_2Si_2$ studied with high-resolution resonant inelastic soft x-ray scattering". In: *Phys. Rev. B* 97 (24 June 2018), p. 245130. DOI: `10.1103/PhysRevB.97.245130`. URL: `https://link.aps.org/doi/10.1103/PhysRevB.97.245130`.

[50] A. Amorese et al. "4f excitations in Ce Kondo lattices studied by resonant inelastic x-ray scattering". In: *Phys. Rev. B* 93 (16 Apr. 2016), p. 165134. DOI: `10.1103/PhysRevB.93.165134`. URL: `https://link.aps.org/doi/10.1103/PhysRevB.93.165134`.

[51] Andrea Amorese et al. "Determining the local low-energy excitations in the Kondo semimetal $CeRu_4Sn_6$ using resonant inelastic x-ray scattering". In: *Phys. Rev. B* 98 (8 Aug. 2018), p. 081116. DOI: `10.1103/PhysRevB.98.081116`. URL: `https://link.aps.org/doi/10.1103/PhysRevB.98.081116`.

[52] M. W. Haverkort. "Quantyfor core level spectroscopy - excitons, resonances and band excitations in time and frequency domain". In: *Journal of Physics: Conference Series* 712 (May 2016), p. 012001. DOI: `10.1088/1742-6596/712/1/012001`. URL: `https://doi.org/10.1088%5C%2F1742-6596%5C%2F712%5C%2F1%5C%2F012001`.

[53] M. Retegan. *Crispy: v0.7.2*. 2019. DOI: `10.5281/zenodo.1451209`. URL: `https://zenodo.org/badge/latestdoi/53660512`.

[54] P. W. Anderson. "Localized Magnetic States in Metals". In: *Phys. Rev.* 124 (1 Oct. 1961), pp. 41–53. DOI: `10.1103/PhysRev.124.41`. URL: `https://link.aps.org/doi/10.1103/PhysRev.124.41`.

[55] P. Coleman. *Heavy Fermions and the Kondo Lattice: a 21st Century Perspective*. print arXiv:1509.05769. Sept. 2015.

[56] J. M. D. Coey. "Ferromagnetism and exchange". In: *Magnetism and Magnetic Materials*. Cambridge University Press, 2010, pp. 128–194. DOI: `10.1017/CBO9780511845000.006`.

[57] S. Blundell. *Magnetism in Condensed Matter*. Oxford Master Series in Condensed Matter Physics. OUP Oxford, 2001. ISBN: 9780198505914. URL: `https://books.google.it/books?id=OGhGmgEACAAJ`.

[58] Jun Kondo. "Resistance Minimum in Dilute Magnetic Alloys". In: *Progress of Theoretical Physics* 32.1 (July 1964), pp. 37–49. ISSN: 0033-068X. DOI: `10.1143/PTP.32.37`. eprint: `http://oup.prod.sis.lan/ptp/article-pdf/32/1/37/5193092/32-1-37.pdf`. URL: `https://doi.org/10.1143/PTP.32.37`.

[59] K. Andres, J. E. Graebner, and H. R. Ott. "4f-Virtual-Bound-State Formation in $CeAl_3$ at Low Temperatures". In: *Phys. Rev. Lett.* 35 (26 Dec. 1975), pp. 1779–1782. DOI: `10.1103/PhysRevLett.35.1779`. URL: `https://link.aps.org/doi/10.1103/PhysRevLett.35.1779`.

[60] C. M. Varma. “Mixed-valence compounds”. In: *Rev. Mod. Phys.* 48 (2 Apr. 1976), pp. 219–238. DOI: 10.1103/RevModPhys.48.219. URL: https://link.aps.org/doi/10.1103/RevModPhys.48.219.

[61] S. Doniach. “The Kondo lattice and weak antiferromagnetism”. In: *Physica B+C* 91 (1977), pp. 231–234. ISSN: 0378-4363. DOI: https://doi.org/10.1016/0378-4363(77)90190-5. URL: http://www.sciencedirect.com/science/article/pii/0378436377901905.

[62] Dai Aoki, William Knafo, and Ilya Sheikin. “Heavy fermions in a high magnetic field”. In: *Comptes Rendus Physique* 14 (Jan. 2013), pp. 53–77. DOI: 10.1016/j.crhy.2012.11.004. arXiv: 1204.5128 [cond-mat.str-el].

[63] L. D. Landau. “The theory of a Fermi liquid”. In: *Soviet Physics Jetp-USSR* 3.6 (1957), pp. 920–925. URL: http://jetp.ac.ru/files/Landau1en.pdf.

[64] Christian Pfleiderer. “Superconducting phases of f-electron compounds”. In: *Rev. Mod. Phys.* 81 (4 Nov. 2009), pp. 1551–1624. DOI: 10.1103/RevModPhys.81.1551. URL: https://link.aps.org/doi/10.1103/RevModPhys.81.1551.

[65] G. R. Stewart. “Non-Fermi-liquid behavior in d- and f-electron metals”. In: *Rev. Mod. Phys.* 73 (4 Oct. 2001), pp. 797–855. DOI: 10.1103/RevModPhys.73.797. URL: https://link.aps.org/doi/10.1103/RevModPhys.73.797.

[66] Qimiao Si et al. “Locally critical quantum phase transitions in strongly correlated metals”. In: 413 (Oct. 2001), pp. 804–808. DOI: 10.1038/35101507. arXiv: cond-mat/0011477 [cond-mat.str-el].

[67] URL: https://icsd.fiz-karlsruhe.de/search/basic.xhtml;jsessionid=339C3D158E35A9C1937BAFA6AD9E4636.

[68] Christoph Geibel. “A new Ce-based heavy fermion system close to a possibly multipolar Quantum Critical Point: CeRh2As2”. In: *Emergent phenomena in strongly correlated quantum matter.* 2018. URL: https://youtu.be/ZgMlDuoWfFo.

[69] R. Madar et al. “New ternary pnictides with the CaBe2Ge2-type structure in the systems, rare-earth-Rh-P and rare-earth-Rh-As”. In: *Journal of the Less Common Metals* 133.2 (1987), pp. 303–311. ISSN: 0022-5088. DOI: https://doi.org/10.1016/0022-5088(87)90241-4. URL: http://www.sciencedirect.com/science/article/pii/0022508887902414.

[70] A. Szytua et al. “Magnetic ordering in NdRh2Si2 and ErRH2Si2”. In: *Solid State Communications* 52.4 (1984), pp. 395–398. ISSN: 0038-1098. DOI: https://doi.org/10.1016/0038-1098(84)90021-8. URL: http://www.sciencedirect.com/science/article/pii/0038109884900218.

[71] Kristin Kliemt. “Crystal growth and characterization of cerium- and ytterbium-based quantum critical materials”. PhD thesis. 2018. URL: http://publikationen.ub.uni-frankfurt.de/frontdoor/index/index/year/2018/docId/46923.

[72] K Kliemt, M Bolte, and C Krellner. "Crystal growth and magnetic characterization of HoIr2Si2 (I4/mmm)". In: *Journal of Physics: Condensed Matter* 30.38 (Aug. 2018), p. 385801. DOI: `10.1088/1361-648x/aada97`. URL: `https://doi.org/10.1088%5C%2F1361-648x%5C%2Faada97`.

[73] Alexander Generalov et al. "Spin Orientation of Two-Dimensional Electrons Driven by Temperature-Tunable Competition of Spin–Orbit and Exchange–Magnetic Interactions". In: *Nano Letters* 17.2 (2017). PMID: 28032768, pp. 811–820. DOI: `10.1021/acs.nanolett.6b04036`. eprint: `https://doi.org/10.1021/acs.nanolett.6b04036`. URL: `https://doi.org/10.1021/acs.nanolett.6b04036`.

[74] R Welter, K Halich, and B Malaman. "Magnetic study of the ThCr2Si2-type RIr2Si2 (R=Pr,Nd) compounds: Magnetic structure of NdIr2Si2 from powder neutron diffraction". In: *Journal of Alloys and Compounds* 353.1 (2003), pp. 48–52. ISSN: 0925-8388. DOI: `https://doi.org/10.1016/S0925-8388(02)01298-7`. URL: `http://www.sciencedirect.com/science/article/pii/S0925838802012987`.

[75] M. Ślaski, J. Leciejewicz, and A. SzytuŁa. "Magnetic ordering in HoRu2Si2, HoRh2Si2, TbRh2Si2 and TbIr2Si2 by neutron diffraction". In: *Journal of Magnetism and Magnetic Materials* 39.3 (1983), pp. 268–274. ISSN: 0304-8853. DOI: `https://doi.org/10.1016/0304-8853(83)90085-9`. URL: `http://www.sciencedirect.com/science/article/pii/0304885383900859`.

[76] M. Melamud et al. "Neutron diffraction study of the magnetic structure of the intermetallic compound DyRh2Si2". In: *Journal of Applied Physics* 55.6 (1984), pp. 2034–2035. DOI: `10.1063/1.333556`. eprint: `https://doi.org/10.1063/1.333556`. URL: `https://doi.org/10.1063/1.333556`.

[77] J.P. Sanchez et al. "Magnetic properties of DyIr2Si2 and ErIr2Si2". In: *Journal of Magnetism and Magnetic Materials* 128.3 (1993), pp. 295–301. ISSN: 0304-8853. DOI: `https://doi.org/10.1016/0304-8853(93)90474-G`. URL: `http://www.sciencedirect.com/science/article/pii/030488539390474G`.

[78] Michal Vališka et al. "Influence of symmetry on Sm magnetism studied on SmIr2Si2 polymorphs". In: *Journal of Alloys and Compounds* 574 (2013), pp. 459–466. ISSN: 0925-8388. DOI: `https://doi.org/10.1016/j.jallcom.2013.05.047`. URL: `http://www.sciencedirect.com/science/article/pii/S0925838813012073`.

[79] K. Kliemt and C. Krellner. "Single crystal growth and characterization of GdRh2Si2". In: *Journal of Crystal Growth* 419 (2015), pp. 37–41. ISSN: 0022-0248. DOI: `https://doi.org/10.1016/j.jcrysgro.2015.02.079`. URL: `http://www.sciencedirect.com/science/article/pii/S0022024815001700`.

[80] Monika Güttler et al. "Robust and tunable itinerant ferromagnetism at the silicon surface of the antiferromagnet GdRh 2 Si 2". In: *Scientific reports* 6 (2016), p. 24254.

[81] M. Mihalik et al. “Magnetism in polymorphic phases: Case of $PrIr_2Si_2$”. In: *Phys. Rev. B* 81 (17 May 2010), p. 174431. DOI: `10.1103/PhysRevB.81.174431`. URL: `https://link.aps.org/doi/10.1103/PhysRevB.81.174431`.

[82] K. Kliemt et al. “$GdRh_2Si_2$: An exemplary tetragonal system for antiferromagnetic order with weak in-plane anisotropy”. In: *Phys. Rev. B* 95 (13 Apr. 2017), p. 134403. DOI: `10.1103/PhysRevB.95.134403`. URL: `https://link.aps.org/doi/10.1103/PhysRevB.95.134403`.

[83] E. Stryjewski and N. Giordano. “Metamagnetism”. In: *Advances in Physics* 26.5 (1977), pp. 487–650. DOI: `10.1080/00018737700101433`. eprint: `https://doi.org/10.1080/00018737700101433`. URL: `https://doi.org/10.1080/00018737700101433`.

[84] J. C. Parlebas et al. “X-ray magnetic circular dichroism at rare-earth L23 absorption edges in various compounds and alloys”. English. In: *Physics Reports* 431.1 (Aug. 2006), pp. 1–38. ISSN: 0370-1573. DOI: `10.1016/j.physrep.2006.05.002`.

[85] V.A. Solé et al. “A multiplatform code for the analysis of energy-dispersive X-ray fluorescence spectra”. In: *Spectrochimica Acta Part B: Atomic Spectroscopy* 62.1 (2007), pp. 63–68. ISSN: 0584-8547. DOI: `https://doi.org/10.1016/j.sab.2006.12.002`. URL: `http://www.sciencedirect.com/science/article/pii/S0584854706003764`.

[86] T. Willers et al. “Spectroscopic determination of crystal-field levels in $CeRh_2Si_2$ and $CeRu_2Si_2$ and of the $4f^0$ contributions in CeM_2Si_2 (M=Cu, Ru, Rh, Pd, and Au)”. In: *Phys. Rev. B* 85 (3 Jan. 2012), p. 035117. DOI: `10.1103/PhysRevB.85.035117`. URL: `https://link.aps.org/doi/10.1103/PhysRevB.85.035117`.

[87] HA Kramers. “HA Kramers, Proc. Acad. Sci. Amsterdam 33, 959 (1930).” In: *Proc. Acad. Sci. Amsterdam*. Vol. 33. 1930, p. 959.

[88] Andrew Steele. “Quantum magnetism probed with muon-spin relaxation”. PhD thesis. University of Oxford, 2011. URL: `https://andrewsteele.co.uk/physics/thesis/andrew-steele-dphil-thesis.pdf`.

[89] Ernst Ising. “Beitrag zur Theorie des Ferromagnetismus”. In: *Zeitschrift für Physik* 31.1 (Feb. 1925), pp. 253–258. ISSN: 0044-3328. DOI: `10.1007/BF02980577`. URL: `https://doi.org/10.1007/BF02980577`.